UNIVERSITY OF CALIFORNIA
RIVERSIDE

Combined Theory and Experiment Toward Designing and Preparing Itinerant Magnetic Transition Metal-rich Borides of $Ti_3Co_5B_2$-type

A Dissertation submitted in partial satisfaction
of the requirements for the degree of

Doctor of Philosophy

in

Chemistry

by

Pritam Shankhari

September 2019

Dissertation Committee:
Dr. Boniface P. T. Fokwa, Chairperson
Dr. Pingyun Feng
Dr. Kevin Kou

The Dissertation of Pritam Shankhari is approved:

Committee Chairperson

University of California, Riverside

Acknowledgment

I would like to express my deepest gratitude to my advisor Dr. Bonface P. T. Fokwa for all the guidance, support, and compassion that he has bestowed upon me during my PhD. I consider myself truly lucky to have an advisor like him who has always believed in me, encouraged me to do my best, and stood by me at my worst.

I would like to thank rest of my dissertation committee members: Dr. Pingyun Feng, Dr. Kevin Kou and the late Dr. Robert C. Haddon for their insightful comments and suggestions at various stages during my PhD.

I would like to thank my Masters advisor Prof. Sundargopal Ghosh at IIT Madras. His advice and guidance at many crucial moments of my life have shaped me as a person and as a researcher.

I would also like to thank all our collaborators, especially the Haddon Group from UC Riverside and Dr. Craig Brown, NIST, Gaithersburg, MD who have generously helped me with their instrument facilities in my research and provided scientific feedbacks.

I was fortunate enough to come across many wonderful friends and colleagues in Riverside who has made this journey easier for me. The list is huge, and I thank all of them from the bottom of my heart, especially all my labmates.

Few friends who have always believed in me and encouraged to do the unthinkable, I thank them all for reaching me to this stage of life. And finally, I would like to thank god for giving me a wonderful family whose love, support and continuous believe in me has powered me to complete this long journey successfully.

This dissertation is dedicated to my mother, Smt Manisha Shankhari, and my father, late Shri Prannath Shankhari

ABSTRACT OF THE DISSERTATION

Combined Theory and Experiment Toward Designing and Preparing Itinerant Magnetic Transition Metal-rich Borides of $Ti_3Co_5B_2$-type

by

Pritam Shankhari

Doctor of Philosophy, Graduate Program in Chemistry
University of California, Riverside, September 2019
Dr. Boniface P. T. Fokwa, Chairperson

Theoretical screening of hypothetical compounds based on a known structure type is a promising approach to facilitate the design of new materials in solid-state chemistry. Electronic structure calculation on $Ti_3Co_5B_2$ structure type ternaries yields a large pseudo-gap at the Fermi level in the density of states (DOS) plot, indicating electronic stability and offers the possibility of tuning the Fermi level via chemical substitutions to derive new isostructural phases. Following this pathway, new promising magnetic materials in this structure type were first predicted by DFT, then prepared by high-temperature synthetic techniques, and finally characterized by X-ray diffraction, EDX analysis, and magnetic measurements.

Total energy calculations by Vienna Ab initio simulation package (VASP) for the quaternary $Hf_2MnRu_5B_2$ predicted a competition for antiferro- and ferromagnetic states in a ruthenium-rich compound of this structure type for the first time. Temperature-dependent magnetization measurements of this compound showed an antiferromagnetic transition at

a low magnetic field (0.005 T), whereas dominating ferromagnetic interactions observed at higher fields confirmed the competition between antiferro- and ferromagnetic states predicted by VASP.

Next, a complete theoretical and experimental study of the ruthenium-rich quaternary series of borides $A_2MRu_5B_2$ (A = Hf, Zr; M = Fe, Mn) established the fundamental difference between the Mn and Fe-based Ru-rich compounds in this structure type: Mn enhances ferromagnetic interactions whereas Fe-based compounds clearly prefer antiferromagnetic ground states. Additionally, it was understood that the 5d element Hf was assisting Mn to further enhance the ferromagnetic interactions, making 5d-rich compounds promising targets.

Lastly, 5d-rich $Hf_2FeIr_5B_2$ and $Hf_2MnIr_5B_2$ were predicted to have strong magnetic anisotropy (i.e. permanent magnet candidates). Experiments confirmed and extended these predictions: $Hf_2FeIr_5B_2$ orders at T_C ~ 901 K and has a coercivity value of 12 kA/m whereas $Hf_2MnIr_5B_2$ orders at about 590 K and has a coercivity of 62 kA/m (the highest value reported for this structure type). $Hf_2MnIr_5B_2$ is the first hard magnetic material in this structure type showing ordering temperature far above room temperature. The good coercivity values of both compounds coupled with their high ordering temperatures make them viable candidates for achieving competitive room temperature permanent magnetic properties in the future.

Table of Contents

Chapter 1:

Introduction, Computational Methods, and Experimental Techniques

1.1. Introduction

Recent bloom in clean and environment-friendly technologies such as electric vehicles, magnetic refrigeration, and wind turbines has increased the demand for high-performing permanent magnetic materials.[1, 2] Thus, a large share of research efforts in solid-state and materials community is concerned with the design and preparation of new permanent magnetic materials. However, as DiSalvo mentioned, "We usually discover materials with enhanced and especially with novel properties by chance rather than design", it is nearly impossible to safely design predict new compounds with novel properties.[3] When it comes to designing new magnetic materials, the scenario is even more challenging, mostly because magnetism itself is a very complex phenomenon. Even today, it is not fully understood why some materials order magnetically whereas the clear majority don't. It's been almost 30 years since the strongest permanent magnet $Nd_2Fe_{14}B$ [4] was discovered and until today we are solely dependent on the supply of rare-earth elements, such as Nd and Dy for the best-performing permanent magnets, both of which have been classified as critical by the U.S. Department of Energy. [5]

On the brighter side, preparing new materials based on a known structure type is much promising—by elemental substitutions or intercalation of species into an existing structure. Furthermore, due to the advancements in computational methods, especially density functional theory (DFT), it is possible to calculate thermodynamic stability and atomic interactions of complex solids by good precision. [6] Thus, screening of hypothetical

phases derived from a known structure type can largely facilitate the synthesis of new stable compounds with target properties by calculating their stabilities and interpreting their atomic interactions by DFT. For this purpose, materials with large structural and compositional diversity, such as metal borides make excellent candidates.

Metal borides (M_xB_y) can largely be classified into two groups as boron-rich (B:M ≥ 4:1) and metal-rich (B:M < 4:1) which crystallize in more than 150 structure types comprising thousands of compounds.[7] Owing to boron's atomic size, electron deficiency, and position in the periodic table, metal borides exhibit bonding motifs that contain extended covalent networks. Some characteristic properties of borides include high melting point, extreme hardness, chemical inertness, and excellent wear resistance which stem from the strong covalent metal-boron and boron-boron bonds present in them.[8] With such wide ranges of compositions and structures, metal borides often show extraordinary novel physical properties. For example, some metal borides show superconductivity, such as MgB_2, [9] which was the first high-temperature metallic superconductor and the recently discovered low-temperature superconductors TaRuB and NbOsB [10]. The boron-rich YB_{66} show superior stability against neutron and other radiations and is used as the monochromator for soft synchrotron radiation [11], while LaB_6 is a good thermionic emitter and is used in electron guns for electron microscopes.[12] Moreover, when containing magnetically active elements in their composition, some rare-earth (RE) based borides are known to show strong permanent magnetic properties.[4, 13] The previously mentioned $Nd_2Fe_{14}B$, widely recognized as "neodymium magnet" is probably the most popular of them as it plays a crucial role in our daily-used electronic devices. Rare-earth-

free (REF) borides containing magnetically active elements, on the other hand, are known to exhibit comparatively “soft” itinerant magnetic properties. Such itinerant magnetism, which stems from the synergy between magnetically active elements and conduction electrons offers potential applications in magnetic refrigeration and spintronics.[14-18].

Very interestingly, the extraordinary properties of some borides can be directly related to their crystal structure and arrangement of boron atoms in them. For example, the planar structure built by hexagonally ordered boron atoms is believed to have an influence on the superconductivity of MgB_2. This discovery attracted the scientific community to investigate certain types of borides having planar boron layers in the past decade and many theoretical and experimental works have been done to develop new 2D-like materials.[10, 19]

In this dissertation, designing and developing new rare-earth free magnetic materials based on the prolific $Ti_3Co_5B_2$-type [20] borides will be elaborated. The quaternary and quinary variants of the $Ti_3Co_5B_2$ structure type contain one-dimensional chains of magnetically active elements built by strategically placing them at one suitable crystallographic site (2*a*). Such quaternaries and quinaries are known to show interesting itinerant magnetic properties.[21, 22] The motivation of the works presented in this dissertation stems from preliminary theoretical investigations showing interesting magnetic properties in some manganese-based compounds [23], especially their semi-hard to hard magnetic properties.

1.2 Computational methods

At first, DFT was applied to screen stability and magnetic interactions of different hypothetical ternary and quaternary compounds. This was done by calculating the total energy and electronic structures using VASP. [24] Relative energies of different magnetic models were then analyzed. Furthermore, bonding and magnetic interactions between different atoms were understood through crystal orbital Hamilton population (COHP) analysis as implemented in the Linear Muffin-Tin Orbital Projection (LMTO) code.[25] The different quantum chemical methods that were used to screen and predict the new compounds are briefly introduced below.

1.2.1 Quantum chemical treatment of chemical bonding

Figure 1.1 represents electronic band structure, the density of states (DOS) and crystal orbital Hamilton population (COHP) plots of a hypothetical one-dimensional crystal of hydrogen atoms adapted from the works by Dronskowski et al.[26, 27] Figure 1.1a shows the k-dependent wave function of a linear chain of H atoms with one H per unit cell. At the lowest energy (zone center) all the 1s orbitals have the same sign (shown in grey) and are in-phase. They have the highest H-H bonding combination and thus, are the most stabilized (lowest in energy). At the highest energy, maximum H-H antibonding interactions between nearest atomic orbitals are present and we see maximum out-of-phase combinations (white and grey shades represent opposite signs of the orbitals). In between, there are extremely large numbers (as many as unit cells present) of closely-spaced energy levels that appear as a "band". Figure 1.1b represents the DOS which results from the inverse slope of the band structure from Figure 1a. The "density of states" plot, as it sounds, represents the

density of energy levels (states) in an energy band at different energies. A quick look at Figure 1.1b tells us that the density of states is maximum at the bottom and top of the band meaning that the energy levels are closely spaced in these two regions, whereas it is the minimum in the center where the energy levels are widespread. Thus, a flat energy band will result in a sharp peak in the DOS and a wide energy band will result in a flat and spread DOS. Figure 1.1c in the right presents the Hamilton population-weighted density of states or the COHP. The COHP is a bond indicator for solids and is derived by multiplying the DOS by the corresponding Hamilton element and it adopts a negative value for bonding and positive value for antibonding. Figure 1.1c shows two such COHP plots: for interactions between 1-2 and 1-3 hydrogens in an H-chain. Comparison between Figure 1.1a and 1.1c shows that for the 1-2 H-H interaction, -COHP (negative COHP) value is bonding in low energies and antibonding in higher energies, which is evident from the orbital interaction pictures in Figure 1.1a. For the 1-3 H-H interaction, however, we see a quite different plot. Firstly, the interaction distance is larger, so we have a smaller value of COHP. Both the lower and high energy orbital interactions are in phase, and hence, we get boding interactions in both these regions. In between, we have the non-bonding regions. Thus, the band structure can be partitioned into bonding, non-bonding and antibonding contribution of orbital pairs through COHP.

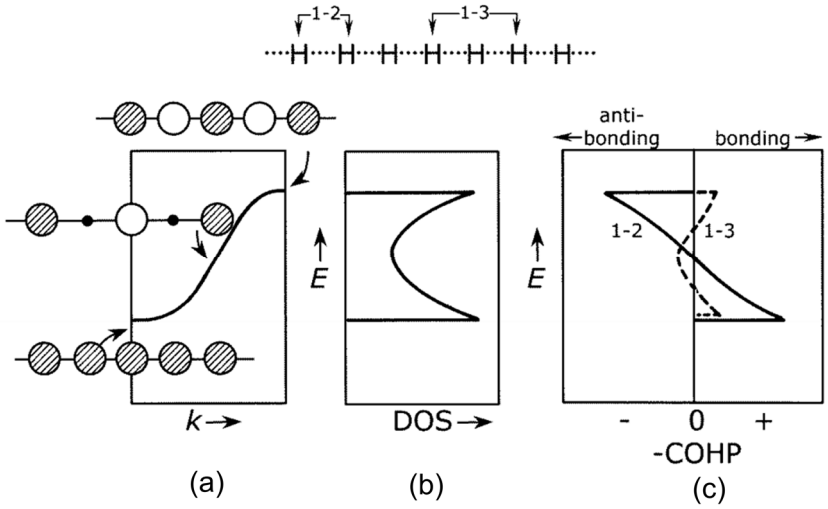

Figure 1.1. (a) Electronic band structure, (b) density of states (DOS), and (c) crystal Orbital Hamilton Population (COHP) (right) of a one-dimensional crystal of hydrogen atoms (Reproduced from [26]).

1.2.2 Electronic theory of itinerant magnetism: A chemical bonding perspective

The presence of a pseudogap at the Fermi level (E_F) is a widely recognized feature of electronic stability in intermetallic compounds.[27] Compounds that have a pseudogap around E_F in the DOS plot are known to be electronically stable. Compounds that have a high density of states at E_F are electronically less stable and susceptible to structural or electronic distortion to gain stability. For example, TiH_2 [28] undergoes Jahn-Teller type distortion to lower DOS at E_F. In other cases, especially when magnetically active elements are involved in the bonding, rearrangement of the electronic structure may occur which can result in the development of long-range magnetic ordering. The whole process is elaborated with the excellent work by Dronskowski et al shown below.

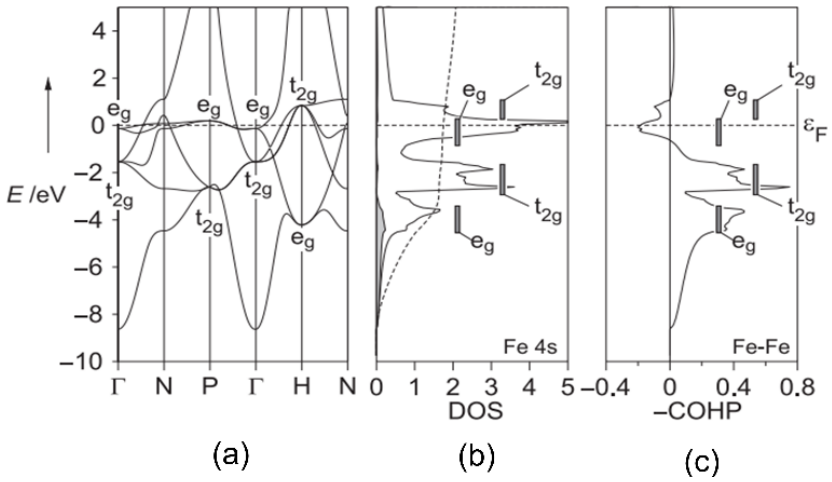

Figure 1.2. Non-spin-polarized (a) Band structure, (b) DOS, and (c) Fe-Fe COHP curves of α-Fe (Reproduced from [26]).

Figure 1.2 shows non-spin-polarized (local spin density approximation or LSDA) electronic structures of α-Fe (body-centered cubic, *bcc*). The calculated DOS plot contains a large peak at E_F (Figure 1.2b). As evident from the COHP plot (Figure 1.2c), this E_F falls in a Fe-Fe antibonding region. However, in spite of having a large DOS at the $E_{F,}$ no structural change is observed in *bcc* Fe, rather an electronic distortion occurs, which reduces the electronic symmetry, lowers the energy and gives rise to magnetism.[27]

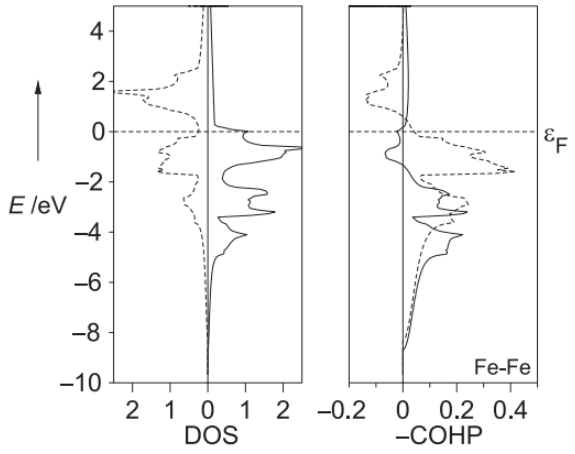

Figure 1.3. Spin-polarized (a) DOS, and (c) Fe-Fe COHP curves of α-Fe (Reproduced from [26]).

The spin-polarized (LSDA) electronic structures are shown in Figure 1.3. In the LSDA DOS calculation, the two spin sublattices shift in energy, the majority spins are lower in energy and the minority spins are higher in energy, resulting in a net magnetic moment. The LSDA Fe-Fe -COHP curve shows that spin polarization removes antibonding states at E_F by shifting the majority and minority spins, thus, lowering the total energy of the system (stabilization). Spin polarization further strengthens the Fe-Fe bond by 5%. Extending this theory to the entire 3d series (Figure 1.4) Dronskowski et al shows that for early transition metals E_F falls in the metal-metal bonding region and thereby no drive towards ferromagnetism is present. For a typical antiferromagnet Cr, E_F falls in the non-bonding region, whereas from "Mn" (hypothetical *bcc* Mn) to Ni E_F falls in the antibonding region, in accordance with the known ferromagnetic ordering found for *bcc* Ni, Co, and Fe.

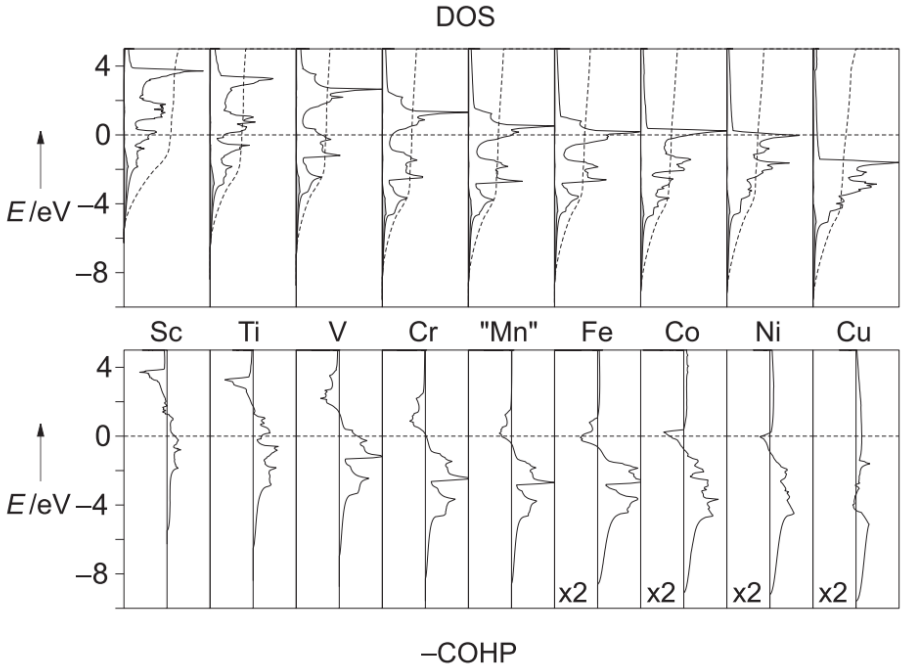

Figure 1.4. Non-spin-polarized DOS and M-M COHP curves for the 3d transition metals (Reproduced from [26]).

The theoretical background discussed so far provided us the key ingredients to screen and predict new magnetic materials, which will be presented in chapter 2, 3, and 4.

1.2.3 Magnetocrystalline anisotropy: A tool for predicting permanent magnets

Magnetocrystalline anisotropy refers to the dependence of magnetic energy on the magnetization axis compared to the crystallographic axes. Such preferred orientation of spins is responsible for maintaining the metastable domain configuration of a permanent magnet and affects the coercivity (H_C) and remanence—thus, the shape of the hysteresis loop. d-block elements possess smaller magnetocrystalline anisotropy by virtue of their electronic properties. On the other hand, rare-earth-based permanent magnets possess large magnetocrystalline anisotropy energy (MAE) which mainly stems from the large spin-orbit coupling (SOC) of rare-earth (f-electrons) elements. [1, 2] This large MAE results in very large H_C value that contributes to the high energy product (BH_{max}) of rare-earth magnets.

As far as designing a new permanent magnetic material is concerned, the desired properties are (i) a high ordering temperature (T_C), (ii) a large saturation magnetization and (iii) a strong magnetic anisotropy.[29] Since magnetism is highly sensitive to temperature, a high T_C and good thermal stability are desired for any practical application of a magnet without requiring additional cooling steps. Although the first two criteria mentioned above can be met with a rare-earth-free pure transition metal/intermetallic magnet without any f-electrons, it is the latter requirement that throws a real challenge.

There is no well-defined rule for anisotropy of d-elements. Single-ion magnetic anisotropy originates from spin-orbit coupling (SOC). Since, SOC is a relativistic mechanism (the single-electron SOC constant $\zeta \propto Z^2$), the anisotropy generally varies as a

function of the atomic number (Z). Hence, heavy elements, such as rare-earths have the highest anisotropies due to their large SOC.[29, 30] According to [29] anisotropy constant of an itinerant ferromagnet is given by:

$$K_1 \approx \pm\frac{1}{4}\zeta\,\Delta L$$

where ζ is the single-electron spin-orbit coupling and ΔL = anisotropy of the orbital moment, defined as:

$$\Delta L = < L > M||Z - < L > M\perp Z$$

However, the anisotropy constants of the 3d ferromagnets calculated using this equation are overestimated by at least 1.5 orders of magnitude. The reason is that the expected values of the orbital moment are much lower which makes ΔL very small. It is believed that the 3d orbital moment is quenched and one needs to overcome this quenching to make a hard-permanent magnet out of 3d elements. [29] Rare-earth moments, on the other hand, are unquenched and show a strong coupling between the 4f charge cloud and the spin. [30] Although calculating anisotropy constants of a specific compound is possible based on these calculations, they cannot provide a solid guideline for enhancing magnetic anisotropy. Yet, a few ideas can be deduced from the scientific background as suggested by Kuz'min et al.: avoidance of cubic structures (increasing structural anisotropy to assist increase magnetic anisotropy), volume expansion, and inclusion of heavier 5d elements. [29] These suggestions provided grounds for designing the large magnetic anisotropy materials that will be presented in Chapter 5 of this dissertation.

1.3 Experimental techniques

Following this theoretical assessment, the promising compounds were synthesized and characterized. Detail of general synthesis procedure, characterization and structure determination methods are given below.

1.3.1 Synthesis

To prepare the samples for synthesis, commercially available high-purity (99.95 % purity) elemental powders (200-325 mesh) were used. Few elements, such as Boron (97%) and Zr/Hf (Hf/Zr impurity 2-3%) are not commercially available highly-pure grade, and we used the best material available. The purity of the commercially purchased elemental powders was checked using powder X-ray diffraction before synthesis to ensure quality. The elements were weighed (totaling in 200 – 1000 mg) in desired atomic ratio and transferred into an agate mortar where they were pulverized vigorously until a homogeneous mixing was achieved. Following that, the finely mixed powders were pressed into a pellet using a die-set (5 – 10 mm diameter) and a hydraulic press (pressure ranging 2 – 5 ton). All of these were done inside a nitrogen glove box (below 2.0 ppm oxygen level). The syntheses were performed at high temperatures under argon atmosphere using either an arc-melting or a muffle furnace. For the arc-melting, the sample pellet was loaded into the water-cooled copper crucible (primary electrode) inside the arc-melting chamber connected to a *Schlenk* line. The sample pellet was kept under vacuum for 15 – 20 minutes and then purged with Argon. This whole procedure was repeated 3 times to ensure the absence of oxygen inside the chamber. The argon gas was purified prior to use over silica gel, molecular sieves and titanium sponge (at 900 K). The pellet was arc-melted

on the water-cooled copper crucible electrode using a tungsten tip as the second electrode. The melting was done using 20 – 40 Amps current depending on the sample and took a few seconds. Each sample was flipped and re-melted for 2 – 3 times to ensure a homogeneous melting. Extra caution was taken when using an element with a low boiling point. Prolonged melting might abruptly increase temperature and evaporate low-melting metals such as manganese.

For the synthesis or annealing using a muffle furnace, the pellet (for annealing the arc-melted ingot) was placed inside an alumina crucible (9 mm outer diameter) and put inside a close-end quartz tube (10 mm inner diameter). The other end of the quartz tube was vacuum-sealed. The sealed quartz-tube was then transferred inside a muffle furnace where the synthesis/annealing was done using the desired temperature profile.

1.3.2 Sample preparation for characterization

Following the synthesis, the cooled ingot was crushed using a custom-made tungsten carbide die-set with high-hardness. The ingots were placed in between the two dies and crushed using a hydraulic press. After crushing the samples were ground into powder using an agate mortar and pestle and thus was ready for powder XRD analysis. Whenever needed, the powder was washed with concentrated hydrochloric acid that dissolved unwanted metallic impurities such as unreacted metal and unwanted alloys. The synthesized metal borides were stable in HCl. The washing procedure was monitored by checking powder XRD and disappearance of effervescence (hydrogen gas produced by the reaction of unreacted metals with HCl). Following that, the acid-washed powder was further washed with deionized water and dried in an oven for further characterization.

1.3.3 Characterization by powder XRD

Powder X-ray data of the powdered samples were collected at room temperature, mostly using a Rigaku MiniFlex 600 diffractometer with Cu-$K_{\alpha 1}$ radiation (λ = 1.54059 Å), image plate detector, Ge monochromator using silicon as the standard. The phase analysis of the sample mixture was done by *Rietveld* refinement of the powder X-ray diffraction (XRD) data using the *FullProf.*[31, 32]

1.3.4 Characterization by single-crystal XRD

Suitable single crystals obtained from the crushed samples of arc-melted ingot and were measured in a Rigaku XtalLAB mini diffractometer with λ(Cu-$K_{\alpha 1}$) = 1.54059 Å for single-crystal structure analysis. The intensities were corrected with respect to the absorption using a numerical procedure based on gaussian integration over a multifaceted crystal model employed in CrysAlis Pro package.[33] The crystal structures were solved by the direct method and refined using SHELX employed in WinGX. [34, 35] The positions of the metals atoms were obtained by direct methods and the boron position was found in the electron density map after a few cycles of the full-matrix least-squares refinement (based on F^2).

1.4 Arrangement of the Dissertation:

This dissertation is organized as follows:

In chapter 1, a brief introduction on metal borides and their potential as host to new magnetic materials have been discussed. Different quantum chemicals methods that will be utilized to analyze electronic structures and screen magnetic interactions have been introduced. As well as different experimental and characterization techniques used have been discussed.

In chapter 2, the $Ti_3Co_5B_2$ structure type has been introduced and first-time bulk synthesis of the ternary $Ti_3Co_5B_2$ has been presented. In addition, its electronic structure has been calculated and its stability has been compared with other competing compounds.

In chapter 3, the prediction, synthesis, characterization and magnetic properties of new Ru-rich quaternary $Hf_2MnRu_5B_2$ are discussed. The unprecedented behavior of Mn in enhancing ferromagnetic interaction was revealed for the first time in this structure type.

In chapter 4, a series of quaternary compounds $A_2MRu_5B_2$ (A = Hf, Zr; M = Fe, Mn) are presented. Their synthesis, characterization, electronic structure calculation, and magnetic properties are presented. This work establishes that Mn along with the 5d element Hf increases ferromagnetic interactions in this structure type whereas Fe and 3d/4d elements prefer antiferromagnetic interactions.

In chapter 5, we present that replacing the 4d element Ru by the 5d and 1-valence-electron-richer element Ir drastically increases magnetic anisotropy in $Hf_2MnIr_5B_2$ and $Hf_2FeIr_5B_2$, leading to large coercivities and high ordering temperatures.

Finally, a conclusion integrates all the works presented throughout this Dissertation.

1.5 References:

[1] K. P. Skokov, O. Gutfleisch, *Scripta Mater.,* 2018, *154*, 289–294.

[2] O. Gutfleisch, M. A. Willard, E. Brück, C. H. Chen, S. G. Sankar, J. P. Liu. *Adv. Mater.,* 2011, 23, 821–842.

[3] DiSalvo, F. J. Challenges and opportunities in solid-state chemistry. *Pure Appl. Chem.* 2000, *72*, 1799–1807.

[4] J. J. Croat, J. F. Herbst, R.W. Lee, F. E. Pinkerton, *J. Appl. Phys.,* 1984, *55*(6), 2078–2082.

[5] https://www.energy.gov/sites/prod/files/DOE_CMS2011_FINAL_Full.pdf

[6] M. G. Kanatzidis, K.R. Poeppelmeier, et al. 2008, *Prog. Solid State Chem.*, *36*(1-2), 1–133.

[7] J. P. Scheifers, Y. Zhang, B. P. Fokwa, *Acc. Chem. Res.*, 2017, *50*, 2317–2325.

[8] G. Akopov, M. T. Yeung, R. B. Kaner, *Adv. Mater.*, 2017, 1604506.

[9] W. N. Kang, H. J. Kim, E. M. Choi, C. U. Jung, S. I. Lee, *Science*, 2001, 292, 1521–1523.

[10] Q. Zheng, R. Gumeniuk, H. Rosner, W. Schnelle, Y. Prots, U. Burkhardt, Y. Grin, A. Leithe-Jasper, *J. Phys.: Condens. Matter*, 2015, 27, 415701.

[11] J. Wong, T. Tanaka, M. Rowen, F. Schäfers, B. R. Müller, Z. U. Rek, *J. Synchrotron Radiat.* 1999, 6, 1086 – 1095.

[12] A. N. Broers, *Appl. Phys. Lett.,* 1973, *22*, 610-612.

[13] J.F. Herbst*, Rev. Mod. Phys.*, 1991, 63, 819 – 898.

[14] R. Hasegawa, *J. Non-Cryst. Solids,* 2001, *287,* 405-412.

[15] M. E. McHenry, M. A. Willard, D. E. Laughlin, *Prog. Mater Sci.,* 1999, 44, 291-433.

[16] X. Tan, P. Chai, C. M. Thompson, M. Shatruk, *J. Am. Chem. Soc.* 2013, *135*, 9553–9557.

[17] P. Chai, S. A. Stoian, X. Tan, P. A. Dube, M. Shatruk, *J. Solid State Chem.*, 2015, *224*, 52-61.

[18] S. Hirt, F. Yuan, Y. Mozharivskyj, H. Hillebrecht, *Inorg. Chem.*, 2016, *55*, 9677-9684.

[19] W. Xie, H. Luo, K. Baroudi, J. W. Krizan, B. F. Phelan, R. J. Cava, *Chem. Mater.*, 2015 *27*, 1149-1152.

[20] Y. B. Kuz'ma, Y. P. Yarmolyuk, *J. Struct. Chem.* 1971, *12*, 422-424.

[21] E. Nagelschmitz, W. Jung, *Chem. Mater.* 1998, *10*, 3189-3195.

[22] R. Dronskowski, K. Korczak, H. Lueken, W Jung, *Angew. Chem. Int. Ed.* 2002, *41*, 2528-2532.

[23] Y. Zhang, G. J. Miller, B. P. T. Fokwa, *Chem. Mater.* 2017, 29, 2535-2541.

[24] J. Hafner, *Comp. Chem.* 2008, *29*, 2044-2078.

[25] R. Tank, O. Jepsen, A. Burkhardt, O. K. Andersen, *TB-LMTO-ASA Program, version 4.7.* Max-Plank Institute for Solid-State Research, 1994 Stuttgart, Germany

[26] Chapter by R. Dronskowski in B. Kramer, ed., 2007. *Adv. Solid State Phys.* (Vol. 42). Springer.

[27] A. Landrum, R. Dronskowski, *Angew. Chem. Int. Ed.* 2000, *39*, 1560-1585.

[28] R. Quijano,R. de Coss, D. J. Singh, *Phys. Rev. B,* 2009, *80*, 184103(1-8).

[29] M. D. Kuz'Min, K.P. Skokov, H. Jian, I. Radulov, O. Gutfleisch, *J.Phys.: Condens. Matter*, 2014, *26*, 064205.

[30] R. Skomski, P. Manchanda, P. Kumar, B. Balamurugan, A. Kashyap,D. J. Sellmyer, *IEEE Trans. Magn.*, 2013, *49*(7), 3215-3220.

[31] D. S. Young, B. S. Sachais, L. C. Jefferies, The *Rietveld* method, 1993.

[32] J. Rodriguez-Carvajal, *In satellite meeting on powder diffraction of the XV congress of the IUCr*, 1990, *127,* Toulouse, France.

[33] CrysAlisPro 1.171.39.38b , Rigaku Oxford Diffraction, 2017

[34] G. M. Sheldrick, *Acta Crystallogr., Sect. A: Found. Crystallogr.* 2008, *A64*, 112.

[35] L. J. Farrugia, WINGX, a windows program for crystal structure analysis. University of Glasgow, Glasgow, 1998.

Chapter 2

Unexpected Trend Deviation in Isoelectronic Transition Metal Borides $A_3T_5B_2$ (A = group 4, T = group 9): $Ti_3Co_5B_2$- versus Perovskite-Type Studied by Experiments and DFT Calculations

Reprinted (adapted) with permission from: P. Shankhari, J. P. Scheifers, M. Hermus, K. Yubuta, B. P. T. Fokwa. " Unexpected Trend Deviation in Isoelectronic Transition Metal Borides $A_3T_5B_2$ (A = group 4, T = group 9): $Ti_3Co_5B_2$- vs. Perovskite-Type Studied by Experiments and DFT Calculations.", 2017, *Z. Anorg. Allg. Chem.*, *643*, 1551-1556 (DOI: 10.1002/zaac.201700271)

2.1 Introduction

$Ti_3Co_5B_2$ is a versatile structure type among metal-rich borides including ternary ($A_3T_5B_2$), quaternary ($A_2MT_5B_2$) and quinary ($A_2M(TT')_5B_2$) phases in its large family.[1, 2] The ternary compounds, $A_3T_5B_2$, are structurally built by face-connected trigonal, tetragonal and pentagonal prisms of *T*-atoms (electron-rich and relatively small transition metals such as Co, Rh, Ir and Ru) while *A*-atoms (relatively large early transition metals such as Sc, Ti, Nb, Zr, Hf, Ta) reside inside the tetragonal and pentagonal prisms and the boron atoms are located within the trigonal prisms (Figure 2.1, left). The unique crystal chemistry of this structure type often allows selective and site-specific substitution of A-atoms by other elements—including 3d magnetically active elements—which then can introduce magnetic ordering in many quaternary and quinary phases.[3, 4] Such quaternaries and quinaries have been studied extensively through both theoretical and experimental investigations in recent years for their interesting itinerant magnetism.[3-11] Although more than sixty

intermetallic compounds with $Ti_3Co_5B_2$-type structure are known, only eight ternaries have been found since the first report of $Ti_3Co_5B_2$ in 1971 by Kuzma [2] *et. al*. There could be multiple reasons behind the small number of ternary phases e.g. the complex phase diagrams of many metal-rich borides or the relative energy of formation of the $Ti_3Co_5B_2$-type phases compared to other structure types, such as perovskites (AT_3B), under similar reaction conditions. Moreover, only a few of these eight have been unambiguously characterized by single-crystal analysis.[12] For example, only powder X-ray diffraction data of $Hf_3Ir_5B_2$ and coarse single-crystal refinement data of $Ti_3Co_5B_2$ were reported long ago which do not comply with today's standard of analysis as neither anisotropic refinement of the atomic displacement parameters nor mixed-occupancy refinements were carried out.[2, 13]

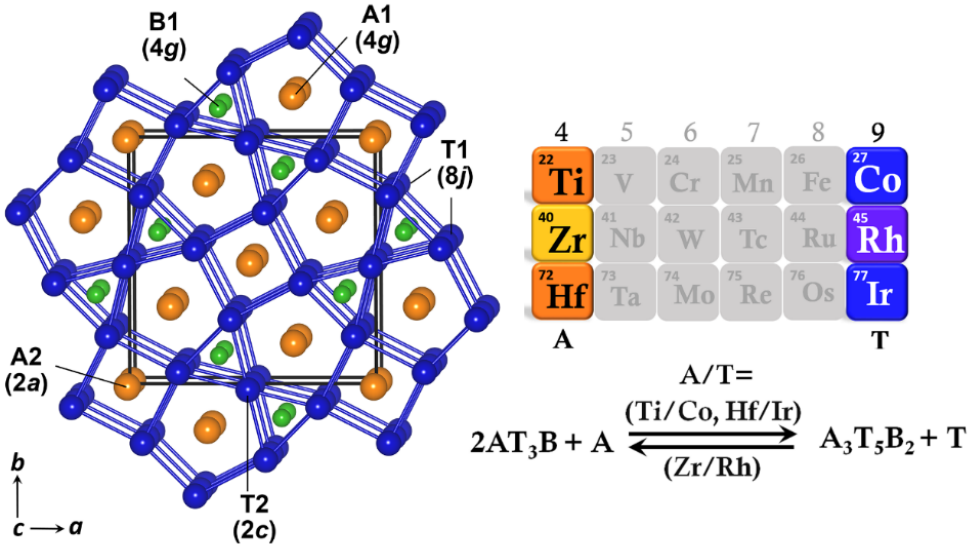

Figure 2.1. Perspective view of the crystal structure of the ternary $A_3T_5B_2$ compounds (space group *P4/mbm*, no. 127) viewed along [001].

Another class of metal-rich borides with an identical metal to boron ratio (M:B) as the $Ti_3Co_5B_2$-type is the (anti-) perovskite-type with the general formula AT_3B. These compounds are also described as Cu_3Au-type structure (AT_3) with interstitial boron atoms occupying the center of the T_6-octahedra.[14] In most cases, a solubility range for boron can be observed, especially if the binary Cu_3Au-type exists.[15] In contrast, there are also ternary boron-deficient perovskites such as $ScNi_3B_{0.5}$, for which the binary intermetallic Cu_3Au-type phase does not exist.[16] Per systematic studies, Takeya et al. discovered that the stability and the boron solubility limits in this class of compounds depend on the valence electron count (VEC).[15] In the last couple of years, the stable VEC-range was correlated with the *Fermi*-level (E_F) being located in a deep pseudo-gap in the density of states (DOS). Moreover, vacancy ordering was observed for several $AT_3B_{0.5}$ perovskites, resulting in a space group change from *Pm*-3*m* to *Fm*-3*m*.[17-19] The presence of a deep pseudo-gap is also a common feature found in the DOS of $Ti_3Co_5B_2$-type borides [9], a further similarity with the boron perovskites. The similarities in the M:B ratio and the electronic structure suggest that these two structure types may compete during formation. In this work, we report the first synthesis of bulk $Ti_3Co_5B_2$ and the single-crystal structure determination of $Hf_3Ir_5B_2$. Furthermore, we applied DFT calculations to understand the unexpectedly failed synthesis of "$Zr_3Ir_5B_2$" under similar synthetic conditions, as a perovskite-like phase is found instead.

2.2 Results and discussion

2.2.1 Phase Analysis

After arc-melting the elemental components, the phase analyses of the recorded powder X-ray diffraction data of the resulting products were done by the *Rietveld* [20] refinement method using FullPROF.[21] Figure 2.2 shows a plot of a typical refinement for the reaction mixture of 3Hf:5Ir:2B. Similar refinements for the samples with the starting compositions 2Ti:6Co:2B and 3Zr:5Rh:2B are provided in the supporting information, Figure S2.1. The results of the *Rietveld* refinements are summarized in Table 2.1. The 2:6:2 mixture of Ti, Co, and B formed the $Ti_3Co_5B_2$-type structure and a face-centered, Co-rich alloy as side phase (Table 2.1, Figure S2.1).

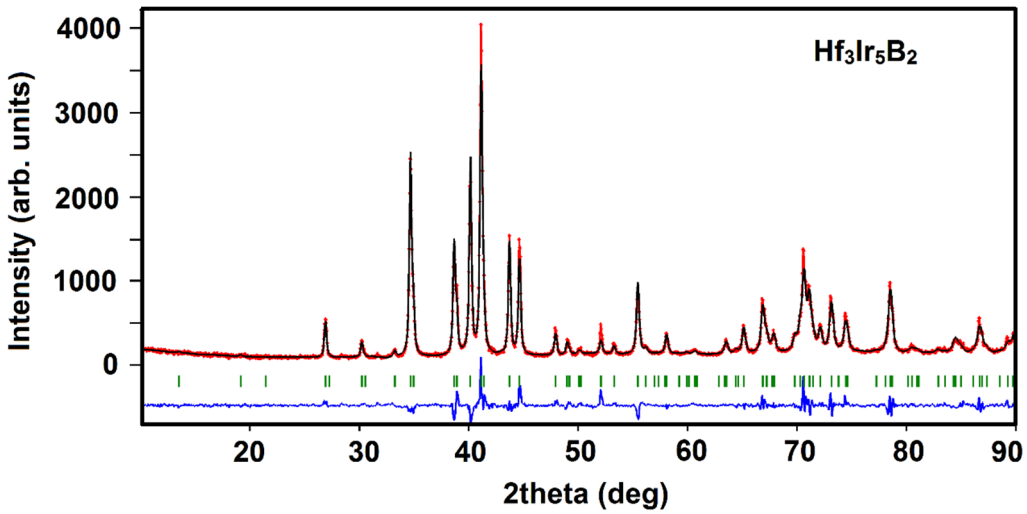

Figure 2.2. Observed (red) and calculated (black) powder X-ray diffraction pattern of $Hf_3Ir_5B_2$, the position of the Bragg's reflections for $Ti_3Co_5B_2$ type structure (green) and the difference curve (blue) obtained from *Rietveld* refinement.

In contrast, a compound with the $Ti_3Co_5B_2$-type structure was not obtained under similar synthetic conditions (arc-melting) for both starting compositions 2Zr:6Rh:2B or 3Zr:5Rh:2B. Instead, the powder diffraction pattern (in both cases) was similar to that of a

boride perovskite at first glance. Additionally, ZrB_2 was found as a minor phase. A closer look at the main compound revealed a powder diffraction pattern that would fit either a cubic face-centered Zr-Rh alloy or a cubic perovskite structure with lattice parameter a = 4.016(1) Å (Figure S2.1). The signal-to-noise ratio (SNR) for some less intense but characteristic peaks of the primitive perovskite structure are very small (SNR = 1.5). Indeed, an optical examination of the powder diffractogram in the 2Θ range $20° < 2\Theta < 35°$ indicated few small reflections, which matched the diffraction pattern of the perovskite structure. In addition, the obtained lattice parameter was much larger than it should have been for pure Rh (a = 3.803 Å) and just slightly smaller than that measured for $ZrRh_3B$ (a = 4.045 Å).[13] Therefore, this phase is very likely a poorly crystallized, boron-deficient perovskite, $ZrRh_3B_{1-x}$. Interestingly, the 3:5:2 mixture of Hf, Ir, and B gave the single-phase $Hf_3Ir_5B_2$ ($P4/mbm$, no. 127) with a = 9.252(1) Å and c = 3.3111(1) Å. These values are in good agreement with the lattice parameters a = 9.261(1) Å and c = 3.323(3) Å reported by Rogl et al.[13] from powder XRD as well as with those found for the single-crystal data solved for the first time (given later, Table 2.2).

Table 2.1. Details of the *Rietveld* refinements for different samples.

Loaded Composition	2Ti:6Co:2B	3Zr:5Rh:2B	3Hf:5Ir:2B
Main compound	$Ti_{2.4(2)}Co_{5.6(2)}B_2$	$ZrRh_3B_{1-x}$	$Hf_3Ir_5B_2$
Space group, *Z*	*P4/mbm* (no. 127), *2*	*Pm*-3*m* (no. 221), 1	*P4/mbm* (no. 127), *2*
***a* (Å)**	8.449(2)	4.016(1)	9.252(1)
***c* (Å)**	3.016(1)	-	3.3111(4)
***V* (Å^3)**	215.3(1)	64.77(1)	283.49(3)
2*Θ*-range (°)	3 - 63	10 - 90	10 - 90
Refinement method	Least squares method		
Profile function	Pseudo-*Voigt*		
R_{Bragg}	6.90	3.27	5.75
Fraction (wt.-%)	37.6(8) [a]	87(2)	100
Byproducts, Fraction (wt.-%)	Co, 28.2(7)[a] SiO_2, 34.2(8)[a]	ZrB_2, 9.8(6) ZrO_2, 3.4(4)	-

[a] relative weight fractions due to unidentified reflections in the diffraction pattern.

2.2.2 Single-Crystal Structure Determination:

A single crystal from each of the arc-melted and crushed samples of 2Ti:6Co:2B and 3Hf:5Ir:2B was isolated and measured for single-crystal structure determination. The intensities were corrected with respect to absorption using a semi-empirical procedure.[22] The crystal structure was solved by direct methods and refined by using the SHELX program package.[23] The positions of the metal atoms were obtained by direct methods and the boron position was found after a few cycles of the full-matrix least-squares refinement (based on F^2) in the electron density map. The refinements confirmed the $Ti_3Co_5B_2$ structure type (P4/mbm, space group no. 127) for both crystals. The single-crystal refinement results, atomic coordinates and selected interatomic distances for both phases

are given in Table 2.2, Table 2.3, and Table 2.4 respectively. The refined lattice parameters for $Ti_3Co_5B_2$, a = 8.3912(2) and c = 3.0095(1) were nearly identical to those obtained from powder data (see above) but were significantly smaller than those reported by Kuzma et al.[13] (a = 8.489 Å and c = 3.038 Å) indicating a different composition. The $Ti_3Co_5B_2$ composition was reported by Kuzma et al. and resulted from a single crystal found while attempting to synthesize "TiCoB", a composition poorer in Co than $Ti_3Co_5B_2$.[2] In our synthesis, however, a greater amount of Co was necessary to quantitatively synthesize the $Ti_3Co_5B_2$ phase, thus a higher amount of Co can be expected if compared to the single crystal of Kuzma et al. Indeed, the composition $Ti_{2.4(2)}Co_{5.6(2)}B_2$ was obtained from our powder XRD refinement and confirmed by single-crystal refinement as $Ti_{2.48(1)}Co_{5.52(1)}B_2$ when refining a Ti/Co mixed occupancy of the site 2*a*. This difference in composition corroborates very well with the difference between the lattice parameters, because the smaller Co atoms partially replace the larger Ti atoms in our sample, thus causing smaller lattice parameters. This result suggests that a phase width exists for this phase, with a solubility limit of Co on the Ti-2*a* position of x = 0.52(1) because Co was used in excess during synthesis and found in the side phase. Therefore, this phase is better described as $Ti_3Co_5B_2$ (x = 0 – 0.5). A perspective view of the crystal structure with general composition $A_3T_5B_2$ is shown in Figure 2.1. In the stoichiometric composition $A_3T_5B_2$, there are two *Wyckoff* positions for A: 2*a*, 4*g* (inside tetragonal and pentagonal prisms, respectively), two *Wyckoff* positions for T: 2*c*, 8*j* (build network of trigonal, tetragonal and pentagonal prisms) and one *Wyckoff* position for boron: 4*g* (inside trigonal prisms). We also checked for mixed occupancy at other Ti and Co sites, but no stable refinement could be achieved.

The composition $Ti_{2.48(1)}Co_{5.52(1)}B_2$ resembles the other ternary compounds $Zr_{2.86(5)}Ru_{5.14(5)}B_2$ and $Hf_{2.83(2)}Ru_{5.17(2)}B_2$ with $Ti_3Co_5B_2$-type structure, for which mixed occupancy was also found at the 2*a* site.[12] Our understanding is that the *T*-atoms being smaller than *A*-atoms can easily occupy the 2*a* site within the tetragonal prisms. The final refinement converged with very good *R* values (R_1; wR_2 = 0.0213; 0.0385 for all 539 reflections). In $Ti_{2.48(1)}Co_{5.52(1)}B_2$ the interatomic distances are very similar to those reported in Kuzma's work. For example, the Co-B distances were reported to be 2.05 – 2.09 Å compared to 2.076(1) – 2.086(1) Å obtained in our refinement.[2]

$Hf_3Ir_5B_2$ was synthesized as stoichiometric compound according to our *Rietveld* refinement, a result confirmed by single-crystal refinement. We were not able to perform a stable refinement with mixed occupancy for this phase and free refinements of the metal-site occupancies indicate that these sites are fully occupied within an error margin of 2σ, leading to a stoichiometric formula. The lattice parameters observed for $Hf_3Ir_5B_2$, *a* = 9.264(2) Å and *c* = 3.3070(5) Å are very close to those reported for the powder XRD data by Rogl et al. (*a* = 9.261(1) Å and *c* = 3.323(3) Å).[13] When we compared these values to those of $Hf_{2.83}Ru_{5.17}B_2$ [12] (*a* = 9.4389(3) Å and *b* = 3.1030(2) Å), which contains the smaller Ru atoms instead of Ir, we expected the lattice parameters to be larger in $Hf_3Ir_5B_2$. Although we observed an elongation (6.6%) of the unit cell in the *c*-direction, it was compressed (1.8%) in the *a*- direction. Nevertheless, the resulting unit cell volume is larger for the Ir-based phase, as expected. The compression of the unit cell parameter in the *ab*-plane was also reflected in the Ru-Ru and Ir-Ir distances in the 3-dimensional framework of prisms. The Ru-Ru bond distances in the *ab*-plane in $Hf_{2.83}Ru_{5.17}B_2$ range from 2.734(2)

Å to 3.094(2) Å, whereas the Ir-Ir distances for $Hf_3Ir_5B_2$ in the *ab*-plane are smaller, 2.6740(6) – 3.0341(7) Å. The metal-boron distances are the shortest interatomic distances in $Hf_3Ir_5B_2$, 2.264(19) – 2.282(19) Å and are larger than those found in $Hf_{2.83}Ru_{5.17}B_2$ [2.207(4) – 2.250(9)]. The final refinement cycles of $Hf_3Ir_5B_2$ converged with *R* values: R_1; $wR_2 = 0.0397$; 0.0279 for all 410 reflections. We also observed unusually large thermal displacement parameters for the Ir atoms in the *c*-direction. We took SAED images (See SI, Figure S2.2) to check for small structural distortions that would cause any change (superstructure or diffuse scattering) along the *c*-direction. Those images did not show any indication for a deviation from the regular unit cell. We conclude that the unusual thermal displacement parameters are an artifact of the semi-empirical absorption correction.

Table 2.2. Single crystal structure data for $Ti_{2.48}Co_{5.52}B_2$ and $Hf_3Ir_5B_2$.

Refined Composition	$Hf_3Ir_5B_2$	$Ti_{2.48(1)}Co_{5.52(1)}B_2$
Space group (No.), *Z*	*P4/mbm* (127), 2	
Formula weight (g/mol)	1518.09	465.75
Wavelength (Å)	0.71073 (Mo-K_α)	
θ-range (°)	4.92-36.12	3.43-45.62
***hkl* range**	$-15 \le h \le 14$	$-16 \le h \le 16$
	$-15 \le k \le 15$	$-16 \le k \le 16$
	$-5 \le l \le 5$	$-6 \le l \le 6$
***a* (Å)**	9.264(2)	8.3912(2)
***c* (Å)**	3.3070(5)	3.0095(2)
***V* (Å^3)**	283.84(9)	211.906(9)
***F*(000)**	1222	427
Crystal size (mm^3)	0.04x0.02x0.02	0.09x0.10x0.17
No. of reflections; R_{int}	5619; 0.0738	17901; 0.0587
No. of independent reflections	410	539
No. of obs. reflections $I > 2\sigma(I)$	351	499
No. of Parameters	18	22
Absorption coefficient μ (mm^{-1})	171.164	25.278
Difference peak/hole (e Å^{-3})	3.011/-4.093	1.251/-0.976
GooF	1.123	1.125
R_1; wR_2 (all *I*)	0.0397; 0.0561	0.0213; 0.0385
R_1; wR_2 ($I > 2\sigma$)	0.0279; 0.0527	0.0180; 0.0376
ICSD depository number	433429	433428

Table 2.3. Atomic coordinates, site occupation factors (SOF), and equivalent displacement parameters (isotropic for boron) for $Ti_{2.48}Co_{5.52}B_2$ and $Hf_3Ir_5B_2$.

Atom label	*Wyckoff* position	*x*	*y*	*z*	SOF	*U*eq
$Ti_{2.48}Co_{5.52}B_2$						
Co1	8*j*	0.06961(3)	0.21605(3)	0.5	1	0.00359(6)
Co2	2*c*	0	0.5	0.5	1	0.00241(8)
Ti1	4*g*	0.32419(3)	0.17581(3)	0	1	0.00312(7)
Ti2	2*a*	0	0	0	0.48(2)	0.0042(1)
Co3	2*a*	0	0	0	0.52(2)	0.0042(1)
B1	4*g*	0.1217(2)	0.3783(2)	0	1	0.0057(4)
$Hf_3Ir_5B_2$						
Ir1	8*j*	0.07133(5)	0.22032(5)	0.5	1	0.0087(2)
Ir2	2*c*	0	0.5	0.5	1	0.0091(2)
Hf1	4*g*	0.32339(6)	0.17661(6)	0	1	0.0085(2)
Hf2	2*a*	0	0	0	1	0.0081(2)
B1	4*g*	0.120(3)	0.380(3)	0	1	0.040(8)

Table 2.4. Selected interatomic distances in $Ti_{2.48(1)}Co_{5.52(1)}B_2$ and $Hf_3Ir_5B_2$ obtained from single crystal refinement. All distances are in Å unit.

$Ti_{2.48(1)}Co_{5.52(1)}B_2$			**$Hf_3Ir_5B_2$**		
Within pentagonal prisms					
Hf1	Ir1	2.8898(7)- 2.9870(7)	Ti1	Co1	2.6347(3)- 2.7072(3)
Hf1	Ir2	2.8440(5)	Ti1	Co2	2.5724(2)
Within tetragonal prisms					
Hf2	Ir1	2.7087(5)	Ti2/Co3	Co1	2.4274(2)
Within trigonal prisms					
B1	Ir1	2.264(19)	B1	Co1	2.0758(12)
B1	Ir2	2.282(19)	B1	Co2	2.0857(12)
Network of prisms					
Ir1	Ir1	2.7298(7) - 3.0341(7)	Co1	Co1	2.5435(4) - 2.6936(4)
Ir1	Ir2	2.6740(6)	Co1	Co2	2.4532(3)
Ir2	Ir2	3.3070(5)	Co2	Co2	3.0095(1)
Hf1	Hf1		Ti2/Co3	Ti2/Co3	3.0095(1)

2.2.3 Electronic structure

The electronic structure of $Hf_3Ir_5B_2$ was analyzed using the Stuttgart version of the tight-binding, linear muffin-tin orbital (TB-LMTO) method with the atomic spheres approximation.[24] The experimentally determined lattice parameters and atomic coordinates of $Hf_3Ir_5B_2$ were optimized by the projector augmented wave method of Blöchl[25] coded in the Vienna ab initio simulation package VASP[26]. More details are provided in the experimental section. The total density of states (DOS) plot (Figure 2.3) revealed that the Fermi level (E_F) falls in a deep pseudogap, ranging from −2.0 eV up to +1.0 eV, typical behavior for this structure type.[12] However, the presence of a significant number of states at E_F indicates metallic behavior, as expected for this metal-rich phase. The presence of the widespread pseudogap also indicates that other electronically stable phases may be derived from $Hf_3Ir_5B_2$ via elemental substitutions, if the Fermi Level shifted according to the rigid band model remains inside the pseudogap. The partial DOS of Ir, Hf, and B were also calculated (Figure 2.3). The partial DOS revealed that the Ir states dominate below E_F and the Hf states dominate above the E_F whereas the boron states are mostly found well below E_F.

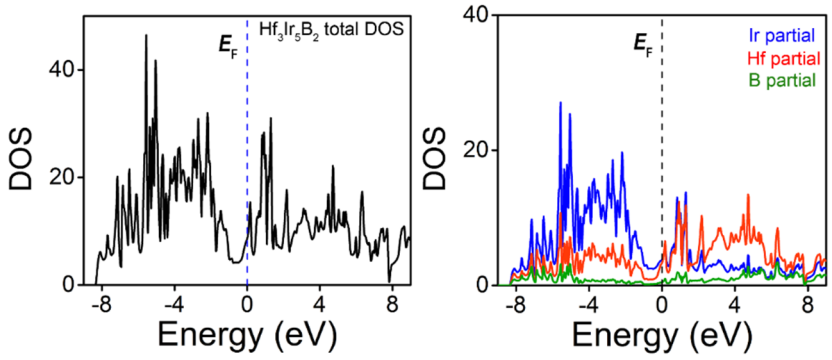

Figure 2.3. Total (left) and partial (right) density of states (DOS) plots of $Hf_3Ir_5B_2$.

We find that both Ti+3Co+B and Hf+3Ir+B mixtures form compounds with the $Ti_3Co_5B_2$-type structure, whereas the Zr+3Rh+B mixture forms a perovskite-like compound. All three starting mixtures are isoelectronic and would fall into the reported valence electron count (VEC) range for boron perovskites. In the Ti- and Hf-based cases the binary intermetallic with Cu_3Au-type structure exist, but no boron perovskites were formed during the reactions, independent of the starting mixture (2:6:2 or 3:5:2). Unexpectedly, the Zr+3Rh+B mixture breaks the trend as it does not form a compound with the $Ti_3Co_5B_2$-type structure but a perovskite-like phase instead.

To understand these different behaviors of the elements in the same group of the periodic table, we compared some of their basic properties such as the metallic radii and the electronegativity: The ratio of the metal radii and the difference of the electronegativity are extremely similar for Ti/Co and Hf/Ir, but they are significantly different from those of Zr/Rh (see Table 2.4). In addition, the Gibbs free energies of formation for both the $A_3T_5B_2$ and perovskite-type structures were used to examine the stability of the two structures. We calculated the free energy change of the following reaction at 0 K.

$$2AT_3B + A = A_3T_5B_2 + T \qquad (1)$$

Table 2.5. Comparison of the experimentally found structures with the ratios of the atomic radii of *A* and *T*, the difference in the electronegativity (EN) of *A* and *T* and the Gibbs free energy at 0 K [ΔGf(0 K)] obtained from VASP.

Elements A and T	*A* = Ti, T = Co	*A* = Zr, T = Rh	*A* = Hf, T = Ir
Radii ratio r_A/r_T	1.156	1.182	1.153
ΔEN = EN(A) - EN(T)	0.4	0.3	0.4
ΔG_f(0K) [eV/f.u.]	-2.083	-0.128	-2.482
Obtained structure type	$Ti_3Co_5B_2$	Perovskite-like	$Ti_3Co_5B_2$

The free energy changes for reaction (1) was obtained through VASP total energy calculations. Starting from the known single-crystal data (wherever available) the structural parameters were allowed to relax before the single point total energy calculations. For Ti, Zr, Hf, and Co, the energies of the *hcp* structures were calculated, while *fcc* crystal structures were used for Rh and Ir. According to the calculated results (see Table 2.5), the formation of $Ti_3Co_5B_2$ and $Hf_3Ir_5B_2$ is highly favored as evident by large negative Gibbs free energies of formation (more than -2.0 eV). In contrast, it is found that the $Ti_3Co_5B_2$-type structure is only slightly favored over the perovskite structure (by only -0.128 eV) for the Zr+Rh+B mixture. Thus, this theoretical result would also predict the formation of the $Ti_3Co_5B_2$-type structure for the Zr+Rh+B mixture, which is contrary to the experimental result. However, the energy difference is very small, and the Gibbs free energy is calculated at 0 K, thus it may be possible that $ZrRh_3B$ is kinetically stabilized or that it is favored under the specific high-temperature reaction conditions.

2.3 Conclusion

We have synthesized bulk $Ti_3Co_5B_2$ for the first time and found a significant mixed occupancy of Ti and Co on the 2*a* site, leading to its reformulation as $Ti_{3-x}Co_{5+x}B_2$ (x = 0 – 0.5). Moreover, we report the first single-crystal data on the isoelectronic $Hf_3Ir_5B_2$ with $Ti_3Co_5B_2$-type structure. The corresponding mixture of Zr, Rh, and B, however, did not form a compound in the $Ti_3Co_5B_2$-type structure under the same reaction conditions. We have found out that the radii ratio r_A/r_T and the electronegativity difference play a great role in understanding this unexpected trend. DFT calculations also provide further support for

this trend, as the Gibbs free energy of formation greatly favors the $Ti_3Co_5B_2$-type structure for $Ti_3Co_5B_2$ and $Hf_3Ir_5B_2$.

2.4 Experimental Section

Highly pure powders of the elements (> 99.5% purity for Ti, Zr, Hf, Co, Rh, Ir and 99% boron, Hf purity includes Zr nominal 2-3.5%) were purchased from Alfa Aesar. The powders of A, T, and boron (*A* = Ti, Zr or Hf; *T* = Co, Rh or Ir; *A* and *T,* being in the same period of the periodic system) were mixed in the ratios 2:6:2 and 3:5:2 and pressed into pellets. Pellets that contained an air-sensitive metal were prepared inside an N_2-filled glovebox. Two pellets were prepared for each composition and one of each was arc-melted under Ar for a short time and flipped upside down just once, while the other set of pellets was re-melted several times. The obtained beads showed metallic luster and were stable in air. They were crushed and ground to powders. The samples were analyzed using a MiniFlex 600 powder X-ray diffractometer by Rigaku with λ(Cu-Kα) = 1.543 Å. The powder X-ray diffraction data for the samples containing Co were gathered on a STOE STADI MP diffractometer equipped with a position-sensitive detector (PSD), using monochromatized Mo-$K\alpha_1$ radiation (λ = 0.71073 Å) to avoid fluorescence. Wherever possible, suitable single crystals were isolated manually, fixed on top of glass capillaries and X-ray data were collected on a Bruker SMART APEX diffractometer equipped with a graphite monochromatized radiation [λ(Mo-$K\alpha_1$) = 0.71073 Å].

Samples for TEM observations were prepared by dispersing finely crushed $Hf_3Ir_5B_2$ on holey carbon films. Selected area electron diffraction (SAED) patterns were obtained using a 200 kV electron microscope (JEOL JEM-2000EXII).

All VASP calculations employed the generalized gradient approximation (GGA) with exchange and correlation treated by the Perdew-Burke-Enzerhoff (PBE) functionals.[27] The convergence threshold for structural relaxation was set to be 0.02 eV/Å in force. The cutoff energy for the plane wave calculations was set to 500 eV and the Brillouin zone integrations were carried out using a *k*-point mesh of 5 × 5 × 15 for $A_3T_5B_2$, 9 × 9 × 9 for AT_3B, *fcc* and *hcp* unit cells.

2.5 Supporting Information

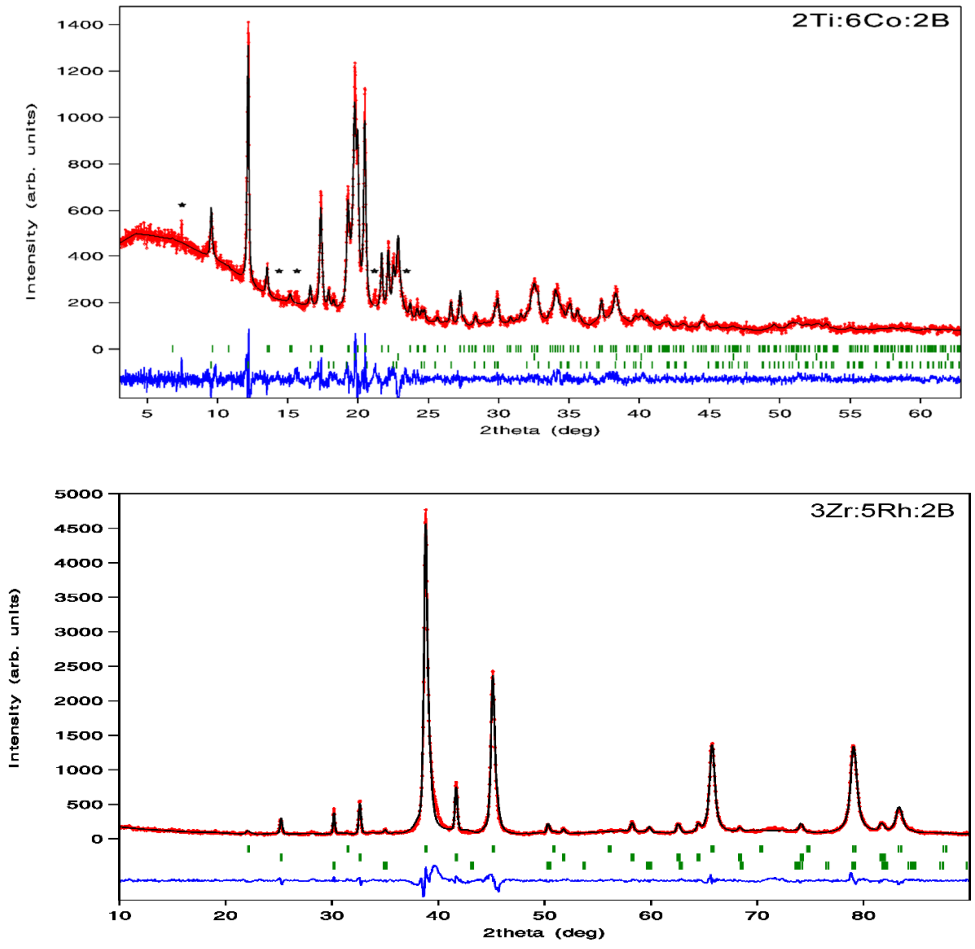

Figure S2.1. *Rietveld* refinement of 2Ti:6Co:2B (top) and 3Zr:5Rh:2B (bottom).

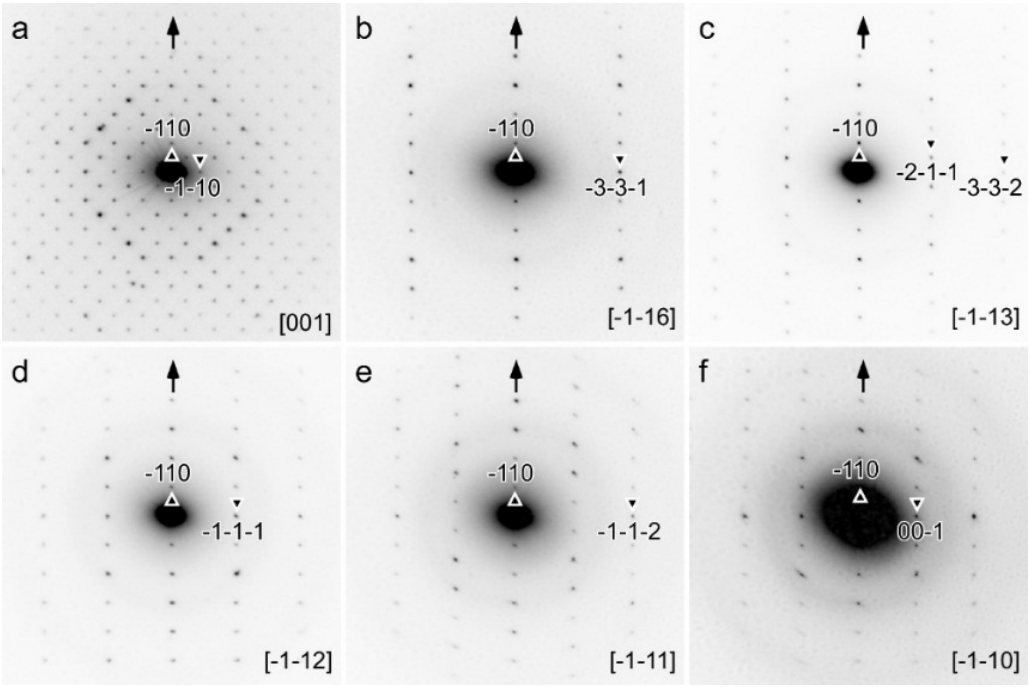

Figure S2.2. SAED images of $Hf_3Ir_5B_2$.

2.6 References

[1] a) B. P. T. Fokwa, *Eur. J. Inorg. Chem.* 2010, *2010*, 3075-3092; b) J. P. Scheifers, Y. Zhang, B. P. T. Fokwa, *Acc. Chem. Res.* 2017, *50*, 2317-2325.

[2] Y. B. Kuz'ma, Y. P. Yarmolyuk, *J. Struct. Chem.* 1971, *12*, 422-424.

[3] E. Nagelschmitz, W. Jung, *Chem. Mater.* 1998, *10*, 3189-3195.

[4] R. Dronskowski, K. Korczak, H. Lueken, W Jung, *Angew. Chem. Int. Ed.* 2002, *41*, 2528-2532.

[5] B. P. T. Fokwa, H. Lueken, R. Dronskowski, *Chem. Eur. J.* 2007, *13*, 6040-6046.

[6] G. D. Samolyuk, B. P. T. Fokwa, R Dronskowski, G. J. Miller, *Phys. Rev. B.* 2007, *76*, 094404.

[7] B. P. T. Fokwa, H Lueken, H. R. Dronskowski, *Eur. J. Inorg. Chem.* 2011, 2011, 3926-3930.

[8] M. Hermus, B. P. T. Fokwa, *Z. Anorg. Allg. Chem.* 2011, *637*, 947-954.

[9] M. Hermus, M. Yang, D. Grüner, F. J. DiSalvo, B. P. T. Fokwa, *Chem. Mater.* 2014, *26*, 1967-1974.

[10] J. Brgoch, S. Yeninas, R. Prozorov, G. J. Miller, *J. Solid State Chem.* 2010, *183*, 2917-2924.

[11] Y. Zhang, G. J. Miller, B. P. T. Fokwa, *Chem. Mater.* 2017, 29, 2535-2541.

[12] M. Hermus, B. P. T. Fokwa, *Eur. J. Inorg. Chem.* 2014, *2014*, 3085-3094.

[13] P. Rogl, H. Nowotny, *J. Less-Comm. Met.* 1979, *67*, 41-50.

[14] K. Yubuta, A. Nomura, K. Nakajima, T. Shishido, *J. Alloys Compd.* 2006, *426*, 308-311.

[15] H. Takeya, T. Shishido, *J. Less-Comm. Met*. 1987, *134,* 263-273.

[16] T. Shishido, K. Kudou, T. Sasaki, S. Okada, J. Ye, K. Iizumi, S. Kohiki, *J. Alloys Compd.* 2004, *383*(1), 294-297.

[17] B. P. T. Fokwa, B. Eck, R. Dronskowski. *Z. Kristallogr. Cryst. Mater.* 2006, *221*, 445-449.

[18] M. Hermus, B. P. T. Fokwa, *J. Solid State Chem.* 2010, *183*, 784-788.

[19] I. Zeiringer, J. G. Sereni, M. G. Berisso, K. Yubuta, P. Rogl, A. Grytsiv, E. Bauer, *Mater. Res. Express,* 2014, *1*, 016101.

[20] D. S. Young, B. S. Sachais, L. C. Jefferies, 1993, The *Rietveld* method.

[21] J. Rodriguez-Carvajal, *In satellite meeting on powder diffraction of the XV congress of the IUCr,* 1990, *127*, Toulouse, France.

[22] G. M. Sheldrick, SADABS, Version 2. Multi-Scan Absorption Correction Program. University of Göttingen: Göttingen, Germany, 2001.

[23] G. M. Sheldrick, *Acta Crystallogr., Sect. A: Found. Crystallogr.* 2008, *A64*, 112.

[24] R. Tank, O. Jepsen, A. Burkhardt, O. K. Andersen, TB-LMTO-ASA Program, version 4.7. Max-Plank Institute for Solid-State Research, 1994 Stuttgart, Germany.

[25] P. E. Blöchl, *Phys. Rev. B: Condens. Matter Mater. Phys.* 1994, *50*, 17953-17979.

[26] G. Kresse, D. Joubert, *Phys. Rev. B: Condens. Matter Mater. Phys.* 1996, *54*, 11169-11186.

[27] J. P. Perdew, K. Burke, M. Ernzerhof*, Phys. Rev. Lett.* 1996, *77*, 3865 –3868.

Chapter 3

Unexpected Competition Between Antiferromagnetic and Ferromagnetic States in $Hf_2MnRu_5B_2$: Predicted and Realized

Reprinted (adapted) with permission from: P. Shankhari, Y. Zhang, D. Stekovic, M. E. Itkis, B. P. T. Fokwa. " Unexpected Competition Between Antiferromagnetic and Ferromagnetic States in $Hf_2MnRu_5B_2$: Predicted and Realized.", 2017, *Inorg. Chem.*, *56* (21), 12674-12677 (DOI: 10.1021/acs.inorgchem.7b01758)

3.1 Introduction

Recent research efforts in solid-state and materials chemistry are concerned with the design and prediction of new compounds and materials. However, it is difficult, in general, to design a phase a priori, and in most cases, the ability to broadly design and predict new phases with new structures remains a challenge.[1-4] On the one hand, "materials design" for a known structure type is possible, e.g., by isoelectronic elemental substitutions, intercalation of species into solids, or synthesis of coordination solids based on solid-state structures to achieve interesting physical properties.[5] As proposed by Canfield, [6] to design a material that will exhibit a specific property, there often needs to be some model or idea of which parameters are important and how to influence or control them. This guiding principle is often an admixture between theory and practical concerns, such as which elements or compounds can readily—and safely—be used: For an intermetallic material with magnetic properties, for example, the tendency is to look at compounds with 3d magnetically active transition metals and/or rare-earth (4f) elements.[6]

Transition-metal borides crystallizing in several unique structures have been the focus of extensive research interest in recent years because of their interesting itinerant magnetic properties.[7-12] $Ti_3Co_5B_2$ [13] is one such prolific structure type that has produced many compounds, including ternaries ($A_3T_5B_2$), quaternaries ($A_2MT_5B_2$), and quinaries [$A_2M(TT')_5B_2$]. The ternary variants $A_3T_5B_2$ are formed by face-connected trigonal, tetragonal, and pentagonal prisms of *T* atoms (generally electron-rich and smaller transition metals such as Co, Rh, Ir, and Ru). The *A* atoms (relatively large atoms such as Mg, Sc, Ti, Zr, and Hf) reside inside both tetragonal and pentagonal prisms, while the B atoms are coordinated within the trigonal prisms [14] In quaternaries (see Figure 3.1a) and quinaries, magnetically active M atoms sitting inside the tetragonal prisms build chains along [001] with intrachain M–M distances in the range 2.90–3.10 Å (see Figure 3.1b) suitable for magnetic interactions. Both experimental and theoretical studies [15-21] have been conducted extensively on the magnetic properties of such quaternaries and quinaries and have revealed that magnetic *M* atoms in conjunction with the electronic contributions from T atoms can drastically influence the magnetic properties. For example, in the quinary series $Sc_2FeRh_{5-x}Ru_xB_2$ and $Sc_2FeIr_{5-x}Ru_xB_2$, the evolution of magnetic interactions has been observed experimentally and reproduced theoretically as a function of the valence electron count (VEC): Preferred antiferromagnetic (AFM) coupling was found below VEC = 62, while preferred ferromagnetic (FM) coupling was found at VEC = 63 or higher.[17, 18, 21] In general, Fe-based magnetic materials have been studied, and it is understood that, in these phases, dominating FM interactions are found in systems with valence-electron-richer 4d/5d transition metals (T = Rh, Ir), while dominating AFM interactions

are observed in those containing valence-electron-poorer 4d transition-metal (T = Ru)-based systems. The Mn-based compounds studied to date are all Rh- or Ir-rich, and their magnetic properties fit well within the studied VEC range. However, no Mn-based Ru-rich phase of this structure type is known which has been magnetically characterized in detail. Mn has produced some important magnetic materials such as Mn_3GaC, hard ferromagnets MnBi [22], Mn_2Ga_5 [23], and MnB [24] even though its ground state is AFM. Herein, we report on the design of the first Mn-based Ru-rich phase, $Hf_2MnRu_5B_2$, predicted theoretically to show competing AFM and FM ordering states and successfully synthesized and investigated for its magnetic properties.

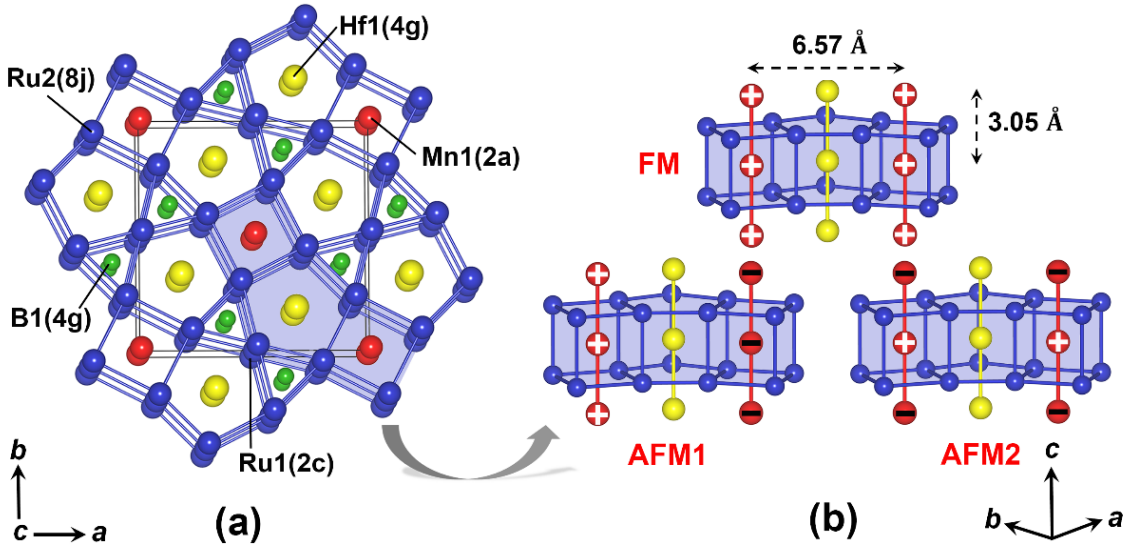

Figure 3.1. **(a)** Representative view of the structure of $Hf_2MnRu_5B_2$ along [001] and **(b)** different magnetic models for Mn chains. The + and – signs represent opposite types of spins

3.2 Results and Discussion

The recipe for designing this phase was clear: It should be Ru-rich and should incorporate Mn along with a 4d or 5d element. Because $Hf_3Ru_5B_2$ was already reported, [25] this phase

was used as the starting point. At first, we employed density functional theory (DFT) calculations to investigate the electronic structure, bonding, and magnetic interactions in $Hf_2MnRu_5B_2$. Geometry optimization was performed on a nonmagnetic (NM) model of $Hf_2MnRu_5B_2$ using the projector-augmented wave method of Blöchl [26, 27] coded in the Vienna ab initio simulation package (VASP). [28] Using the geometry-optimized structures, three different magnetic models were designed (Figure 3.1b), and spin-polarized VASP calculations were performed to investigate their spin-exchange interactions. The structural parameters were further allowed to relax while the spin-polarized VASP calculations were performed. Table S3.5 summarizes the results of the VASP calculations. All three spin-polarized models were energetically much more stable than the NM model, indicating favoring of spin interactions in the system. Among the three spin-polarized models, FM and AFM1 were found to be significantly more stable than the AFM2 model, indicating that FM interaction of the spins within the individual chains is preferred. Interestingly, the FM and AFM1 models were energetically very close in energy (the FM model was more stable just by 3.86 meV/u.c.), which seemed somewhat surprising to us because until now in all calculations in the Ru-rich phases of this structure type, which were done mainly on Fe-based phases, AFM1 was calculated to be the most stable model. For example, the recent DFT calculations on $Zr_2FeRu_5B_2$ indicated that AFM1 is more stable than FM by 120 meV/u.c., while in $Ti_2FeRu_4RhB_2$, AFM1 is found to be more stable than FM by 61.1 meV/u.c.[29, 30] Furthermore, considering the 61 VEC for $Hf_2MnRu_5B_2$, it would favor dominating AFM interactions as mentioned earlier (VEC < 62). Certainly,

either Mn or Hf or both act as a rule-breaker in $Hf_2MnRu_5B_2$. Therefore, this unexpected prediction had to be verified experimentally (see later).

VASP results on the FM ground state show a large moment of 2.70 μ_B on Mn, which was mainly attributed to the splitting of the majority and minority spins of Mn d orbitals (Figure 3.2b). Also, very small moments were calculated on Ru atoms (Table S3.5).

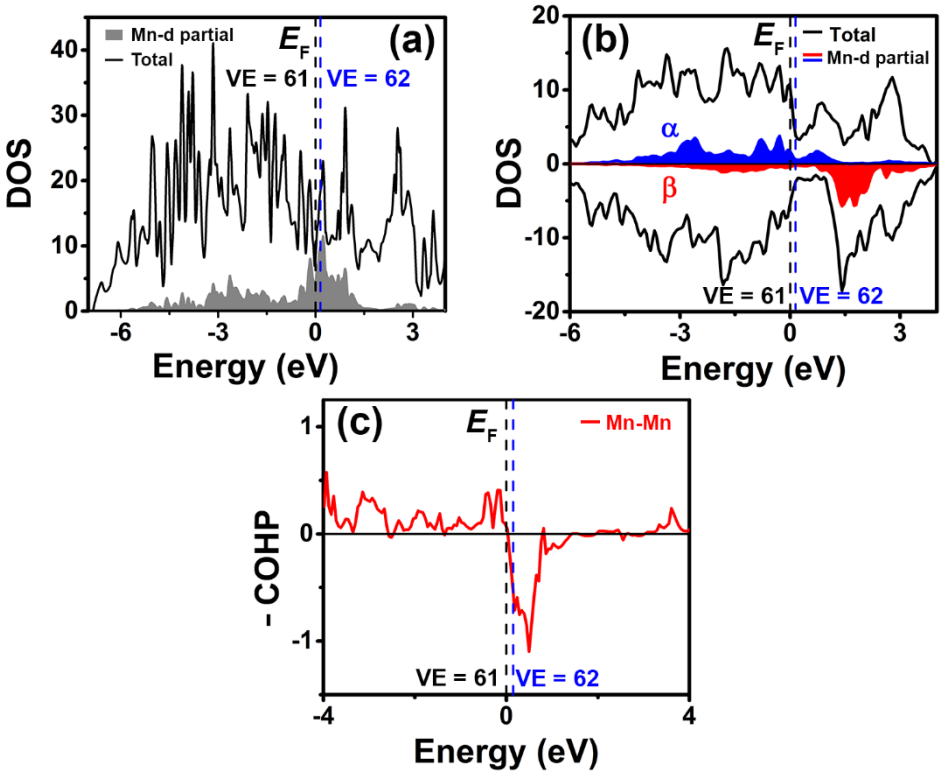

Figure 3.2. **(a)** Non-spin-polarized and **(b)** spin-polarized [majority (blue) and minority (red) spin states of Mn] density of state curves of $Hf_2MnRu_5B_2$ (VEC = 61). **(c)** Non-spin-polarized COHP curve for the Mn–Mn interaction. The Fermi level (E_F) is shown as a black dotted line (VEC = 61), while the blue dotted line represents the Fermi level for VEC = 62.

$Hf_2MnRu_5B_2$ was synthesized by arc-melting the elements under an argon atmosphere. Structure refinement and phase analysis of the powder X-ray data were done

by the *Rietveld* method, [31, 32] which yielded a mixed occupancy of Ru and Mn at the 2*a* Wyckoff position and a final composition of $Hf_2Mn_{0.73(1)}Ru_{5.27(1)}B_2$. A Fe/Ru mixed occupancy was also observed in the isostructural $Zr_2FeRu_5B_2$ and related systems.[29] The results of the *Rietveld* refinement are given in Tables S3.1–S3.3 and Figure S3.1. The main phase $Hf_2Mn_{0.73}Ru_{5.27}B_2$ was produced with 92 wt % along with minor known side phases identified as HfRu (4.6 wt %) and $Ru_{1-x}Mn_x$ (x = 0.40 and 3.4 wt %). The refined lattice parameters a = 9.3021(5) Å and c = 3.0549(2) Å are in good agreement with those optimized by DFT (Table S3.1). Experimental and structure determination details are provided in the Supporting Information.

Magnetization measurements were carried out in a vibrating-sample magnetometer in the field-cooled (FC) and zero-field-cooled (ZFC) modes and at different magnetic fields (Figure 3.3). At very low field (0.005 T), a maximum (T_N = 20 K) is apparent for both FC and ZFC measurements in the μ–T plot (Figure 3.3a), indicating AFM ordering. However, this AFM transition vanishes at high magnetic fields (Figures 3.3b and S3.4), and an FM state emerges with $T_C \sim 115$ K, indicating metamagnetic behavior for this compound. This behavior might be rationalized by the competition between the AFM1 and FM ground states and weak interchain Mn–Mn interactions, as found by DFT calculations. Our understanding is that the ground state is AFM with weak AFM interactions between the Mn chains. These weak interactions can be easily overcome by a small applied field. Indeed, at 0.1 T, an FM transition at $T_C \sim 115$ K appears in the μ–T plot, indicating metamagnetic behavior for this compound. Also, a *Curie–Weiss* behavior, $\chi_m = C/(T - \theta)$, was apparent above 275 K for the $1/\chi_m$–T plot, the fitting of which led to a positive *Weiss*

constant of 116.7 K, confirming the presence of FM interactions. The derived *Curie* constant (C) is 9.29 × 10–7 emu·K·mol^{-1}, which leads to an effective moment of 2.73 μ_B. This moment is very close to the DFT-calculated moment on Mn for the two favored FM and AFM1 magnetic models (Table S3.5).

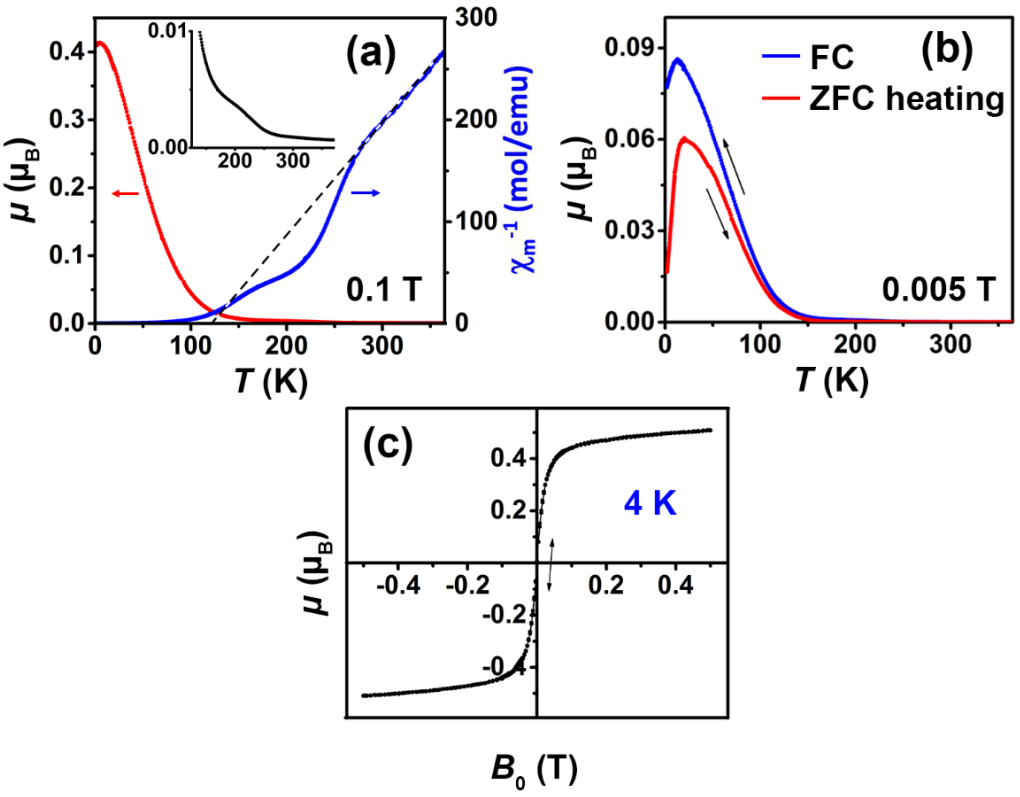

Figure 3.3. Magnetization versus temperature (μ–T) and inverse susceptibility versus temperature ($1/\chi_m$–T) plots for $Hf_2Mn_{0.73}Ru_{5.27}B_2$ at **(a)** 0.005 and **(b)** 0.1 T fields. **(c)** Magnetization versus field strength curve (hysteresis loop) measured at 4 K up to an applied field of 0.5 T.

The $1/\chi_m$–T plot at 0.1 T also indicates a deviation from the *Curie–Weiss* line between 150 and 275 K, also observed in the μ–T plot upon enlargement (inset in Figure 3b). This weak transition, which disappears at high magnetic fields (e.g., at 5 T; Figure S3.4b), is still unidentified but most probably arises from the metamagnetic nature of the

phase. Furthermore, to confirm that the magnetic transitions of $Hf_2MnRu_5B_2$ are not originating from the side phase $Ru_{1-x}Mn_x$, we have successfully synthesized and measured the magnetic property of this phase, which was found to be Pauli paramagnetic with a magnetic moment 3 orders of magnitude weaker than that of $Hf_2MnRu_5B_2$ at 0.05 T.

To further understand the nature of Mn–Mn interactions within the chains, crystal orbital Hamilton population (COHP) analysis was performed. In the non-spin-polarized Mn–Mn COHP (Figure 3.2c) of $Hf_2MnRu_5B_2$, the Fermi level (E_F) falls in a nonbonding region; thus, direct Mn–Mn interactions would be predicted to be AFM within the chains.[16] However, a large antibonding peak is found near E_F in the non-spin-polarized Mn–Mn COHP plot (from 0.0 to 1.0 eV; Figure 3.2c). Assuming a valid rigid band approximation, E_F would shift to slightly higher energies with increased VEC for the experimental composition ($Hf_2Mn_{0.73}Ru_{5.27}B_2$ has 61.3 VEC compared to 61 for $Hf_2MnRu_5B_2$) and fall into the antibonding region. Consequently, COHP would predict direct FM Mn–Mn interactions (E_F for VEC = 62 is shown in Figure 2). This analysis also confirms the weak nature of the AFM interactions, which in this case would be suppressed by an increase of the VEC (a slight change in the composition).

Field-dependent measurements (see Figure 3.3c) at low temperature (4 K) revealed a hysteretic behavior with extremely small coercivity; thus, the compound can be classified as an extremely soft magnetic material. Even though the ground state is AFM below 20 K, the presence of hysteresis at 4 K indicates that a canting of the magnetic spins is very probable. Furthermore, the magnetic moment per Mn atom obtained from the μ–H plot is

much smaller than the theoretically predicted value for an FM state, which also hints at a canted AFM ground state.

VASP spin-orbit coupling calculations indicated that spin parallel to the *c* axis is higher in energy than spin perpendicular to the *c* axis by 0.84 meV/u.c. (the energy difference for hard magnetic MnBi is 0.30 meV/u.c.), indicating large magnetic anisotropy. However, the interchain Mn–Mn spin-exchange interaction is very weak, making it very easy to flip the spins of each isolated FM Mn chain under an applied magnetic field, like the behavior of soft magnetic $Ti_2FeRh_5B_2$. [30] Therefore, this compound ends up having a very small coercivity despite its large magnetic anisotropy.

3.3 Conclusion

The VEC of this new compound is 61 (61.3 for the experimental composition), and thus it is surprising that FM interactions dominate in this compound, even if it is only at high magnetic fields. In fact, this behavior mostly occurred in VEC-richer compounds (VEC ≥ 63). For the Ru-rich (VEC-poorer) compounds, Fe has been the magnetically active element and mostly 3d or 4d transition metals have been used on the *A*-site [in $A_2M(TT')_5B_2$]. Consequently, Mn and the 5d element (Hf) should be mostly credited for this unexpected behavior in this VEC-poorer range.

3.4 Experimental Details

The starting materials used for the synthesis of the title phase were elemental powders of Hf (99.6%), Mn (99.99%), Ru (99.9%) and B (99% amorphous and crystalline), purchased from Alfa Aesar. The elements were weighed in the desired atomic ratio, mixed well (total

mass around 0.3 g) and was pressed into a pellet inside a glove box. The pellet was arc-melted under argon atmosphere using a Schlenk line. The argon gas was purified prior to use over silica gel, molecular sieves and titanium sponge (at 950 K). The melting was performed on a water-cooled copper crucible using a tungsten tip as the second electrode, where the pellet was re-melted for few seconds with a direct current of 20 Amperes until a homogeneous melting was achieved (prolonged melting will evaporate manganese). During the handling, sample preparation, manipulation, and synthesis tungsten carbide die sets, agate mortar-pestle were used in order to avoid any magnetic contaminations. The synthesized phase was stable in the air as a compact bulk as well as finely ground powders. Powder X-ray data of synthesized compound was collected at room temperature, using Rigaku MiniFlex 600 diffractometer [Cu-$K\alpha_1$ radiation (λ = 1.54059 Å), Ge monochromator, image plate detector, and silicon standard].

Energy-dispersive X-ray spectroscopy (EDX) was carried out on an ultra-high-resolution low-energy system of the type Nova NanoSEM450 equipped with a 50mm^2 X-Max 50 SD EDX detector.

The magnetic measurements of an approximately 20 mg sample of crystalline powder were measured by utilizing a Vibrating Sample Magnetometer in an EverCool-II cryogen-free upgraded version of a Physical Property Measurement System (Quantum Design International, USA). ZFC temperature dependencies were measured under fields of 0.005 and 0.1 T from 2 to 370 K after cooling in zero field. Field dependencies were measured between +0.5 and -0.5 T at various temperatures.

3.5 Computation Details

All VASP calculations employed the generalized gradient approximation (GGA) with exchange and correlation treated by the Perdew-Burke-Enzerhoff (PBE) functionals.[33] The convergence threshold for structural relaxation was set to be 0.02 eV/Å in force. The cutoff energy for the plane wave calculations was set to 500 eV and the Brillouin zone integrations were carried out using a 5 × 5 × 15 and 5 × 5 × 7 k-point mesh for crystallographic unit cells (NM, FM, and AFM1) and cells doubled along the c-axis (AFM2), respectively. GGA+SOC calculations were employed to examine the spin-orbit coupling effect. VASP total energies of spin parallel and perpendicular to the c-axis were calculated to examine the magnetic anisotropy.

Within TB-LMTO, exchange and correlation were treated using the von Barth-Hedin local density (LDA) and local spin-density approximation (LSDA). [34] All relativistic effects except spin-orbit coupling were taken into account using a scalar relativistic approximation.[35] The basis sets include 2s and 2p wave functions for B, 3d, 4s, 4p wave functions for Mn, 4d, 5s, 5p wave functions for Ru, 5d, 6s, 6p wave functions for Hf. The B 3d, Ru 4f, and Hf 5f orbitals were treated by the Löwdin downfolding technique.[36] Sets of 2 × 2 × 8 k-points in the irreducible wedge of the Brillouin zone were used for integrations over crystallographic unit cells.

3.6 Supporting Information

Table S3.1. *Rietveld* refinement data of $Hf_2Mn_{0.73}Ru_{5.27}B_2$.

Phase	$Hf_2MnRu_5B_2$	
Refined composition	$Hf_2Mn_{0.73(1)}Ru_{5.27(1)}B_2$	
Space group; *Z*	*P*4/*mbm* (no. 127), 2	
Profile function	pseudo-Voigt	
Lattice parameters	**expt.**	**calc.**
***a* (Å)**	9.3021(5)	9.27682
***c* (Å)**	3.0549(2)	3.06550
Volume (Å^3)	264.34	
R_P, R_{Bragg}	0.0309, 0.0470	
Mass fraction (w%)	92.0	
Side phase-1 HfRu, *Pm*-3*m* (no. 221) *a* =3.2113(4) R_P, R_{Bragg} =0.0244, 0.0298 mass fraction = 4.6 w%	**Side phase-2** $Ru_{1-x}Mn_x$ (x = 0.40), *P*6$_3$/*mmc* (no. 194) *a* =2.6724(9), *c*= 4.266(4) R_P, R_{Bragg} =0.0215, 0.0339 mass fraction = 3.4 w%	

Table S3.2. Atomic coordinates for $Hf_2Mn_{0.73}Ru_{5.27}B_2$ obtained from *Rietveld* refinement. The ones obtained from DFT calculations of FM $Hf_2MnRu_5B_2$ are shown in italics.

Atom	**Wyckoff position**	**Occupancy**	**x**	**y**	**z**
Hf1 (expt.)	*4g*	1.0	0.32417(14)	0.17583(14)	0
Hf1 (calc.)			*0.32367*	*0.17633*	*0*
Mn1/Ru3	*2a*	0.73/0.27	0	0	0
Ru1	*3.2c*	1	0	0.5	0.5
Ru2 (expt.)	*8j*	1	0.0709(2)	0.21512(19)	0.5
Ru2 (calc.)			*0.07010*	*0.21353*	*0.5*
B1 (expt.)	*4g*	1	0.122	0.378	0
B1 (calc.)			*0.12394*	*0.37606*	*0*

Table S3.3. Selected interatomic distances and coordination in $Hf_2Mn_{0.73}Ru_{5.27}B_2$ from *Rietveld* refinement.

Ru2	B1	2x	2.2033(13)
	Mn1|Ru3	2x	2.6024(14)
	Ru1	1x	2.7308(18)
	Ru2	1x	2.8149(26)
	Hf1	2x	2.8315(19)
	Hf1	2x	2.9376(19)
	Ru2	2x	2.9797(26)
	Ru2	2x	3.0549(2)
Ru1	B1	4x	2.2156(1)
	Ru2	4x	2.7308(18)
	Hf1	4x	2.7719(11)
	Ru1	2x	3.0549(2)
Hf1	B1	1x	2.6596(13)
	Ru1	2x	2.7719(11)
	B1	2x	2.8153(13)
	Ru2	4x	2.8315(19)
	Ru2	4x	2.9376(19)
	Hf1	2x	3.0549(2)
Mn1|Ru3	Ru2	8x	2.6024(14)
	Mn1|Ru3	2x	3.0549(2)
B1	Ru2	4x	2.2033(13)
	Ru1	2x	2.2156(1)
	Hf1	1x	2.6596(13)
	Hf1	2x	2.8153(13)

Table S3.4. Calculated interatomic distances and -ICOHP values for Hf_2MnRuB_2 compared to those with literature values.

Bond	**Distance (Å)**	**ICOHP (eV/bond)**	**Bond (Literature)**	**Distance (Å) (Literature)**	**ICOHP (eV/bond, Literature)**
Ru-B	2.235	2.60	Ru-B[29]	2.225[29]	2.93[29]
	2.207	2.81			
Ru-Hf	2.775	1.46	Ru-Zr[29]	2.851-2.947[29]	1.58-2.02[29]
	2.829	1.46			
	2.936	1.30			
Ru-Ru	2.736	1.26	Ru-Ru[16]	2.6-3.0[16]	0.851-1.09[16]
	2.839	1.02			
	2.948	1.00			
Ru-Mn	2.588	1.97	Ru-Mn[38]	2.75[38]	1.39[38]
Mn-Mn	3.066	0.57	Mn-Mn[39]	2.71[39]	0.63[39]

Table S3.5. VASP total energies and magnetic moments for different magnetic models.

Model	**Relative energy (meV/u.c.)**	**Magnetic moment (μ_B)**			
		Mn (2*a*)	**Ru (8*j*)**	**Ru (3.2c)**	**Total**
FM	0.00	+2.70	-0.10	-0.09	+2.19
AFM1	+3.86	±2.67	±0.05	0.00	0.00
AFM2	+66.1	±2.64	±0.01	0.00	0.00
NM	+1162.1	-	-	-	-

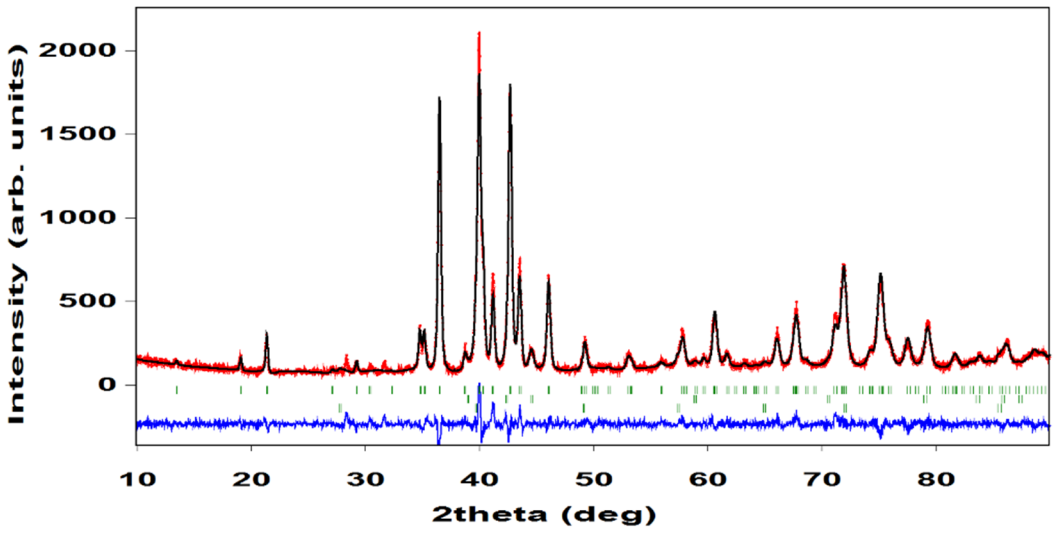

Figure S3.1. Measured (red) and calculated (black) powder patterns of $Hf_2Mn_{0.73}Ru_{5.27}B_2$, after *Rietveld* refinement of $Hf_2Mn_{0.73}Ru_{5.27}B_2$ sample. *Bragg* peak positions of the three identified phases (see table S3.1) given in green.

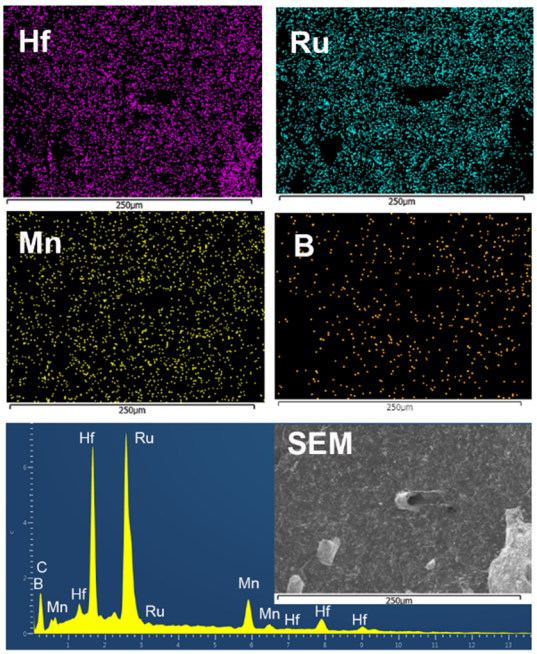

Figure S3.2. EDX mapping (top) and EDX spectrum (bottom) for the synthesized phase along with electron image from SEM (bottom inset). C in the EDX spectrum is from the carbon paste used as support.

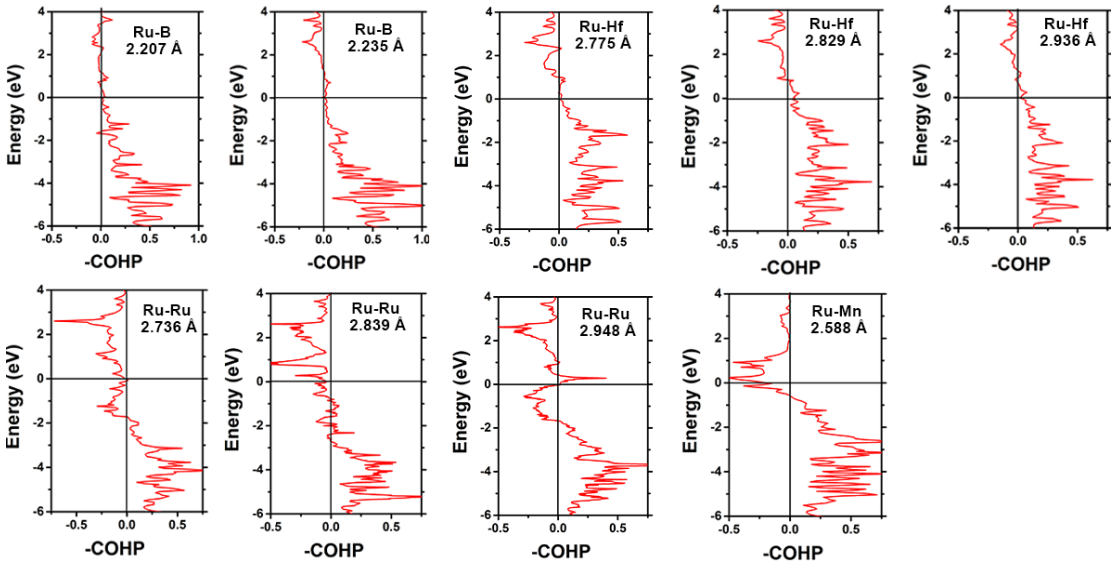

Figure S3.3. COHP curves for the different type of interactions in $Hf_2MnRu_5B_2$.

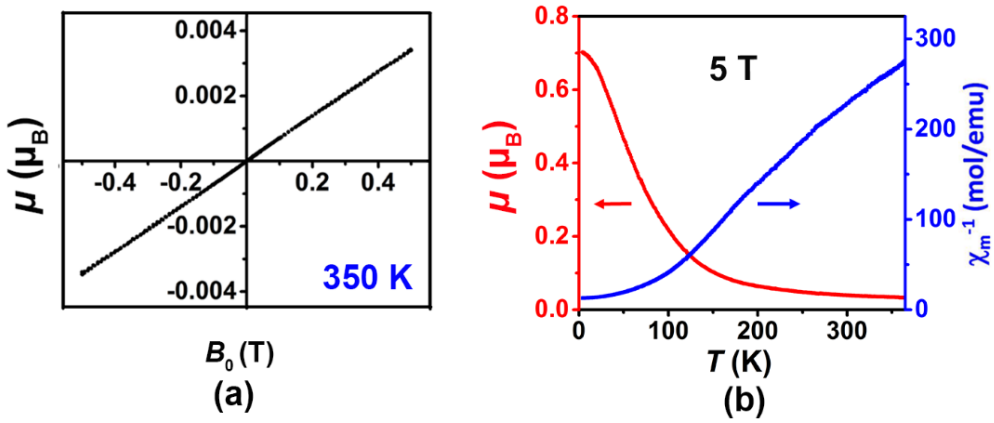

Figure S3.4. Magnetization vs field strength curve (hysteresis loop) measured at 350 K up to an applied magnetic field of 0.5 T for $Hf_2Mn_{0.73}Ru_{5.27}B_2$ (a), magnetization vs temperature and inverse susceptibility vs temperature plots for $Hf_2Mn_{0.73}Ru_{5.27}B_2$ at 5 T (b).

3.7 References

[1] F. J. DiSalvo, *Pure Appl. Chem.* 2000, *72*, 1799-1807.

[2] M. A. Jansen, *Angew. Chem. Int. Ed.* 2002, *41*, 3746-3766.

[3] M. G. Kanatzidis, K. R. Poeppelmeier, S. Bobev, A. M. Guloy, S.-J. Hwu, A Lachgar, S. E. Latturner, E. Schaak, D.-K. Seo, S. C. Sevov, *Prog. Solid State Chem.* 2008, 36, 1-133.

[4] O. M. Yaghi, M. O'keeffe, N. W. Ockwig, H. K. Chae, M. Eddaoudi, J. Kim, *Nature* 2003, *423*, 705-714.

[5] J. D. Bocarsly ,E. E. Levin, C. A. Garcia, K. Schwennicke, S. D. Wilson, R. Seshadri, *Chem. Mater.* 2017, *29*, 1613-1622.

[6] P. C. Canfield, *Nat. Phys.* 2008, *4*, 167-169.

[7] J. P. Scheifers, Y. Zhang, B. P. Fokwa, Accounts of chemical research, 2017, *50*, 2317-2325.

[8] H. Park, P. R. N. Misse, M. Mbarki, P. Shankhari, B. P. T. Fokwa, *Eur. J. Inorg. Chem.* 2017, *2017*, 2267-4472.

[9] P. Shankhari, P. R. N. Misse, M. Mbarki, H. Park, B. P. T. Fokwa, *Inorg. Chem.*, 2017, *56,* 446–451.

[10] M. Mbarki, R. S. Touzani, B. P. T. Fokwa, *Angew. Chem. Int. Ed.* 2014, *53*, 13174-13177.

[11] K. Hofmann, N. Kalyon, C. Kapfenberger, L. Lamontagne, S. Zarrini, R. Berger, R. Seshadri, B. Albert, *Inorg. Chem.* 2015, *54*, 10873-10877.

[12] Q. Zheng, R. Gumeniuk, H. Borrmann, W. Schnelle, A. A. Tsirlin, H. Rosner, U. Burkhardt, M. Reissner, Y. Grin, *Dalton Trans.* 2016, *45*, 9590-9600.

[13] Y. B. Kuz'ma, Y. P. Yarmolyuk, *J. Struct. Chem.* 1971, *12*, 422-424.

[14] B. P. T. Fokwa, *Eur. J. Inorg. Chem.* 2010, *2010*, 3075-3092.

[15] E. Nagelschmitz, W. Jung, *Chem. Mater.* 1998, *10*, 3189-3195.

[16] R. Dronskowski, K. Korczak, H. Lueken, W Jung, *Angew. Chem. Int. Ed.* 2002, *41*, 2528-2532.

[17] B. P. T. Fokwa, H, Lueken, R. Dronskowski, *Chem. Eur. J.* 2007, *13*, 6040-6046.

[18] G. D. Samolyuk, B. P. T. Fokwa, R Dronskowski, G. J. Miller, *Phys. Rev. B.* 2007, *76*, 094404 (1-12).

[19] B. P. T. Fokwa, H Lueken, H. R. Dronskowski, *Eur. J. Inorg. Chem.* 2011, 2011, 3926-3930.

[20] M. Hermus, B. P. T. Fokwa, *Z. Anorg. Allg. Chem.* 2011, *637*, 947-954.

[21] M. Hermus, M. Yang, D. Grüner, F. J. DiSalvo, B. P. T. Fokwa, *Chem. Mater.* 2014, *26*, 1967-1974.

[22] V. Ly, X. Wu, L. Smillie, T. Shoji, A. Kato, A. Manabe, K. Suzuki, *J. Alloys Compd.* 2014, *615*, S285-S290.

[23] S.-H. Kim, M. Boström, D.-K. Seo, *J. Am. Chem. Soc.* 2008, *130*, 1384-1391.

[24] S. Ma, K. Bao, Q. Tao, P. Zhu, T. Ma, B. Liu, Y. Liu, T. Cui, *Sci. Rep.* 2017, 7.

[25] M. Hermus, B. Fokwa, *Eur. J. Inorg. Chem.* 2014, *2014*, 3085-3094.

[26] P. E. Blöchl, *Phys. Rev. B* 1994, *50*, 17953-17979.

[27] G. Kresse, D. Joubert, *Phys. Rev. B* 1999, *59*, 1758-1775.

[28] G. Kresse, J. Furthmüller, *Phys. Rev. B* 1996, *54*, 11169-11186.

[29] J. Brgoch, S. Yeninas, R. Prozorov, G. J. Miller, *J. Solid State Chem.* 2010, *183*, 2917-2924.

[30] Y. Zhang, G. J. Miller, B. P. T. Fokwa, *Chem. Mater.* 2017, 29, 2535-2541.

[31] D. S. Young, B. S. Sachais, L. C. Jefferies, The *Rietveld* method, 1993.

[32] J. Rodriguez-Carvajal, *In satellite meeting on powder diffraction of the XV congress of the IUCr*, 1990, *127,* Toulouse, France.

[33] J. P. Perdew, K. Burke, M. Ernzerhof, *Phys. Rev. Lett.* 1996, *77*, 3865-3868.

[34] U. Barth, Von; L. A. Hedin, *J. Phys. C* 1972, *5*, 1629-1642.

[35] D. D. Koelling, B. N. Harmon*, J. Phys. C* 1977, *10*, 3107-3114.

[36] W. R. L. Lambrecht, O. K. Andersen, *Phys. Rev. B* 1986, *34*, 2439-2449.

[37] R. Dronskowski, K. Korczak, H. Lueken, W Jung, *Angew. Chem. Int. Ed.* 2002, *41*, 2528-2532.

[38] B. P. T. Fokwa, C. Goerens, M. Gilleßen, *Z. Kristallogr.* 2010, *225*, 180-186.

[39] I. M. Ndassa, B. P. T. Fokwa, *Comput. Mater. Sci.* 2014, *92*, 416-421.

Chapter 4

A Delicate Balance Between Antiferromagnetism and Ferromagnetism in Ruthenium-Rich $Ti_3Co_5B_2$-Type Borides: A DFT and Experimental Study

4.1 Introduction

Metal borides readily distinguish themselves in the realm of solid-state materials by a set of characteristic properties, including high melting points, superior mechanical hardness, and chemical inertness originating from the presence of strong boron-boron and metal-boron bonds.[1 – 9] Besides these, some metal borides show superconductivity, such as MgB_2 [10] (first high-temperature metallic superconductor) and the recently discovered NbRuB, [11] TaRuB, or NbOsB [12], while few others show superior stability against radiations and are used as monochromators, for example, YB_{66}.[13] Unexpected and very effective magnetic refrigeration materials based on the $AlFe_2B_2$ were explored recently. [14 – 16] Also, high temperature boron-based thermoelectric materials have been studied extensively in recent years.[17] Moreover, many metal-borides are known to show extraordinary magnetic properties when containing magnetically active elements in their compositions, for example, the rare-earth-based strong permanent magnet $Nd_2Fe_{14}B$ and its derivatives.[18,19] The compound $Nd_2Fe_{14}B$ is widely recognized as "neodymium magnet" and plays a crucial role in our daily-used electronic devices including speakers and electric motors. The presence of rare-earth elements along with magnetically active element is responsible for very large coercivity values and high energy products in these "hard" magnetic materials.[19] Rare-earth-free borides containing magnetically active elements, on the other hand, such as the ordered quaternary variants of the $Ti_3Co_5B_2$

structure type [20a-b, 21] are known to exhibit a wide range of comparatively "soft" itinerant magnetic properties. Such itinerant magnetism, which stems from the synergy between magnetically active elements and conduction electrons offers potential applications in magnetic refrigeration and spintronics.[14-17, 22]

The tetragonal $Ti_3Co_5B_2$ (space group *P*4/*mbm*, no. 127) is a prolific structure type within the metal-rich boride family adopted by more than seventy known compounds which include ternaries (with general composition: $A_3T_5B_2$), quaternaries ($A_2MT_5B_2$) and quinaries [$A_2M(TT')_5B_2$].[23-25] The crystal structure of the ternary variants is formed by face-connected trigonal, tetragonal and pentagonal prisms of *T*-atoms (electron-rich transition metals such as Co, Rh, Ir, Ru). The *A*-atoms (larger transition or main group elements such as Mg, Sc, Ti, Zr, Hf, Mn) reside inside the tetragonal and pentagonal prisms whereas the smaller boron atoms are located within the trigonal prisms (Figure 4.1).[25] Of much interest are the above-mentioned quaternary variants containing magnetically active elements (*M* = Fe, Mn, Co, etc.) which form well-separated chains of *M*-atoms along [001] within the channels built by tetragonal prisms. The intrachain *M*-*M* distance of ca. 3.1 Å is suitable for direct magnetic interaction observed in many compounds of this type, for example, antiferromagnetic $Sc_2FeRu_5B_2$, ferromagnetic $Sc_2FeRh_5B_2$ or metamagnetic $Sc_2FeIr_5B_2$.[26-28] Interestingly, the transition from antiferromagnetism to ferromagnetism between the first two compounds was explained by a valence electron (VE) dependent study in the series $Sc_2FeRu_{5-x}Rh_xB_2$ (x = 0 – 5, VE = 60 – 65) [28]. In this series, increasing the number of VE first resulted in decreased antiferromagnetic interactions from 60 to 62 VE, then a transition from antiferro- to ferromagnetism was observed between 62 and 63

VE. Adding more valence electrons (63 – 65 VE) further enhanced the ferromagnetic interactions. Non-spin-polarized Crystal Orbital Hamilton Population (COHP) analysis established that phases with ≤ 62 VE (for example, $Sc_2FeRu_5B_2$, 60 VE) exhibit nonbonding *M-M* states at the Fermi level (E_F), therefore showing antiferromagnetic interactions, whereas phases with higher VE such as for ≥ 63 VE (for example, $Sc_2FeRh_5B_2$, 65 VE) the E_F show antibonding *M-M* states at the Fermi suggesting ferromagnetic interactions. [26, 29]

Much to our surprise, we recently discovered stable ferromagnetic interactions in a ruthenium-rich boride $Hf_2MnRu_5B_2$ with 61 VE.[30] DFT calculations using the Vienna Ab initio simulation package (VASP) found that the most stable ground state in this compound was ferromagnetic (FM) where chains of Mn-atoms interact ferromagnetically with similar neighboring chains (illustrated in Figure 4.3). However, this FM ground state model was found to be close in energy to one of the antiferromagnetic (AFM) models AFM1 where neighboring chains interact antiferromagnetically with each other.[30] This small energy difference between the FM and AFM1 (3.9 meV/unit-cell) pointed to a more complex magnetic behavior. Experimentally, AFM ordering (T_N = 20 K) was observed in $Hf_2MnRu_5B_2$ at very low magnetic fields (≤ 0.005 T), while FM behavior with $T_C \approx 115$ K and a positive *Weiss* constant of 116.7 K were found at higher fields, for example, 0.1 T field. This discovery was intriguing because for all prior studies on Ru-rich compounds in this structure type were mostly focused on Fe-based phases, and DFT had predicted stable AFM1-type ground states for VE ≤ 62. For example, in $Zr_2FeRu_5B_2$ (62 VE), AFM1 model was found more stable than the FM model by 120 meV/u.c. [31] In fact, ferromagnetism in

ruthenium-rich borides, in general, is rare. Only some rare-earth-based ruthenium-rich borides[32] with the $CeCo_3B_2$ structure type and a few rare-earth-free ruthenium-rich borides such as $Ti_{9-n}Fe_{2+n}Ru_{18}B_8$ (n = 0, 1, 2) [33, 34] crystallizing in the $Zn_{11}Rh_{18}B_8$ structure type [35] are ferromagnetic. Discovery of $Hf_2MnRu_5B_2$ positioned $Ti_3Co_5B_2$ as another structure type to show some ferromagnetic behavior (even if only field dependent) in the ruthenium-rich boride family. It was postulated that Mn was helping in stabilizing FM interactions between Mn chains in $Hf_2MnRu_5B_2$ in contrast to the Fe-based compounds (such as $Sc_2FeRu_5B_2$ or $Zr_2FeRu_5B_2$). However, a 5*d* element (Hf) was also used for the first time in this structure type which could have additional effects on itinerant magnetism and might have influenced magnetic interactions due to its 5*d* electrons; therefore, the effects of Mn and Hf needed to be evaluated independently, which was the primary motivation for this work.

In the present work, we have studied the series $A_2MRu_5B_2$ (*A* = Zr, Hf, *M* = Fe, Mn) theoretically (VASP total energy calculations and COHP bonding analysis) and experimentally. For a full experimental evaluation of the series, we have successfully synthesized and fully characterized the two new compounds $Hf_2FeRu_5B_2$ and $Zr_2MnRu_5B_2$. In addition, we have re-synthesized and carried out low-field magnetic measurements of the previously reported $Zr_2FeRu_5B_2$, which was studied only at high fields. [31]

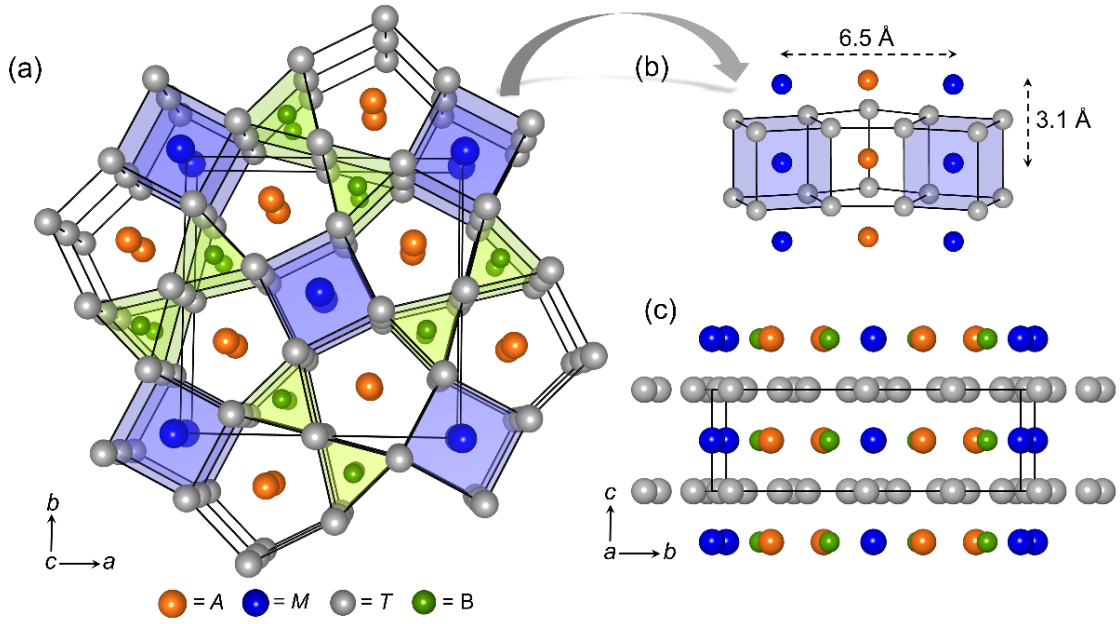

Figure 4.1. Perspective view of the crystal structure of the quaternaries $A_2MT_5B_2$ (A = Zr/Hf, M = Mn/Fe, T = Ru) viewed along [001] **(a)** and [100] **(b, c)** . The ternaries ($A_3T_5B_2$) can be visualized the same way but with $M = A$.

4.2 Theoretical results and discussion

Single-crystal X-ray diffraction data of the ternaries $Zr_3Ru_5B_2$ and $Hf_3Ru_5B_2$ [36] were used to make the new quaternary models $Zr_2MnRu_5B_2$ and $Hf_2FeRu_5B_2$ by replacing Zr and Hf at the *Wyckoff* position *2a* (within the tetragonal prisms) by Mn and Fe, respectively. This was done in agreement with previously reported quaternaries (e.g., $Zr_2FeRu_5B_2$) where *M* atoms had shown a strong site preference for the *2a Wyckoff* position. [31] Thus, the Fe or Mn-atoms form linear chains within the channels made by tetragonal prisms (Figure 4.1). The lattice parameters of the new quaternaries were relaxed using the projector augmented wave method of Blöchl [37-39] coded in the VASP.[40a] The relaxed structures were used to investigate the electronic structure and bonding, and magnetic interactions. More details on the theoretical procedure are provided under the experimental section.

4.2.1 Electronic stabilities of $Zr_2MnRu_5B_2$ and $Hf_2FeRu_5B_2$

The density of states (DOS) plots obtained from the electronic structure calculations are given in Figure 4.2. The Fermi levels (E_F) of the non-spin-polarized (nsp) DOS of the ternaries $Zr_3Ru_5B_2$ and $Hf_3Ru_5B_2$ [36] (recalculated in this work) fall in a large pseudogap (~ -0.5 – 2.0 eV, Figures 4.2a and 4.2b). This pseudogap, which indicates electronic stability, is a typical feature of $Ti_3Co_5B_2$-type compounds. [25] The nsp DOS calculations of the quaternaries $Zr_2MnRu_5B_2$ and $Hf_2FeRu_5B_2$, however, showed increased states at E_F indicating structural instability (Figures 4.2c and 4.2d). A partial DOS analysis of the atoms at the *2a Wyckoff* site for the ternaries and quaternaries (Figures 4.2a – 4.2d, dotted lines) reveal no states at E_F for Zr/Hf in the ternaries (Figures 4.2a and 4.2b) in contrast to the large states for Mn/Fe in the quaternaries (Figures 4.2c and 4.2d), thus explaining the electronic instabilities (increased DOS at E_F) in the quaternaries. However, these Mn/Fe states nearly all vanish when spin-polarization (sp) is taken into account (Figures 4.2e – 4.2f, dotted lines). Consequently, the sp DOS plots for both quaternaries show a significant decrease in the number of states at E_F compared to the nsp DOS plots—an indication of overall electronic stabilization through spin-polarization for both $Zr_2MnRu_5B_2$ and $Hf_2FeRu_5B_2$.

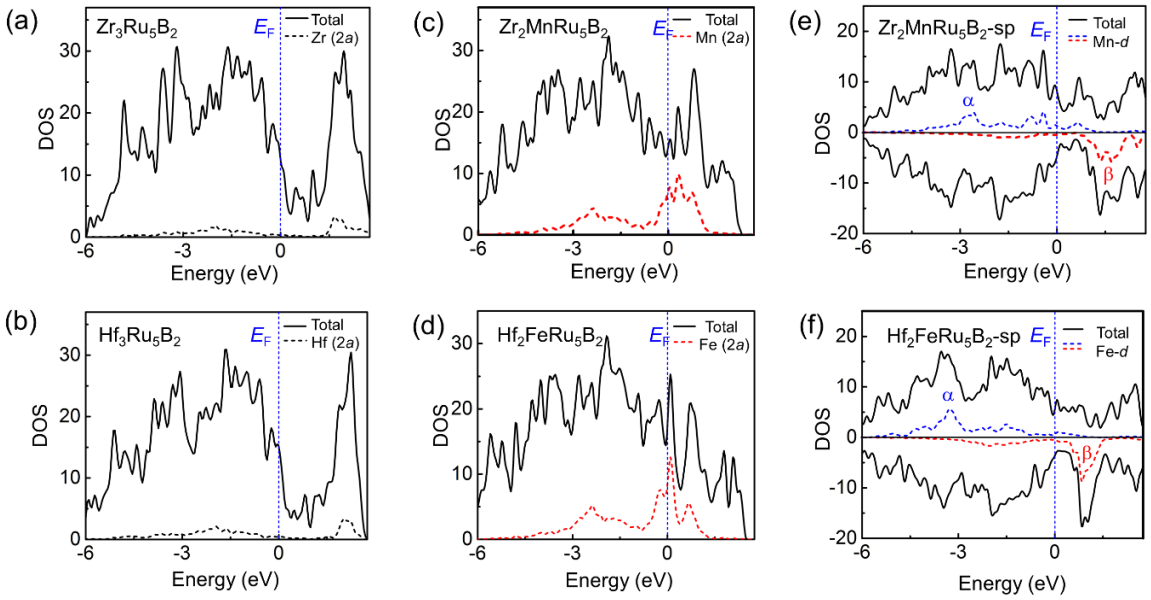

Figure 4.2. Non-spin-polarized total DOS plots for $Zr_3Ru_5B_2$ **(a)** and $Hf_3Ru_5B_2$ **(b)** with Zr/Hf (2*a* site) partial DOS are shown in black dotted lines; non-spin-polarized total DOS of $Zr_2MnRu_5B_2$ **(c)** and $Hf_2FeRu_5B_2$ **(d)** including Mn/Fe-d (2*a* site) partial DOS (red dotted lines); spin-polarized total DOS of $Zr_2MnRu_5B_2$ **(e)** and $Hf_2FeRu_5B_2$ **(f)** with partial sp DOS of Mn/Fe-d (red and blue dotted lines).

4.2.2 VASP total energy calculations and magnetic ordering models

To investigate the nature of spin-exchange interactions between the *M*-atoms, we considered four different magnetic models illustrated in Figure 4.3: one ferromagnetic (FM) and three antiferromagnetic (AFM1, AFM2, and AFM3), and calculated their total energies using spin-polarized VASP calculations. Both FM and AFM1 models have ferromagnetic chains in which atomic magnetic moments interact ferromagnetically within the chains, while AFM2 and AFM3 models have antiferromagnetic chains where atomic moments interact antiferromagnetically within the chains. However, in the FM and AFM2 models, the neighboring chains interact ferromagnetically (in the *ab* plane) whereas in AFM1 and AFM3 neighboring chains interact antiferromagnetically. The structural

parameters of these models were further relaxed while performing all the sp VASP calculations. The relative energies, with respect to the most stable model, of all four quaternaries are given in Table 4.1. Previously reported calculations of $Zr_2FeRu_5B_2$ were performed using the TB-LMTO [40b] method which also predicted the same AFM1 ground state as our VASP calculations (see later), however, for direct comparison with the other three compounds, we have recalculated the energies of this compound using the same VASP code.

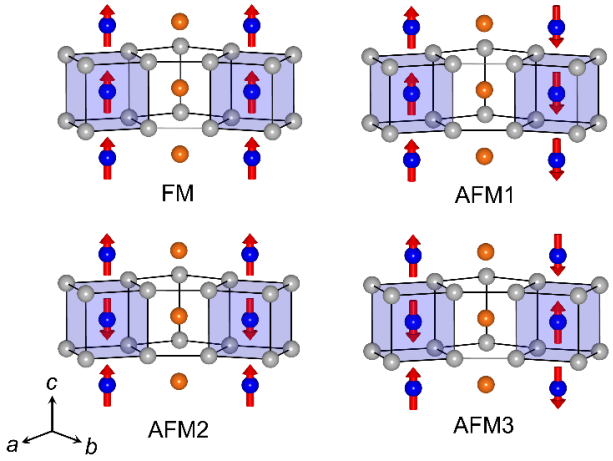

Figure 4.3. Magnetic models used for VASP calculations of $A_2MT_5B_2$ quaternaries showing possible interactions within and between the chains.

Table 4.1. Relative energies of different magnetic models for $A_2MT_5B_2$ (A = Zr, Hf, M = Fe, Mn) compared to the most stable one obtained through VASP calculations. The most stable model is given in boldface.

Compound	Relative energy compared to the most stable model (meV/u.c.)				
	FM	AFM1	AFM2	AFM3	NM
$Zr_2FeRu_5B_2$*	+89.0	**0.0**	88.5	92.7	1547.5
$Hf_2FeRu_5B_2$	+76.6	**0.0**	+76.8	85.4	1623.2
$Zr_2MnRu_5B_2$	+4.8	**0.0**	+99.9	132.4	1164.7
$Hf_2MnRu_5B_2$ [30]	**0.0**	+3.9	+66.1	91.98*	1160.2

*Recalculated in this work

The magnetic (sp) models for all the compounds were much stable (by more than 1000 meV/u.c.) than the nonmagnetic (NM) models indicating spin-polarization is highly favored and magnetic ordering is very likely. Interestingly, the experimentally observed lattice parameters match better with the ones that were obtained through the sp VASP calculations than the ones obtained through nsp calculations (Table 4.2)— additional evidence supporting magnetic ordering.

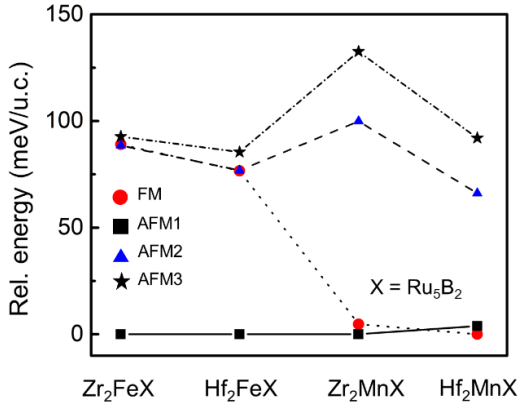

Figure 4.4. Relative energies for $A_2MT_5B_2$ (A = Zr, Hf, M = Fe, Mn) compared to the most stable model.

The relative energies of the different models from Table 4.1 are plotted in Figure 4.4. Out of the four models, AFM2 and AFM3, which have antiferromagnetic chains are much higher in energy than the ground state (most stable) model in all four cases. Besides, COHP analysis (see later) and previous findings [41] indicated that magnetic interaction within the chains would be ferromagnetic. Thus, these two least favored models with AFM intrachain interactions are eliminated at this point from further discussion. However, the similarity in the trends of these two models for all four compounds is noteworthy (Figure 4.4).

Table 4.2. Comparison of theoretically and experimentally obtained lattice parameters

	$Hf_2FeRu_5B_2$		$Zr_2MnRu_5B_2$		$Zr_2FeRu_5B_2$		$Hf_2MnRu_5B_2$	
	a (Å)	*c* (Å)	*a* (Å)	*c* (Å)	*a* (Å)	*c* (Å)	*a* (Å)	*c* (Å)
nsp relaxed	9.275	3.028	9.343	3.027	9.325	3.035	9.294	3.021
sp relaxed	9.264	3.061	9.318	3.076	9.311	3.076	9.276	3.065
Expt.*	9.307(1)	3.059(1)	9.322(1)	3.068(1)	9.318(1)	3.064(1)	9.302(1)	3.055(1)

nsp-relaxed = non-spin-polarized calculation while allowing geometry optimization
sp-relaxed = spin-polarized calculation while allowing geometry optimization (for the most stable model)
*obtained from the powder-XRD refinement

$Zr_2FeRu_5B_2$ and $Hf_2FeRu_5B_2$: In the reported LMTO results on $Zr_2FeRu_5B_2$, [29] AFM1 was found to be the most stable model suggesting that strong antiferromagnetic interactions were present between the chains. Our VASP calculations also confirm this result, but with a smaller energy difference (ΔE = 89.0 meV/u.c.) between AFM1 and FM compared to the LMTO result (ΔE = 120 meV/u.c.). In the new $Hf_2FeRu_5B_2$, AFM1 was also found to be the most stable model through VASP calculations. The large energy difference in favor of AFM1 indicates the presence of significant interchain antiferromagnetic interactions. However, the energy difference between AFM1 and FM observed in $Zr_2FeRu_5B_2$ is lowered by 12.4 meV/u.c. in $Hf_2FeRu_5B_2$ (ΔE = 76.6 meV/u.c.) indicating that Hf slightly helped to lower the AFM interchain interactions in this compound.

$Zr_2MnRu_5B_2$ and $Hf_2MnRu_5B_2$: Upon going from the Fe-based compounds to the Mn-based ones (compare in Figure 4.4), the large energy difference between the FM and AFM1 falls, and FM becomes comparable in stability to AFM1 (ΔE = 4.8 meV/u.c.) in $Zr_2MnRu_5B_2$. A further lowering in the energy of the FM leads to a slightly stable FM state for $Hf_2MnRu_5B_2$, albeit with a smaller energy difference (ΔE = -3.9 meV/u.c.). [30] In this case too, Hf strengthens the FM interchain interactions and even lead to a slightly more

stable FM model. These results indicate that the interchain FM and AFM Mn-Mn interactions in the Mn-based compounds are similar in strength in contrast to dominating AFM interactions in the Fe-based compounds.

In conclusion of these sp VASP calculations, the Mn-based phases prefer competing models while the Fe-based phases clearly favor AFM1, but in all phases, the intrachain interactions are FM, a finding also supported by the COHP bonding analysis below.

4.2.3 Understanding intrachain *M-M* magnetic interactions through COHP analysis

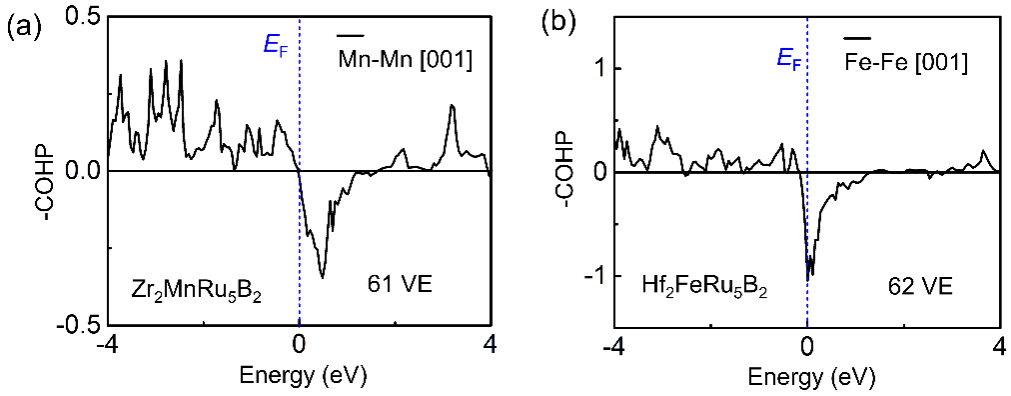

Figure 4.5. Non-spin-polarized COHP plots for *M-M* interaction along [001] for $Zr_2MnRu_5B_2$ **(a)** and $Hf_2FeRu_5B_2$ **(b)**.

The VASP results indicated preferred magnetic models with FM intrachain *M-M* interactions (AFM1 or FM) in all four systems. To further understand the nature of the intrachain interactions, we performed a COHP analysis of the nsp models using TB-LMTO method.[40b] The *M-M* interaction along [001] in such quaternaries have been described to be ferromagnetic if the Fermi level has antibonding states in the nsp COHP curve and antiferromagnetic if the Fermi has non-bonding states.[29] The nsp COHP curves of both

$Zr_2MnRu_5B_2$ and $Hf_2FeRu_5B_2$, given in Figure 4.5, show a large antibonding region starting near E_F. E_F for $Zr_2MnRu_5B_2$ (61 VE) falls just at the edge of the antibonding region, whereas E_F of $Hf_2FeRu_5B_2$ (62 VE) falls into the deep antibonding region given the fact that the later has one more electron. Thus, COHP would predict the *M-M* interactions to be ferromagnetic along the chains for both $Zr_2MnRu_5B_2$ and $Hf_2FeRu_5B_2$ supporting the VASP results (FM or AFM1 model), but in strong contrast to the previous finding for $Mg_2MnRh_5B_2$ (62 VE), for which COHP showed non-bonding interactions at E_F and experiments also found dominating AFM interactions (negative Weiss constant).[29] E_F in $Zr_2MnRu_5B_2$ closely lies to the non-bonding region, so one can expect in this case that the Mn-Mn ferromagnetic interaction along the chain may be weaker (this was also the case for $Hf_2MnRu_5B_2$ [30]) than the Fe-Fe ferromagnetic interactions in $Hf_2FeRu_5B_2$. Interestingly, this position of E_F (near the edge of the antibonding region) in these compounds offers an opportunity to predict new compounds containing intrachain ferromagnetic interactions. Adding more valence electrons for example via Ru/Ir or Ru/Rh substitution (without changing the magnetic element) will shift E_F towards the deep antibonding region, thus enabling robust ferromagnetic intrachain *M-M* interactions in a wide VE-range. Such studies are in progress and are reminiscent of recent studies achieved in the series $Sc_2FeRu_{5-x}Rh_xB_2$ (x = 0−5, VE = 60−65),[28] $Ti_2FeRu_{5-x}Rh_xB_2$ (x = 1−5, VE = 63−67),[42] and $Sc_2FeRu_{5-x}Ir_xB_2$ (x = 0−5, VE = 60−65), [43] where increasing ferromagnetic interactions with increasing VE have been observed. However, studying new Zr- or Hf-based quinary series will help shed some light on the role of the non-magnetic 4d and 5d transition metals replacing their 3d counterparts Sc and Ti.

4.3 Experimental results and discussion

4.3.1 Phase analysis and structure determination

The phase analysis of the new compounds was done by *Rietveld* refinement [44] of the powder X-ray diffraction (XRD) data using the *FullProf* [45] suite, results which are given in Table 4.3. All peaks in the powder X-ray diffraction pattern of $Zr_2MnRu_5B_2$ (Figure 4.6a) could be assigned to the $Ti_3Co_5B_2$ structure type (space group *P*4/*mbm,* no. 127) with lattice parameters of a = 9.322 (1) Å and c = 3.0679 (4) Å. Thus, no side phase was formed and $Zr_2MnRu_5B_2$ was obtained in a single phase. Mixed occupancy refinement at *Wyckoff* site 2*a* in agreement with single-crystal structure refinements (see later) led to the final composition $Zr_2Mn_{0.91(1)}Ru_{5.09(1)}B_2$ with a mixed occupancy of Mn and Ru on the 2*a* site. $Zr_2FeRu_5B_2$, [31] $Hf_2MnRu_5B_2$ [30] and many other reported quaternaries in this structure type show a similar mixed occupancy at the *2a* position.

$Hf_2FeRu_5B_2$ was obtained as the major product (94.8 wt %) along with the minor non-magnetic side product HfRu (5.2 wt %) identified through *Rietveld* refinement of powder XRD data (Figure 4.6b). Mixed occupancy refinement led to a Fe/Ru mixed *2a* site and a final composition of $Hf_2Fe_{0.81(1)}Ru_{5.19(1)}B_2$ with lattice parameters a = 9.307 (4) Å, c = 3.059 (1) Å. The refined lattice parameters of the two quaternary compounds were smaller than their parent ternaries $Hf_{2.83(2)}Ru_{5.17(2)}B_2$ [a = 9.4389 (3) Å, c = 3.1030 (2) Å] and $Zr_{2.86(5)}Ru_{5.12(5)}B_2$ [a = 9.4761 (3) Å, c = 3.1197 (2) Å] because the larger Zr or Hf atoms are replaced by the smaller Mn or Fe atoms.

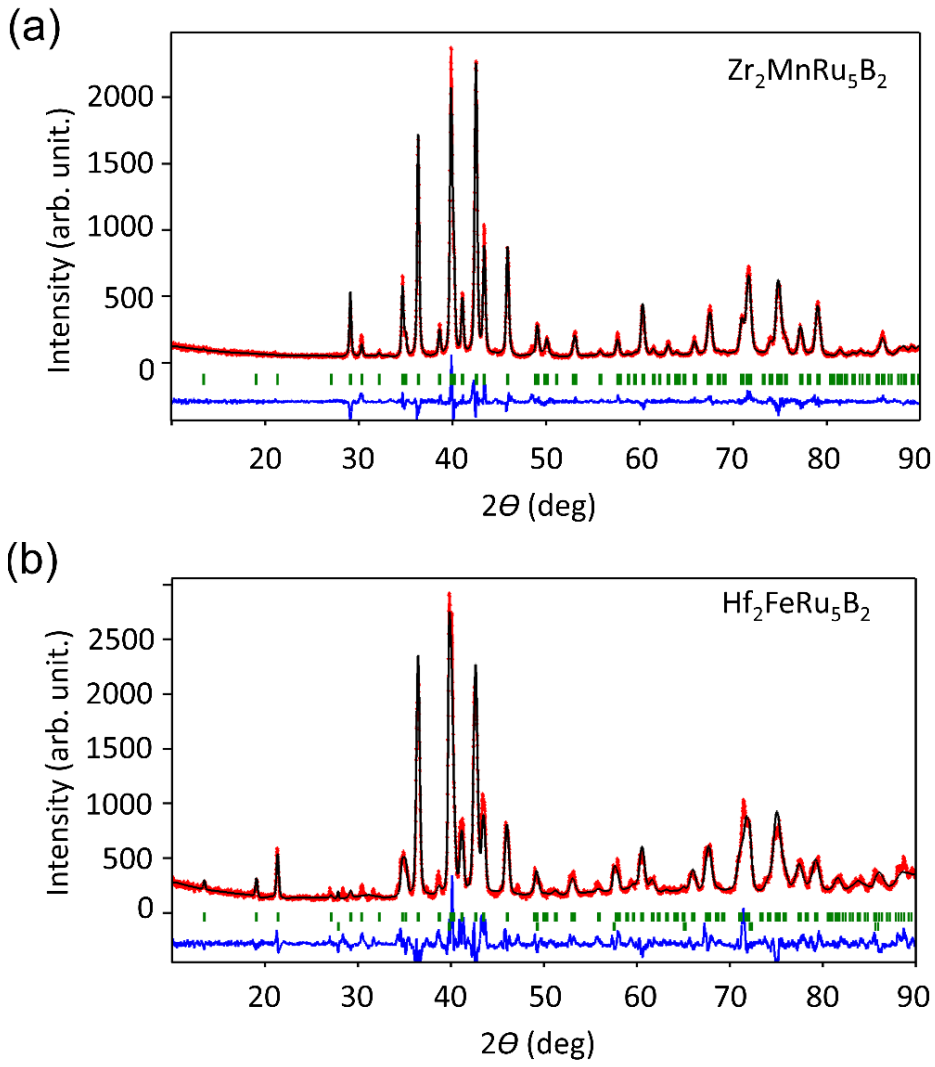

Figure 4.6. *Rietveld* refinement of the powder XRD data for the $Zr_2MnRu_5B_2$ (a) and $Hf_2FeRu_5B_2$ (b) samples. The red and the black curves represent the measured and the calculated patterns, respectively, whereas the blue curve shows the intensity difference. The positions of the *Bragg* peaks are shown in green.

Suitable single crystals obtained from each of the crushed samples of arc-melted $Zr_2MnRu_5B_2$ and $Hf_2FeRu_5B_2$ were found and XRD data were collected for single-crystal structure determination. The structures were solved by the direct method and refined using the SHELX programs.[46, 47] Results of the single-crystal refinements (given in Table 4.4) confirmed tetragonal $Ti_3Co_5B_2$-type structure with lattice parameters of a = 9.3448 (7)

Å and c = 3.0728 (4) Å for $Zr_2MnRu_5B_2$ and a = 9.2705 (4) Å and c = 3.0489 (2) Å for $Hf_2FeRu_5B_2$. The lattice parameters obtained through single-crystal refinements were very close to those obtained from the powder XRD (compare Table 4.3 and Table 4.4). Ruthenium atoms at *Wyckoff* position 8*j* and 2*c* in both $Zr_2MnRu_5B_2$ and $Hf_2FeRu_5B_2$ build face connected trigonal, tetragonal, and pentagonal prisms (see Figure 4.1). Zr/Hf, the largest atoms in the structure are located inside the pentagonal prisms (site 4*g*) while the boron atoms sit within the trigonal prisms (site 4*g*). Mn or Fe atoms are located inside the tetragonal prisms at the site 2*a*. However, this 2*a* site also partially accommodates Ru: About 5% of the Mn site in $Zr_2MnRu_5B_2$ and 19% of the Fe site in $Hf_2FeRu_5B_2$ are occupied by Ru atom. In this structure type, the 2*a* site is known to have mixed occupancy in many phases including the parent ternaries $Zr_{2.86(5)}Ru_{5.14(5)}B_2$ and $Hf_{2.83(2)}Ru_{5.17(2)}B_2$ where the 2*a* site was co-occupied by Ru and Zr/Hf atoms while in $Zr_2FeRu_5B_2$ the *2a* site was mix-occupied by Fe and Ru. The structure refinements converged with final compositions of $Zr_2Mn_{0.95(1)}Ru_{5.05(1)}B_2$ and $Hf_2Fe_{0.81(2)}Ru_{5.19(2)}B_2$ with excellent R values. We were not able to obtain meaningful mixed occupancy in any other sites. The presence of all metals and their relative ratios in each of the new compounds were confirmed by semi-quantitive energy dispersive X-ray (EDX) spectroscopy (Figure S4.1 in supporting information).

The atomic positions, site occupation factors (SOF), and displacement parameters are given in Table 4.5. The results are comparable to those observed in similar compounds such as $Zr_2FeRu_5B_2$.[31] Selected interatomic distances and coordination are provided in Table 4.6. The Ru-B distances are the shortest ones in both structures. All interatomic

distances are comparable with isotypic systems like $Zr_2FeRu_5B_2$[31] or $Hf_3Ru_5B_2$[36], and hence we will keep the discussion limited. The Mn-Mn distance in $Zr_2MnRu_5B_2$ along [001] was found to be 3.073(1) Å, which is close to the Fe-Fe distance in $Hf_2FeRu_5B_2$, 3.089(2) Å. Although no strong bonding interactions are expected between these atoms, they are in the perfect distance range for inducing strong magnetic interactions, as demonstrated in other isotypic compounds and by the above DFT results.

Table 4.3. Results of the *Rietveld* refinement of the powder XRD data for $Zr_2MnRu_5B_2$ and $Hf_2FeRu_5B_2$.

Phase	$Zr_2MnRu_5B_2$	$Hf_2FeRu_5B_2$
Refined composition	$Zr_2Mn_{0.91(1)}Ru_{5.09(1)}B_2$	$Hf_2Fe_{0.81(1)}Ru_{5.19(1)}B_2$
Space group; *Z*	*P*4/*mbm* (no. 127), 2	
Profile function	pseudo-Voigt	
***a* (Å)**	9.322 (1)	9.307 (4)
***b* (Å)**	9.322 (1)	9.307 (4)
***c* (Å)**	3.0679 (4)	3.059 (1)
***V* (Å^3)**	266.66 (5)	265.0 (1)
***R*$_P$, *R*$_{Bragg}$**	3.80, 5.94	5.77, 9.77
Mass fraction (wt %)	100	94.8
Side Phase	-	HfRu (*P m*-3*m*) *a* = 3.205 (1) Å

Table 4.4. Single-crystal structure refinement data of $Zr_2MnRu_5B_2$ and $Hf_2FeRu_5B_2$.

Refined Composition	$Zr_2Mn_{0.95(1)}Ru_{5.05(1)}B_2$	$Hf_2Fe_{0.81(2)}Ru_{5.19(2)}B_2$
Space group, *Z*	*P*4/*mbm*, 2	
Formula weight (g/mol)	766.66	948.39
θ-range (°)	3.083-33.441	3.108-33.676
***hkl* range**	$-6 \le h \le 14$	$-14 \le h \le 10$
	$-14 \le k \le 2$	$-14 \le k \le 4$
	$-2 \le l \le 4$	$-3 \le l \le 4$
Cell parameters *a* (Å)	9.3448(7)	9.2705(4)
***b* (Å)**	9.3448(7)	9.2705(4)
***c* (Å)**	3.0728(4)	3.0489(2)
***V* (Å^3)**	268.33(5)	262.03(3)
***F*(000)**	672	805
Crystal size (mm^3)	0.101×0.017×0.009	0.121×0.025×0.017
No. of reflections; R_{int}	830; 0.0169	939; 0.0273
No. of independent reflections	310	307
No. of obs. reflections $I > 2\sigma(I)$	284	286
No. of Parameters	20	19
Absorption coefficient μ (mm^{-1})	19.345	55.943
Difference peak/hole (e Å^{-3})	1.551/-1.854	3.057/-3.295
GooF	1.173	1.066
R_1; wR_2 (all *I*)	0.0317, 0.0668	0.0314, 0.0735
R_1; wR_2 ($I > 2\sigma$)	0.0282, 0.0656	0.0285, 0.0719
CSD depository number [a]	1909640	1909638

[a]:Further details of the crystal structures can be obtained from the http://www2.fiz-karlsruhe.de/icsd_home.html on quoting the respective deposition numbers.

Table 4.5. Atomic positions, site occupation factors (SOF), and displacement parameters (isotropic for boron) for $Zr_2MnRu_5B_2$ and $Hf_2FeRu_5B_2$.

Atom label	Wyckoff position	*x*	*y*	*z*	SOF	*U*eq
$Zr_2Mn_{0.95(1)}Ru_{5.05}B_2$						
Ru1	8*j*	0.07042(5)	0.21603(5)	0.5	1	0.0051(2)
Ru2	2*c*	0	0.5	0.5	1	0.0043(2)
Ru3	2*a*	0	0	0	0.05(1)	0.0042(6)
Mn1	2*a*	0	0	0	0.95(1)	0.0042(6)
Zr1	4*g*	0.17588(6)	0.67588(6)	0	1	0.0057(2)
B1	4*g*	0.6230(8)	0.1230(8)	0	1	0.009(2)
$Hf_2Fe_{0.81(2)}Ru_{5.19(2)}B_2$						
Ru1	8*j*	0.07011(8)	0.21444(8)	0.5	1	0.0043(2)
Ru2	2*c*	0	0.5	0.5	1	0.0040(3)
Ru3	2a	0	0	0	0.19 (2)	0.0045(7)
Fe1	2*a*	0	0	0	0.81 (2)	0.0045(7)
Hf1	4*g*	0.17571(4)	0.67571(4)	0	1	0.0065(2)
B1	4*g*	0.625(1)	0.125(1)	0	1	0.010(3)

Table 4.6. Selected interatomic distances (Å) in $Zr_2MnRu_5B_2$ and $Hf_2FeRu_5B_2$ as obtained from single-crystal refinement.

$Zr_2Mn_{0.95(1)}Ru_{5.05}B_2$			**$Hf_2Fe_{0.81(2)}Ru_{5.19(2)}B_2$**		
Within pentagonal prisms					
Zr1	Ru1	2.8499(6) - 2.9459(6)	Hf1	Ru1	2.8294(7) - 2.9248(7)
Zr1	Ru2	2.7862(5)	Hf1	Ru2	2.7624(3)
Within tetragonal prisms					
Mn1/Ru3	Ru1	2.6209(4)	Fe1/Ru3	Ru1	2.5881(6)
Mn1	Mn1	3.0728(4)	Fe1	Fe1	3.0489(2)
Within trigonal prisms					
B1	Ru1	2.206(5)	B1	Ru1	2.189(9)
B1	Ru2	2.237(5)	B1	Ru2	2.242(9)
Network of Prisms					
Ru1	Ru1	2.8222(7) - 3.0728(4)	Ru1	Ru1	2.825(1) - 3.0489(2)
Ru1	Ru2	2.7340(5)	Ru1	Ru2	2.7259(7)
Ru2	Ru2	3.0728(4)	Ru2	Ru2	3.0489(2)

4.4 Results and discussion of the magnetic data

In the following section we will discuss the magnetic properties of all the $A_2M_5Ru_5B_2$ (A = Zr/Hf, M = Mn/Fe) compounds under investigation. Table 4.7 contains results of the different magnetic measurements performed on the new compounds along with the ones reported earlier.

Magnetic properties of reported $Hf_2MnRu_5B_2$: Magnetic susceptibility measurements for $Hf_2MnRu_5B_2$ were reported already in [30]: A spontaneous magnetization was observed below the *Curie* temperature (T_C) = 115 K in the magnetization vs. temperature (μ – T) plot, thus a ferromagnetic state emerged below T_C. The inverse-susceptibility vs temperature (χ_{mol}^{-1} – T) plot showed a *Curie*-Weiss behavior $\chi_{mol} = C/(T- \Theta)$ above 275 K with a positive Weiss constant of Θ = +116.7 K, thus confirming the predicted Mn-Mn FM interactions found by both sp-VASP and COHP analysis for this compound. Interestingly, under much weaker field (0.005 T) a maximum was observed in the μ – T plot at T_N =20 K, suggesting that the actual ground state may be of very weak AFM nature (AFM1-type). The experimentally determined *Curie* constant C = 1.17×10^{-5} m^3Kmol^{-1} at 0.1 T corresponds to an effective paramagnetic moment of μ_{para} = 2.63 μ_B. The magnetic moment did not saturate up to a field of 0.5 T while performing field dependent measurements (B – H curve), however, the determined magnetic moment at 4 K was 0.70 μ_B/f.u. at the highest applied field of 5 T field.

Low-field magnetic measurements for $Zr_2FeRu_5B_2$: The magnetic susceptibility measurements on $Zr_2FeRu_5B_2$were reported [31] only at very high magnetic field (2.5 and 5 T) where spontaneous magnetization was observed below T_C = 239 K with an atomic

magnetic moment (0.24 μ_B/f.u. at 5 K, 5 T) and the compound was described to be ferrimagnetic. Although AFM1 was found to be the most stable model theoretically in this compound no maximum in the $\chi_{mol} - T$ plot was observed (absence of T_N). In fact, the *Curie*-Weiss fitting of the $\chi_{mol}^{-1} - T$ plot in the paramagnetic region (T > 220 K) yielded a positive *Weiss* constant Θ = +129.0 K (Table 4.7) indicating FM interactions. We have successfully synthesized and characterized this compound (Figure S4.2 and Table S4.1) and have performed this compound's thermomagnetic measurements at 0.1 T. This measurement shows the presence of a maximum in the $\chi_{mol} - T$ plot indicating the suspected antiferromagnetic transition at T_N = 23 K (Figure 4.5) confirming the AFM1 ground state. This feature was not revealed in the earlier report most likely due to the high field applied which might have destroyed the antiferromagnetic (AFM1-type) transition like in $Hf_2MnRu_5B_2$.

Magnetic properties of the new $Zr_2MnRu_5B_2$ and $Hf_2FeRu_5B_2$: Magnetic susceptibility for both new compounds were measured at different fields in the temperature range $4 \leq T \leq 370$ K. The μ – T plots at 0.1 T field for both $Zr_2MnRu_5B_2$ and $Hf_2FeRu_5B_2$ showed the presence of a maximum (T_N) at 28 K and 25 K, respectively, indicating an antiferromagnetic transition for both (Figure 4.5). However, this antiferromagnetic transition vanishes at high magnetic fields and a ferromagnetic state emerges with T_C ~75 K for $Zr_2MnRu_5B_2$ (Figure 4.8) and with T_C ~250 K for $Hf_2FeRu_5B_2$ (Figure 4.7, bottom)$_2$, indicating a meta-magnetic behavior for these compounds. Interestingly, T_C is clearly smaller for $Zr_2MnRu_5B_2$ than for $Hf_2FeRu_5B_2$ indicating much weaker intrachain FM interactions in the former (see also below).

The $\chi_{mol}^{-1} - T$ plot for $Zr_2MnRu_5B_2$ at 0.1 T (Figure 4.7, middle) shows a *Curie*-Weiss behavior in the range 250 – 370 K, analysis of which led to a positive Weiss constant Θ = +150.2 K and a *Curie* constant $C = 1.08\times10^{-5}$ m^3Kmol^{-1} which corresponds to a paramagnetic moment of μ = 2.63 μ_B. The $\chi_{mol}^{-1} - T$ plot for $Hf_2FeRu_5B_2$ also shows a *Curie*-Weiss behavior in the paramagnetic range 320 – 370 K leading to the Weiss constant Θ = +284.8 K and the *Curie* constant $C = 1.45\times10^{-5}$ m^3Kmol^{-1} corresponding to μ = 3.03 μ_B. These large and positive Weiss constants indicate the presence of strong FM interactions in both compounds. The smaller Weiss constant for $Zr_2MnRu_5B_2$ confirms its weaker FM interactions if compared to $Hf_2FeRu_5B_2$, as seen above with their T_C.

Field dependent measurements (hysteresis loops) were done for the two compounds up to an applied field of 0.5 T for $Zr_2MnRu_5B_2$ and 1.0 T for $Hf_2FeRu_5B_2$. At 5 K and 5 T a magnetic moment of 0.63 μ_B/f.u. for $Hf_2FeRu_5B_2$ and 0.39 μ_B/f.u. for $Zr_2MnRu_5B_2$ (Figure 4.8) is recorded. None of the compounds show magnetic saturation within this range of applied field, but $Hf_2FeRu_5B_2$ already shows a tendency to saturate thus confirming its stronger FM interactions. Both compounds show very weak hysteresis with very small coercivities (Figure 4.8, insets), indicating their soft magnetic nature.

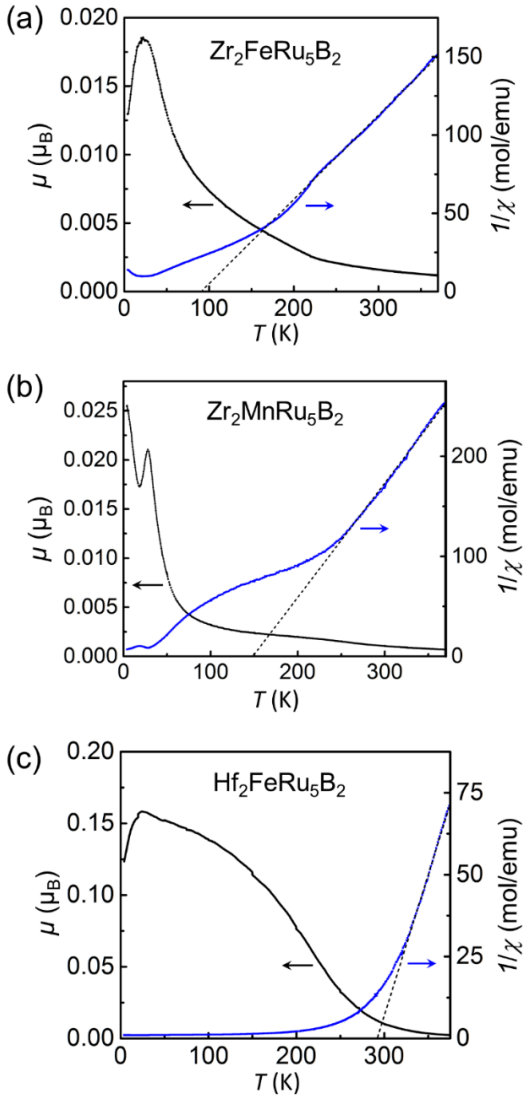

Figure 4.7. Zero-field-cooled (ZFC) magnetization vs temperature (μ – T) and inverse-susceptibility vs temperature (χ_{mol}^{-1} – T) plots for $Zr_2FeRu_5B_2$, $Zr_2MnRu_5B_2$ and $Hf_2FeRu_5B_2$ and measured at 0.1 T field.

Table 4.7. Results of the magnetic measurements of the $A_2MRu_5B_2$ quaternaries.

Compound	**T_N, (K) at 0.1 T**	**T_C (K)**	**μ_a (μ_B), 5T**	**Θ (K)**	**μ_{para} (μ_B)**	**Paramagnetic range (K)**	**Ref.**
$Zr_2FeRu_5B_2$	23 (T_N)	239	0.24	+91.4	3.85	220 - 370	[31], this work
$Zr_2MnRu_5B_2$	28 (T_N)	75	0.39	+150.2	2.61	250 - 370	this work
$Hf_2FeRu_5B_2$	25 (T_N)	250	0.63	+284.8	3.04	321 - 370	this work
$Hf_2MnRu_5B_2$	20 (T_N) (0.005 T)	115	0.70	+116.7	2.73	275 - 370	[30]

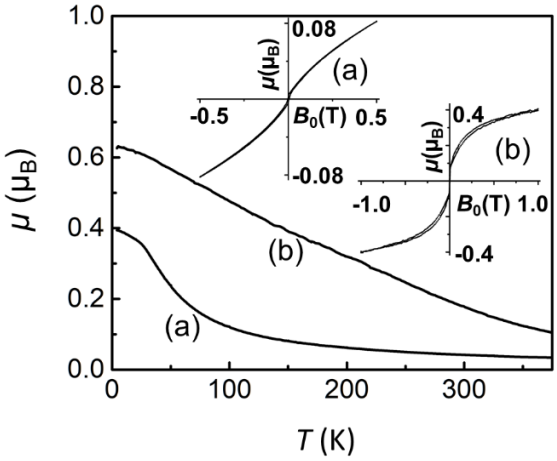

Figure 4.8. Magnetization vs temperature (μ – T) plot for $Zr_2MnRu_5B_2$ (a) and $Hf_2FeRu_5B_2$ (b) measured at 5 T field at 4 K, and Magnetization vs field strength curves (hysteresis loops) measured at 4 K (inset).

Magnetic trends in these phases: There are two types of interactions present in these compounds: The direct (and stronger) intrachain interaction at ca. 3.1 Å *M-M* distance and the indirect intrachain interaction between chains at 6.6 Å which are mostly due to conduction electrons. The nature and strength of these two interactions can be understood experimentally from the μ – T and $\chi_{mol}^{-1} - T$ plots. VASP calculations predicted that AFM1, which has antiferromagnetic interchain interactions is the most favorable model for three ($Zr_2FeRu_5B_2$, $Hf_2FeRu_5B_2$, and $Zr_2MnRu_5B_2$) out of four compounds. This prediction is verified experimentally as only these three compounds have an antiferromagnetic transition (T_N) at a relatively high magnetic field of 0.1 T. For the fourth compound, $Hf_2MnRu_5B_2$, predicted by VASP to have the weakest interchain AFM interactions (FM and AFM1 models are comparable in energies), T_N is observed only at much lower field (0.005 T) and it has the smallest antiferromagnetic transition (T_N = 20 K) of all four compounds, thus also confirming the VASP prediction. The presence of ferromagnetic intrachain *M-M*

interactions is reflected by the positive *Weiss* constants (Θ) for all compounds (Figure 4.7 and Table 4.7). Also, applying a magnetic field enables the flipping of spins between the chains, thereby inducing FM ordering with *Curie* Temperatures ranging from 75 K in $Zr_2MnRu_5B_2$ up to 250 K in $Hf_2FeRu_5B_2$. Consequently, all these compounds show metamagnetic behaviors

Magnetism in Ru-rich borides: There are only two other ruthenium-rich quaternary borides characterized in the $Ti_3Co_5B_2$ structure type ($Sc_2FeRu_5B_2$ and $Sc_2MnRu_5B_2$ [27]) and both phases show dominant antiferromagnetic interactions (negative *Weiss* constants). The main difference between these 2 phases and the four phases described above ($A_2MRu_5B_2$, A = Zr, Hf) is that the *A* elements are 4d/5d compared to 3d (Sc) in $Sc_2MRu_5B_2$, therefore the 4d/5d electrons may be playing a crucial role in inducing the rather strong FM interactions in these new $A_2MRu_5B_2$ phases. Table 4.8 lists some rare-earth-free ruthenium-rich borides that have been characterized for their magnetic properties. The magnetic properties of several Ru-containing borides crystallizing with the Th_7Fe_3-type structure have been studied in recent years. While many ternary Ru-rich phases have been studied, magnetic ordering was reported for $Fe_{0.5}Ru_{6.5}B_3$ [48] only, as predominating AFM interactions ($\theta = -74$ K) were observed, thus supporting the finding of dominating AFM interactions in Ru-rich $A_2MRu_5B_2$ borides where A is a 3d metal. More interesting are, however, the Th_7Fe_3-type quaternary series $MRh_{6-n}Ru_nB_3$ (M = Fe, Co; n = 1 – 5).[49,50] For $FeRh_{6-n}Ru_nB_3$, the *Curie* temperature and magnetic moment (μ_a^{5T}) decrease with increasing Ru content from T_C = 295 K and μ_a^{5T}= 3.35 μ_B (in $FeRh_5RuB_3$) to T_C = 205 K and μ_a^{5T} = 0.70 μ_B (in $FeRhRu_5B_3$). For $CoRh_{6-n}Ru_nB_3$, the magnetic

moment also decreases but linearly with increasing Ru content from 0.74 μ_B ($CoRh_5RuB_3$) to 0.13 μ_B ($CoRhRu_5B_3$). Considering that the Rh-free $Fe_{0.5}Ru_{6.5}B_3$ showed predominant AFM interactions and that all quaternaries show dominating FM interactions; it can be assumed that the nature of magnetic interactions in the quaternaries is markedly different from that of the ternary. Nevertheless, the decreasing magnetic moments in such solid solutions is likely due to the increasing strength of AFM interactions as the Ru-content increases, thereby directly linking the presence of AFM interactions to the Ru-content. Truly interesting is the series $Ti_{9-n}Fe_{2+n}Ru_{18}B_8$ (n = 0, 1, 2) because it was the first to show strong ferromagnetic ordering in a rare-earth-free ruthenium-rich boride both experimentally and theoretically for the n = 0 member. Interestingly, these compounds crystallize in the $Zn_{11}Rh_{18}B_8$-type structure with the same space group as $Ti_3Co_5B_2$ - (*P*/4*mbm*, no. 127), but they contain the unique ladders of Fe-atoms build by a chain of interconnected Fe-dumbbells that were found by density functional theory to be responsible for this unexpected magnetic behavior. All the $Ti_3Co_5B_2$-type compounds of the current study show positive *Weiss* constants and thus dominating FM interactions as well. However, the interplay between the magnetic element (Fe/Mn) and the 4*d*/5*d* electrons (Zr or Hf) is unique in these compounds and is to be credited for the strong FM interactions that were not observed earlier in this structure type such as in $Sc_2FeRu_5B_2$ and $Sc_2MnRu_5B_2$.

Table 4.8. Magnetic properties of other ruthenium-based borides.

Compound	Structure type	T_N, T_C (K) at 0.1 T	μ_a (μ_B), 5T	Θ (K)	Ref.
$Sc_2FeRu_5B_2$	$Ti_3Co_5B_2$	13 (T_N)	-	-995	[27]
$Sc_2MnRu_5B_2$	$Ti_3Co_5B_2$	11 (T_N)	-	-83.6	[27]
$Fe_{0.5}Rh_{6.5}B_3$	Th_7Fe_3	NA	0.31	-74	[48]
$Ti_9Fe_2Ru_{18}B_8$	$Zn_{11}Rh_{18}B_8$	200 (T_C)	1.2 (7 T)	+ 290	[33]
$Ti_8Fe_3Ru_{18}B_8$	$Zn_{11}Rh_{18}B_8$	210 (T_C)	0.868	+95	[34]
$Ti_7Fe_4Ru_{18}B_8$	$Zn_{11}Rh_{18}B_8$	220 (T_C)	1.814	+169	[34]

4.5 Conclusion

New quaternary borides $Hf_2FeRu_5B_2$ and $Zr_2MnRu_5B_2$ have been synthesized via arc-melting the elemental compositions and characterized by powder and single-crystal X-ray diffraction as well as EDX analysis. Electronic structure calculations through VASP indicated strong antiferromagnetic interactions between *M*-chains (*M* = Fe, Mn) in the Fe-based compound whereas competing ferro- and antiferromagnetic interactions are found in the Mn-based compound. Furthermore, it is shown through COHP analysis that the Fe-Fe interactions within the chains are stronger than the Mn-Mn interactions. Finally, vibrating sample magnetometry at 0.1 T showed the presence of a *Néel* Temperature (T_N) indicating the interchain antiferromagnetic interactions for the new compounds. However, both show positive Weiss constants indicating ferromagnetic intrachain *M-M* interaction. VASP energies and results of the magnetic measurements of the new compounds and the previously reported ones establish that the interplay between the magnetic element (Mn/Fe) and 4*d* or 5*d* element (Zr/Hf) dramatically lowers the AFM interactions in these compounds and increases ferromagnetic interactions. This effect was the maximum when both Hf and Mn were present together in $Hf_2MnRu_5B_2$.

4.6 Experimental Section

Synthesis: Elemental powders of Hf (99.6%), Zr (98%), Fe (99.5%) Mn (99.99%), Ru (99.9%) and B (99%, amorphous and crystalline) were purchased from Alfa-Aesar. Powders in proper ratios were mixed and pressed into pellet (0.3 g total mass) inside a glove box. The pellets were transferred to an arc-melting furnace with a water-cooled copper crucible connected to a Schlenk line. Melting of the pellets were done using 20 Amps current under argon atmosphere until homogenous melting was obtained (prolonged melting evaporates manganese). The sample was taken out after cooling down and crushed for characterization. Sample preparation and handling were performed using agate mortar-pestle and tungsten carbide die sets to avoid magnetic contamination. The synthesized phases were stable in the air as a compact bulk as well as finely ground powders.

Powder X-ray diffraction: The arc-melted samples were finely crushed, and Powder X-ray data were collected at room temperature, using a Rigaku MiniFlex 600 diffractometer with Cu-$K_{\alpha1}$ radiation (λ = 1.54059 Å), image plate detector, Ge monochromator using silicon as the standard.

Single-crystal X-ray diffraction: Suitable single-crystals were measured in a Rigaku XtalLAB mini diffractometer with λ(Cu-$K_{\alpha1}$) = 1.54059 Å for single-crystal structure analysis. The intensities were corrected with respect to the absorption using a numerical procedure based on gaussian integration over a multifaceted crystal model employed in CrysAlis Pro package.[51] The crystal structures were solved by the direct method and refined using SHELX employed in WinGX. [46, 47] The positions of the metals atoms

were obtained by direct methods and the boron position was found in the electron density map after a few cycles of the full-matrix least-squares refinement (based on F^2).

Magnetic measurements: The magnetic measurements were done by using a Vibrating Sample Magnetometer in an EverCool-II cryogen-free upgraded version of a Physical Property Measurement System (Quantum Design International, USA). Magnetization vs temperature measurements of approximately 30 mg powdered sample of $Zr_2MnRu_5B_2$ and $Hf_2FeRu_5B_2$ were carried out at different fields in the temperature range 4-375 K.

Computational details: All VASP calculations employed the generalized gradient approximation (GGA) with exchange and correlation treated by the Perdew-Burke-Enzerhoff (PBE) functionals. The convergence threshold for structural relaxation was set to be 0.02 eV/Å in force. The cutoff energy for the plane wave calculations was set to 500 eV and the Brillouin zone integrations were carried out using a $5 \times 5 \times 15$ and $5 \times 5 \times 7$ k-point mesh for crystallographic unit cells (non-magnetic, FM and AFM1) and cells doubled along the c-axis (AFM2), respectively.

Within TB-LMTO, exchange and correlation were treated using the von Barth-Hedin local density (LDA) and local spin-density approximation (LSDA). All relativistic effects except spin-orbit coupling were taken into account using a scalar relativistic approximation. The basis sets include 2s and 2p wave functions for B, 3d, 4s, 4p wave functions for Mn, 4d, 5s, 5p wave functions for Ru, 5d, 6s, 6p wave functions for Hf and 4d, 5s, 5p wave functions for Zr. The B 3d, Ru, Zr, and Hf 4f orbitals were treated by the Löwdin downfolding technique. Sets of $2 \times 2 \times 8$ k-points in the irreducible wedge of the Brillouin zone were used for integrations over crystallographic unit cells.

4.7 Supporting Information

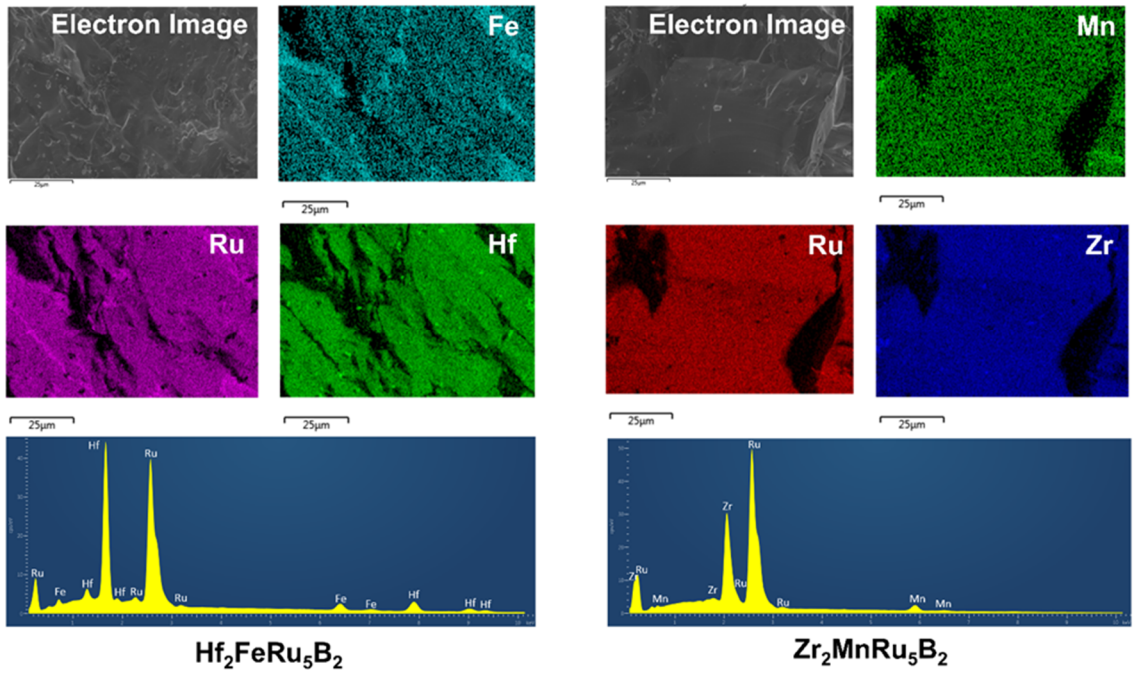

Figure S4.1. EDX mapping and EDX spectrum for the synthesized phase along with electron image from SEM

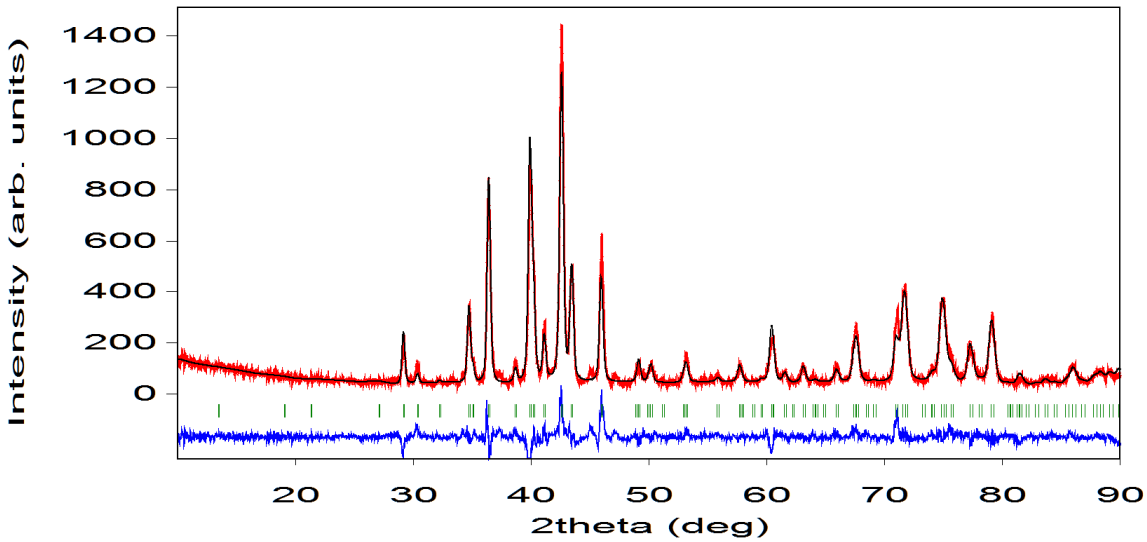

Figure S4.2. Powder X-ray diffractogram with *Rietveld* refinement for the arc melted samples of "$Zr_2FeRu_5B_2$. Red shows the measured and black shows the calculated XRD pattern. Positions of the Bragg peaks for the phase(s) are shown in green.

Table S4.1. Results of the *Rietveld* refinement of powder X-Ray diffraction for $Zr_2FeRu_5B_2$.

Phase	$Zr_2FeRu_5B_2$
Refined Composition	$Zr_2Fe_{0.82(1)}Ru_{5.18(1)}B_2$
Space group; *Z*	P4/*mbm* (no. 127), 2
Profile function	pseudo-Voigt
***a* (Å)**	9.318 (1)
***b* (Å)**	9.318 (1)
***c* (Å)**	3.064 (1)
***V* (Å^3)**	266.07 (3)
R_P, R_{Bragg}	5.32, 8.98
Mass fraction (wt %)	100
Side Phase	None

4.8 References

[1] G. Akopov, M. T. Yeung, R. B. Kaner, *Adv. Mater*., 2017, 1604506.

[2] M. Teng, H. Li, X. Zheng, S. Wang, X. Wang, H. Zhao, S. Han, et al. *Adv. Mater.,* 2017*,* 29, 1604003.

[3] J. P. Scheifers, Y. Zhang, B. P. Fokwa, *Acc. Chem. Res.,* 2017, *50*, 2317–2325.

[4] M. T. Yeung, J. Lei, R. Mohammadi, C. L. Turner, Y. Wang, S. H. Tolbert, R. B. Kaner. *Adv. Mater., 2016,* 6993–6998.

[5] J. V. Rau, A. Latini, *Chem. Mater*., 2009, 21, 1407 – 1409.

[6] B. Albert, H. Hillebrecht. *Angew. Chem. Int. Ed.* 2009, 48, 8640-8668.

[7] J. B. Levine, S. H. Tolbert, R. B. Kaner, *Adv. Funct. Mater*. 2009, 19, 3519-3533.

[8] Q. Gu, G. Krauss, W. Steurer, *Adv. Mater*., 2008, *20*, 3620-6.

[9] H. Y. Chung, M. B. Weinberger, J. B. Levine, A. Kavner, J. M. Yang, S. H. Tolbert, R. B. Kaner, *Science*, 2007 *316*, 436-439.

[10] J. Nagamatsu, N. Nakagawa, T. Muranaka, Y. Zenitani, J. Akimitsu, *Nature*, 2001, *410*, 63.

[11] W. Xie, H. Luo, K. Baroudi, J. W. Krizan, B. F. Phelan, R. J. Cava, Chem. Mater., 2015, *27*, 1149-1152.

[12] Q. Zheng, R. Gumeniuk, H. Rosner, W. Schnelle, Y. Prots, U. Burkhardt, Y. Grin, A. Leithe-Jasper, *J. Phys.: Condens. Matter*, 2015, 27, 415701.

[13] J. Wong, T. Tanaka, M. Rowen, F. Schäfers, B. R. Müller, Z. U. Rek, *J. Synchrotron Radiat.* 1999, *6*, 1086 – 1095.

[14] S. Hirt, F. Yuan, Y. Mozharivskyj, H. Hillebrecht, *Inorg. Chem*., 2016, *55*, 9677-9684.

[15] X. Tan, P. Chai, C. M. Thompson, M. Shatruk, *J. Am. Chem. Soc.* 2013, *135*, 9553–9557.

[16] P. Chai, S. A. Stoian, X. Tan, P. A. Dube, M. Shatruk, *J. Solid State Chem.*, 2015, *224*, 52-61.

[17] M. Jalaly, B. K. Khosroshahi, F. J. Gotor, M. J. Sayagués, S. A Yamini, F. Failamani, T. Mori, *Ceram. Int.*, 2019, *45*(11), 14426-14431.

[18] J.F. Herbst, Rev. Mod. Phys., 1991, *63*, 819 – 898.

[19] O. Gutfleisch, M. A. Willard, E. Brück, C. H. Chen, S. G. Sankar, J. P. Liu, Advanced materials. 2011, 23, 821-842.

[20] E. Nagelschmitz, W. Jung, *Chem. Mater.* 1998, *10*, 3189-3195.

[21] a) B. P. T. Fokwa, *Eur. J. Inorg. Chem.* 2010, *2010*, 3075-3092; b) Y. B. Kuz'ma, Y. P. Yarmolyuk, *J. Struct. Chem.* 1971, *12*, 422-424.

[22] H. Zhu, Ni. Chaoying, F. Zhang, D. Youwei, J. Q. Xiao, *J. Appl. Phys.,* 2005*,* 97, 10M512.

[23] W. Xie W, M. K. Fuccillo, B. F. Phelan, H. Luo, R. J. Cava, *J. Solid State Chem.,* 2015, *227*, 92-97.

[24] B. Petermüller, C. Neun, M. Stekiel, D. Zimmer, M. Tribus, K. Wurst, B. Winkler, H. Huppertz, *Chem. Eur. J*., 2018, *24*, 14679-14685.

[25] P. Shankhari, J. P. Scheifers, M. Hermus, K. Yubuta, B. P. T. Fokwa, *Z. Anorg. Allg. Chem.,* 2017, 643, 1551-1556.

[26] G. D. Samolyuk, B. P. T. Fokwa, R Dronskowski, G. J. Miller, *Phys. Rev. B.* 2007, *76*, 094404.

[27] E. A. Nagelschmitz, Dissertation, University of Cologne, Cologne (Germany) 1995

[28] B. P. T. Fokwa, H, Lueken, R. Dronskowski, *Chem. Eur. J.* 2007, *13*, 6040-6046.

[29] R. Dronskowski, K. Korczak, H. Lueken, W Jung, *Angew. Chem. Int. Ed.* 2002, *41*, 2528-2532.

[30] P. Shankhari, Y. Zhang, D. Stekovic, M. E. Itkis, B. P. T. Fokwa, *Inorg. Chem.*, 2017, *56*, 12674-12677.

[31] J. Brgoch, S. Yeninas, R. Prozorov, G. J. Miller, *J. Solid State Chem.* 2010, *183*, 2917-2924.

[32] K. Hiebl, P. Rogl, E. Uhl, M. J. Sienko, *Inorg. Chem.*, 1980, 19, 3316-3320.

[33] B. P. T. Fokwa, G. D. Samolyuk, G. J. Miller, R. Dronskowski, *Inorg. Chem.*, 2008, 47, 2113-2120.

[34] C. Goerens, J. Brgoch, G. J. Miller, B. P. Fokwa, *Inorg. Chem.*, 2011, 50, 6289-6296.

[35] U. Eibenstein, W. Jung, *Z. Anorg. Allg. Chem.*, 1998, 624, 802-806.

[36] M. Hermus, B. Fokwa, *Eur. J. Inorg. Chem.* 2014, *2014*, 3085-3094.

[37] P. E. Blöchl, *Phys. Rev. B* 1994, *50*, 17953-17979.

[38] G. Kresse, D. Joubert, *Phys. Rev. B* 1999, *59*, 1758-1775.

[39] G. Kresse, J. Furthmüller, *Phys. Rev. B* 1996, *54*, 11169-11186.

[40] (a) J. Hafner, *Comp. Chem.* 2008, *29*, 2044-2078. (b) R. Tank, O. Jepsen, A. Burkhardt, O. K. Andersen, TB-LMTO-ASA Program, version 4.7. Max-Plank Institute for Solid-State Research, 1994 Stuttgart, Germany

[41] Y. Zhang, G. J. Miller, B. P. T. Fokwa, *Chem. Mater.* 2017, 29, 2535-2541.

[42] B. P. T. Fokwa, H Lueken, H. R. Dronskowski, *Eur. J. Inorg. Chem.* 2011, 2011, 3926-3930.

[43] M. Hermus, M. Yang, D. Grüner, F. J. DiSalvo, B. P. T. Fokwa, *Chem. Mater.* 2014, *26*, 1967-197.

[44] D. S. Young, B. S. Sachais, L. C. Jefferies, The *Rietveld* method, 1993.

[45] J. Rodriguez-Carvajal, *In satellite meeting on powder diffraction of the XV congress of the IUCr*, 1990, *127,* Toulouse, France.

[46] G. M. Sheldrick, *Acta Crystallogr., Sect. A: Found. Crystallogr.* 2008, *A64*, 112.

[47] L. J. Farrugia, WINGX, a windows program for crystal structure analysis. University of Glasgow, Glasgow, 1998.

[48] P. R. N. Misse, Ph.D. Thesis, RWTH Aachen University: Germany, 2012

[49] P. Shankhari, P. R. N. Misse, M. Mbarki, H. Park, B. P. T. Fokwa, *Inorg. Chem.*, 2017, *56,* 446–451

[50] H. Park, P. R. N. Misse, M. Mbarki, P. Shankhari, B. P. T. Fokwa, Eur. J. *Inorg. Chem.,* 2017, 4467–4472

[51] CrysAlisPro 1.171.39.38b, Rigaku Oxford Diffraction, 2017

Chapter 5

Enhancing Magnetic Anisotropy by Maximizing 5d Elements in $Ti_3Co_5B_2$ Structure Type Borides: Large Coercivities and High Ordering Temperatures in $Hf_2FeIr_5B_2$ and $Hf_2MnIr_5B_2$

5.1 Introduction

Continuous growth in clean and environment-friendly technologies such as electric vehicles, magnetic refrigeration, and wind turbines has increased demands of high-performing (magnets having high energy product, BH_{max}) permanent magnetic materials.[1, 2] Today's best-performing permanent magnets are mostly made from rare-earth (RE) elements, especially Nd and Dy, both of which have been marked as "critical" by U.S. Department of Energy.[3] Intrinsically, these RE-based permanent magnets possess large magnetocrystalline anisotropy energy (MAE) which mainly stems from large spin-orbit coupling (SOC) of rare-earth (f-electrons) elements. This large MAE results in very high coercivity (H_C) value that contributes to the high energy product (BH_{max}). [1, 4] Theoretically, the performances of RE magnets are difficult to beat by the rare-earth-free (REF) counterparts, but, given the small supply risk of REF permanent magnets, they are being considered in less-demanding applications.[2, 5] In recent years, major progress has been made toward improving the performance of REF magnets by extrinsic parameters, such as microstructure and processing. [5] Nevertheless, preparing new REF magnetic materials showing superior intrinsic properties, such as large MAE has been a challenge to the scientific community for the last 20 years. Although continuous efforts have been made, very less has been achieved—mainly because of the complex nature of magnetism itself.

Mn-based alloys such as MnAl, MnBi, Mn-Ga; [6] binary alloys of Zr-Co and Hf-Co; [7, 8] $L1_0$-ordered compounds, such as, FeCo, CoPt, FeNi; and iron nitrides (α''-$Fe_{16}N_2$) [9] are some of the most widely studied, REF permanent magnets of the past decade which show large coercivity (H_C values 40 to several hundred kA/m) and high ordering temperature (as high as ~1000 K). Most of these compounds, however, suffer from issues arriving during their synthesis, processing or stability. For example, MnBi starts to decompose at 535 K, metastable nature of MnAl makes it difficult to obtain good texture and high coercivity simultaneously through standard manufacturing methods, $L1_0$-ordered FeNi and FeCo are difficult to form and their bulk synthesis has not been achieved yet, and the impressive magnetic properties Zr-Co and Hf-Co nanoparticle films suffer in their bulk forms. As a result, we still largely rely on 35 years old RE permanent magnets for commercial use.[10]

As far as designing a new permanent magnetic material is concerned, the desired properties are (i) a high ordering temperature (T_C), (ii) a large saturation magnetization and (iii) a strong magnetic anisotropy.[4] Since magnetism is highly sensitive to temperature, a high T_C and good thermal stability are desired for any practical application of a magnet without requiring additional cooling steps. Although the first two criteria mentioned above can be met with a rare-earth-free pure transition metal/intermetallic magnet without any f-electrons, it is the latter requirement that throws a real challenge. Magnetic anisotropy refers to the dependence of magnetic energy on the magnetization axis compared to the crystallographic axes. Such preferred orientation of spins is responsible for maintaining the

metastable domain configuration of a permanent magnet and affects the coercivity and remanence—thus, the shape of the hysteresis loop.[11]

Zhang et al. described the theoretical procedure on calculating MAE applying density functional theory (DFT) methods for the tetragonal $Ti_3Co_5B_2$ system.[11] According to their work, there are three contributions towards the total MAE: (i) single-ion magnetic anisotropy that arises through SOC, (ii) relative orientation of these magnetic ions is controlled by spin-exchange coupling (iii) long-range magnetic dipole-dipole (MDD) interactions. They evaluated the SOC energy (E_{SOC}), the spin-exchange energy and the MDD interactions of previously reported hard magnetic material $Sc_2FeRu_3Ir_2B_2$.[12] These calculations resulted in a very large MAE for this compound (-2.85 meV/f.u.) due to its very large E_{SOC} = -2.81 meV/f.u. Although this compound showed large E_{SOC} value, the spin exchange energy which originates from relative orientation of spins as parallel (FM) or antiparallel (AFM), showed the presence of dominating antiparallel spins (antiferromagnetic interaction), which most likely resulted in small magnetization (0.45 μ_B/f.u.) of this compound. By replacing Sc (3d element) and Ru (4d element) with 5d elements Hf and Ir, respectively, we have maximized the number of 5d electrons and designed two new compounds: $Hf_2FeIr_5B_2$ and $Hf_2MnIr_5B_2$. VASP energy calculations yielded in E_{SOC} of +3.27 meV/u.c. and -1.55 meV/u.c. for the Fe- and the Mn-based compounds, respectively. The E_{SOC} value calculated for the Fe-based compound is the highest reported so far in this structure type. Moreover, calculations for this compound did not show the presence of any antiferromagnetic interactions, implying higher magnetization and ordering temperature. Following the promising theoretical results, both

compounds were successfully synthesized by arc-melting under argon, structurally characterized using XRD techniques, and their magnetic properties were investigated. Both compounds order well above room temperature, ca. 901 K for $Hf_2FeIr_5B_2$ and ca. 590 K for $Hf_2MnIr_5B_2$. Moreover, $Hf_2FeIr_5B_2$ shows large magnetic moment as a result of the uncompensated ferromagnetic interactions but moderate coercivity value, H_C = 12.0 kA/m. $Hf_2MnIr_5B_2$, however, shows very large coercivity value, H_C = 62.0 kA/m along with high ordering temperature of 590 K. This is the highest reported H_C value and the first high-temperature hard magnetic material in the $Ti_3Co_5B_2$ structure type.

5.2 Results and discussion

5.2.1 Computational details

It is important to mention at this point that, as chemists, while designing the new compounds we focused only on the intrinsic properties based solely on composition and crystal structure. Macroscopic effects, such as grain size, surface defects, and post-synthesis processing were not considered. The recipe to design the new compounds was clear: maximize the number of 5d elements in an anisotropic crystal system. Since we recently published the bulk synthesis of the $Hf_3Ir_5B_2$ [14], this compound was taken as the starting point for the new quaternaries $Hf_2MIr_5B_2$ (M = Fe, Mn). $Hf_3Ir_5B_2$ crystallizes in the tetragonal system with a/c ~ 2.8 (an isotropic system, such as cubic, will have a/c = 1) and has the maximum number of 5d elements (3Hf and 5Ir) reported in a $Ti_3Co_5B_2$ structure type compound till date. Thus, we envisioned the new quaternaries $Hf_2MIr_5B_2$ (M = Fe, Mn) by replacing Hf by the magnetic element M at the Wyckoff site 2a (tetragonal Ir-prism) of $Hf_3Ir_5B_2$ structure. DFT calculations were used to investigate the electronic

structure and spin orientations in the newly designed compounds. The lattice parameters of the quaternaries were relaxed using the projector augmented wave method of Blöchl [14, 15] coded in the Vienna ab Initio Simulation Package (VASP).[16] All VASP calculations employed the generalized gradient approximation (GGA) with Perdew-Burke-Enzerhoff functional.[17]

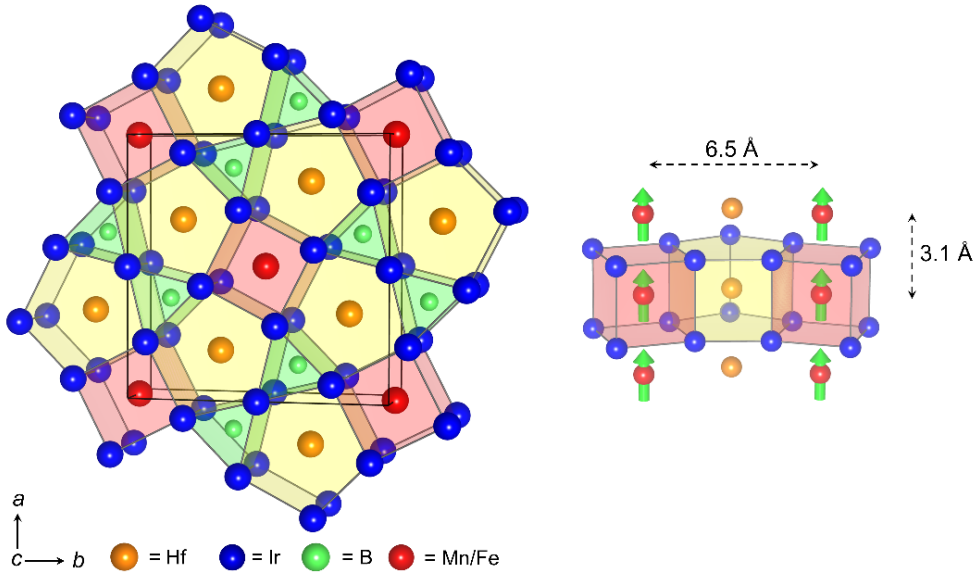

Figure 5.1. The perspective of crystal structures of the quaternaries $Hf_2MIr_5B_2$ (M = Fe, Mn) viewed along [001] (left) formation of magnetic chains (right).

We reported on the electronic structures of the ternary $Hf_3Ir_5B_2$. The non-spin-polarized (nsp, without spin-polarization) density of states (DOS) plot (presented in Figure 5.2) shows a large pseudogap around the Fermi level (E_F) indicating the electronic stability of this ternary—a typical feature of the $Ti_3Co_5B_2$ structure type.[18] Upon replacing the Hf at *Wyckoff* site 2*a* with M (M = Fe, Mn) in the quaternaries, the DOS increases sharply at E_F giving rise to a peak. DOS plots of the quaternaries are given in Figure 5.3a and 5.3b and both show the presence of a sharp peak at E_F. Interestingly, the nsp-DOS plots of the two

compounds look very similar. However, this electronic instability was stabilized upon spin-polarization through lowering states at E_F giving rise to magnetic moments. The resulting spin-polarized (sp) DOS plots are shown in Figure 5.3c and 5.3d.

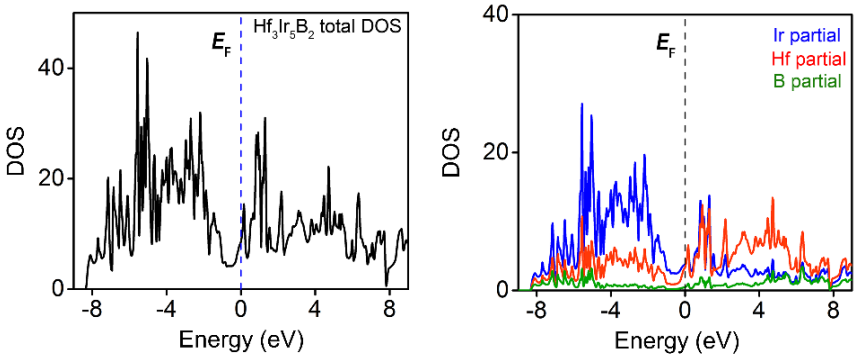

Figure 5.2. Non-spin-polarized total DOS plots for $Hf_3Ir_5B_2$ (left), partial Hf, Ir and B DOS (right).

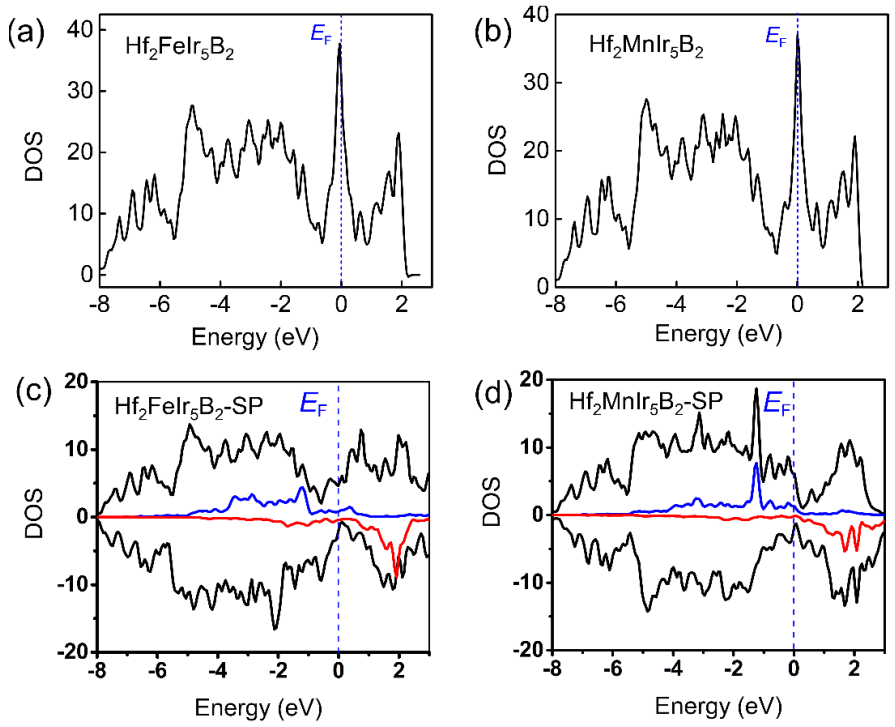

Figure 5.3. Non-spin-polarized total DOS plots for $Hf_2FeIr_5B_2$ (a), $Hf_2MnIr_5B_2$ (b), spin-polarized total DOS plots for $Hf_2FeIr_5B_2$ (c), $Hf_2MnIr_5B_2$ (c).

The placement of the *M* atoms in the 2*a* Wyckoff site generates one-dimensional chains along crystallographic direction [001] in $Ti_3Co_5B_2$-type quaternaries.[] The exchange energies can be estimated by evaluating the spin-exchange interactions between the magnetic atoms. This was done by calculating the relative energies of three different magnetic models, namely, FM, AFM1, and AFM2 (Figure 5.4), as previously done for $Hf_2MnRu_5B_2$. The total energies of these three magnetic models were calculated using VASP and the result of the calculations are given in Table 5.1.

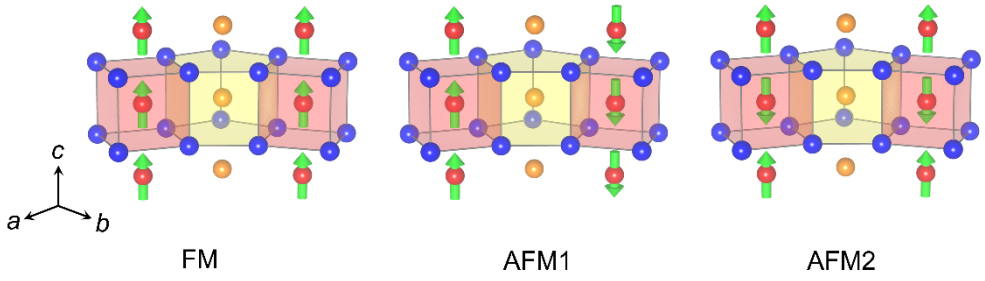

Figure 5.3. Magnetic models used for VASP calculations of $Hf_2MIr_5B_2$ quaternaries showing possible interactions within and between the chains.

Table 5.1. Relative energies of different magnetic models compared to the most stable one (**in bold**) obtained through VASP calculations.

Compound	**Relative energy compared to the most stable model (meV/f.u.)**			
	FM	AFM1	AFM2	NM
$Hf_2FeIr_5B_2$	**0.00**	40.19	96.17	1106.15
$Hf_2MnIr_5B_2$	60.01	**0.00**	242.47	1507.31

As evident from Table 5.1, all magnetic models for both the compounds were much stable than the corresponding non-magnetic models (NM, without any spin-polarization). This indicates that spin-polarization is energetically favorable. The spin interactions in the two

compounds are quite different: while the $Hf_2FeIr_5B_2$ has a predicted FM ground state, $Hf_2MnIr_5B_2$ is predicted to order with an AFM1-type antiferromagnetic ground state. Thus, the *M-M* interchain interactions (mostly due to conduction electrons because of the large M-M distance of 6.5 Å) in the two compounds are opposite in sign, while the intrachain M-M interactions are the same. These results are quite exciting and somewhat unexpected for $Hf_2MnIr_5B_2$, while they are in perfect agreement for $Hf_2FeIr_5B_2$ if compared with previously reported $Ti_3Co_5B_2$-type compounds. In fact, Ru-rich Fe-based compounds mostly prefer antiferromagnetic ground state (AFM1 type) and have less than 63 valence electrons (VE), while FM ground state is more stable for those richer in group-9-elements (Rh, Ir) having more than 63 VE. Examples of AFM1 compounds include; $Zr_2FeRu_5B_2$ (62 VE) [19], $Hf_2FeRu_5B_2$ (62 VE) [20], $Ti_2FeRu_4RhB_2$ (63 VE) [11] and $Sc_2FeRu_3Ir_2B_2$ (62 VE) [11], and FM compounds are $Hf_2FeIr_5B_2$ (67 VE, present work), $Ti_2FeRh_5B_2$ [11], $Ti_2FeCo_5B_2$, [11] and $Hf_2FeCo_5B_2$ [11]. However, the Mn-based compounds do not show a solid trend. Only four Mn-based compounds have been calculated before: $Hf_2MnRu_5B_2$ (61 VE) [21], $Zr_2MnRu_5B_2$ (61 VE) [20], $Ti_2MnCo_5B_2$ (66 VE) [11], $Hf_2MnCo_5B_2$ (66 VE) [11], and $Hf_2MnIr_5B_2$ (66 VE, present work). In contrast to the Fe-based compounds, the trend in Mn-based compounds is not VE-dependent at all. While the two reported Hf-based compounds have the FM ground state, all other compounds including the new Hf-based one prefer the AFM1 ground state regardless of VEs. From these data, it is impossible to draw a conclusion on the trend of the Mn-based compounds and it is better to treat the Fe- and Mn-based compounds separately. The results from the VASP calculation of all Fe- and Mn-based compound reported for this structure type are given in table 5.2. Thus, while the

transition between antiferromagnetism to ferromagnetism around 63 VE as proposed in previous works well for the Fe-based compounds it does not apply to the Mn-based phases.

Table 5.2. Valence electron count (VEC), and relative energies of different magnetic models compared to the most stable one obtained through VASP calculations for all Fe- and Mn-based compounds in $Ti_3Co_5B_2$ structure type . The most stable model is given in boldface.

Compound	VEC	Relative energy. The most stable model is given in boldface (meV/f.u.)			Reference
		FM	AFM1	AFM2	
Fe-based compounds					
$Hf_2FeIr_5B_2$	67	**0.00**	40.19	96.17	**This work**
$Ti_2FeRh_5B_2$	67	**0.00**	3.74	11.70	[11]
$Ti_2FeCo_5B_2$	67	**0.00**	53.09	199.07	[11]
$Hf_2FeCo_5B_2$	67	**0.00**	58.88	155.79	[11]
$Hf_2FeRu_5B_2$	62	38.30	**0.00**	38.40	[20]
$Zr_2FeRu_5B_2$	62	44.50	**0.00**	44.25	[20]
$Ti_2FeRu_4RhB_2$	63	30.55	**0.00**	22.22	[11]
$Sc_2FeRu_3Ir_2B_2$	62	36.77	**0.00**	10.77	[11]
Mn-based compounds					
$Hf_2MnIr_5B_2$	66	60.01	**0.00**	242.47	**This work**
TiMnCo5B2	66	9.82	**0.00**	144.69	[11]
$Hf_2MnCo_5B_2$	66	**0.00**	5.46	194.77	[11]
$Hf_2MnRu_5B_2$	61	**0.00**	1.92	33.05	[21]
$Zr_2MnRu_5B_2$	61	2.40	**0.00**	49.95	[20]

In addition to the exchange interaction analysis through VASP calculations, crystal orbital Hamilton population (COHP) analysis was performed using the Stuttgart version of the tight-binding, linear muffin-tin orbital (TB-LMTO) method with the atomic spheres approximation [22] in order to verify the VASP-predicted M-M ferromagnetic intrachain interactions within the *M*-chains. According to the -COHP methodology, FM interactions would place E_F in an antibonding region while for AFM it would be placed in a bonding region. [23] Figure 5.5 shows the -COHP plots for both Fe-Fe and Mn-Mn interactions in

their respective compounds. Indeed, E_F is placed in an antibonding region for both -COHP curves, thus confirming the presence of ferromagnetic intrachain M-M spin interactions in both compounds.

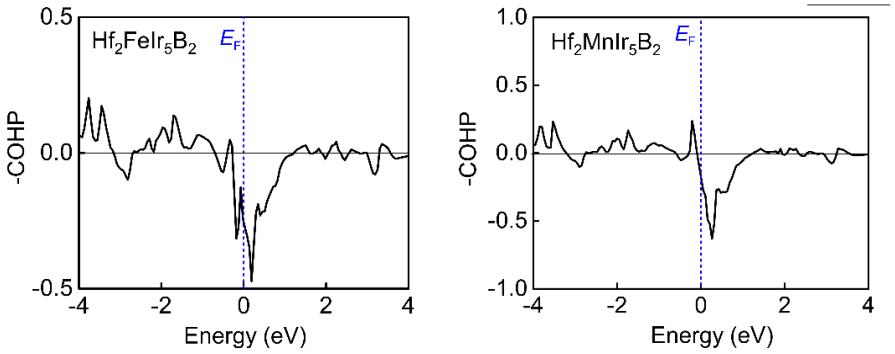

Figure 5.5. Non-spin-polarized COHP plots for *M*-*M* (*M* = Fe/Mn) interaction along [001] for $Hf_2FeIr_5B_2$ (left) and $Hf_2MnIr_5B_2$ (right).

Finally, we examined the SOC contribution towards the total MAE by applying GGA+SOC calculations as described by Zhang et al.[11] for calculations of the $Ti_3Co_5B_2$-type compounds. VASP total energies of spin parallel (E_{SOC} $\|c$) and perpendicular (E_{SOC} $\perp c$) to the crystallographic *c*-axis for each compound were calculated. The net SOC energy (E_{SOC}) was then calculated using the relation,

$$E_{SOC} = E_{SOC} \|c - E_{SOC} \perp c$$

Results of the E_{SOC} calculations are given in Table 5.3 along with the E_{SOC} of some other reported compounds of the same type. Since the contribution of magnetic dipole-dipole interaction (MDD) towards the total MAE is very small, typically in the order of 10^{-2} meV/f.u., we have ignored it in calculating the total MAE ($E_{MAE} = E_{SOC} + E_{MDD}$), and hence, the total MAE can be approximated as $E_{MAE} \approx E_{SOC}$.

Table 5.3. E_{SOC} ($E_{SOC} = E_{SOC} \parallel c - E_{SOC} \perp c$) and relative exchange energy of $Ti_3Co_5B_2$ structure type compounds. The exchange energy is estimated as the energy difference between FM and AFM1 models.

Compound	E_{SOC} meV/f.u.	$E_{AFM1} - E_{FM}$ meV/f.u.	Reference
$Hf_2FeIr_5B_2$	+3.27	+40.19	**This work**
$Hf_2MnIr_5B_2$	-1.55	-60.01	**This work**
$Sc_2FeRu_3Ir_2B_2$	-2.83	-36.77	[11]
$Ti_2FeRu_4RhB_2$	-0.23	-30.55	[11]
$Ti_2FeRh_5B_2$	-0.18	+3.74	[11]
$Ti_2FeCo_5B_2$	+0.14	+53.09	[11]
Hf_2FeCo_5B2	+0.20	+58.88	[11]
$Hf_2MnRu_5B_2$	+0.42	+1.92	[21]
$Ti_2MnCo_5B_2$	+0.12	-9.82	[11]
$Hf_2MnCo_5B_2$	+0.99	+5.46	[11]

The calculated E_{SOC} for $Hf_2FeIr_5B_2$ is +3.27 meV/f.u. indicating a large magnetic anisotropy in which spin $\perp c$ (easy plane) is favored over spin $\parallel c$. This value is also larger than all E_{SOC} values reported so far for $Ti_3Co_5B_2$-type phases (Table 5.3). For example, the highest was calculated value so far (-2.83 meV/f.u.) for $Sc_2FeRu_3Ir_2B_2$ where the orientation $\parallel c$ (easy axis) was favored over $\perp c$.

Interestingly, the Mn-based compound $Hf_2MnIr_5B_2$ shows characteristics that are very similar to those of $Sc_2FeRu_3Ir_2B_2$. In fact, $Hf_2MnIr_5B_2$ also shows a very high E_{SOC} value (-1.55 meV/f.u.) and has an easy c axis. Moreover, the large exchange energy observed (-60.01 meV/f.u.) originates from the antiferromagnetic orientation of spins. The large coercivity value in $Sc_2FeRu_3Ir_2B_2$ was explained by the large MAE as well as the large negative exchange energy (-36.77 meV/f.u.) which originates from strong AFM1 type antiferromagnetic interactions. In fact, breaking these interactions is necessary (using an extra external magnetic field) is necessary before flipping of the magnetic spins can occur

with the flipping of the external field, thereby increasing the field needed. The direct consequence of this analysis is that $Hf_2MnIr_5B_2$ is predicted to have a similar (or larger) coercivity as $Sc_2FeRu_3Ir_2B_2$. Given that most REF hard magnetic materials have far smaller E_{SOC} values such as -0.15 meV/f.u. for MnBi, there is a very high chance that the predicted high magnetic anisotropies may lead to hard magnetic properties for these new phases, either intrinsically (see experimental part below) or extrinsically (future work).

5.2.2 Phase analysis and structure determination

The phase analysis of both the new compounds was done by *Rietveld* refinement [24] of the powder X-ray diffraction (XRD) data using the *FullProf* [25] method. Results of the refinements are given in figure 5.6 and table 5.4. The refinements confirmed the $Ti_3Co_5B_2$ structure type (space group *P*4/*mbm,* no. 127) for both the new compounds with lattice parameters of a = 9.0975(7) Å and c = 3.2040(3) Å for $Hf_2FeIr_5B_2$ and a = 9.1827(6) Å and c = 3.2139(3) Å for $Hf_2MnIr_5B_2$. Additionally, both the samples contain a common side phase $HfIr_3B_{0.5}$. This side phase which belongs to the cubic crystal system is non-magnetic in nature and thus should not interfere in the magnetic measurements. Mixed occupancy refinement of Ir and Fe/Mn at the *Wyckoff* site 2*a* led to the final compositions of $Hf_2Fe_{0.66(1)}Ir_{5.34(1)}B_2$ and $Hf_2Mn_{0.81(1)}Ir_{5.19(1)}B_2$. $Zr_2FeRu_5B_2$,[20] $Hf_2MnRu_5B_2$ [21] and many other reported quaternaries in this structure type show a similar mixed occupancy at the *2a* position.

The refined lattice parameters of the two new quaternary compounds are smaller than those of their parent ternary $Hf_3Ir_5B_2$ [a = 9.264(2) Å, c = 3.3070(5) Å] because the larger Hf atoms are replaced by the smaller Mn/Fe atoms. Additionally, we have earlier

noticed through VASP calculations that magnetic interaction is further responsible for contraction of the lattice parameters in such $Ti_3Co_5B_2$-type compounds containing magnetically active elements.[20]

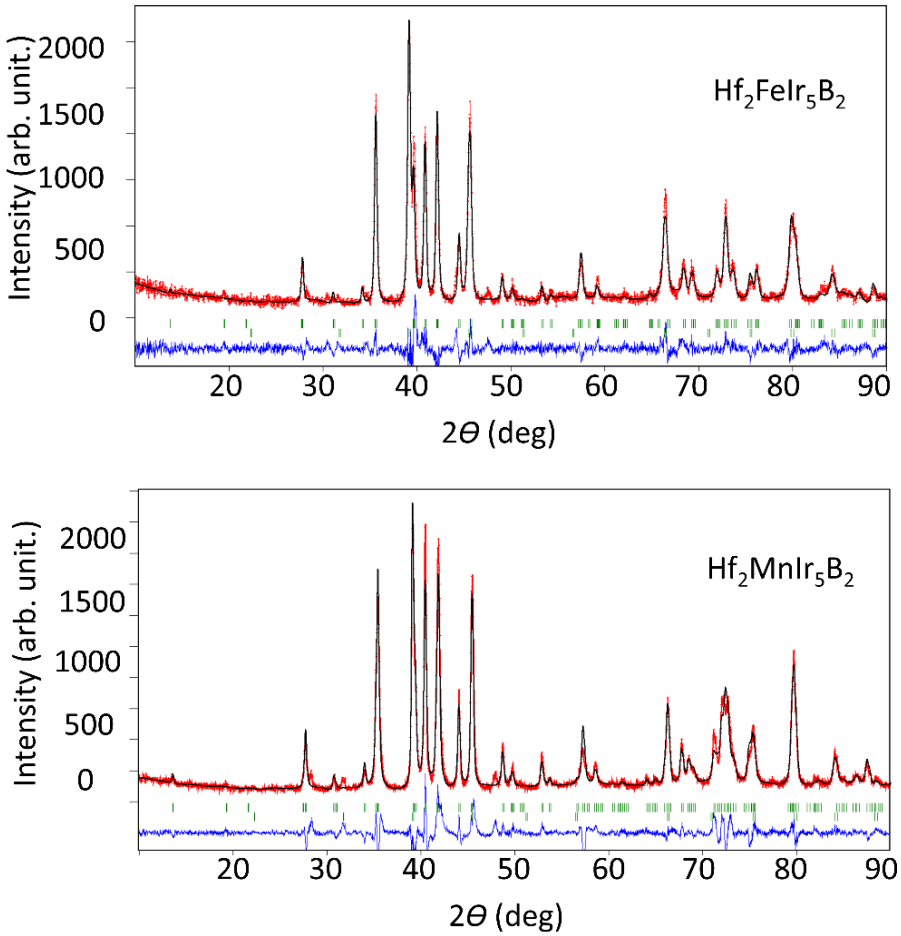

Figure 5.6. *Rietveld* refinement of the powder XRD data for the $Hf_2FeIr_5B_2$ (top) and $Hf_2MnIr_5B_2$ (bottom) samples. The red and the black curves represent the measured and the calculated patterns, respectively, whereas the blue curve shows the intensity difference. The positions of the *Bragg* peaks are shown in green.

Table 5.4. Results of the *Rietveld* refinement of the powder XRD data for $Hf_2FeIr_5B_2$ and $Hf_2MnIr_5B_2$.

Phase	$Hf_2FeIr_5B_2$	$Hf_2MnIr_5B_2$
Refined composition	$Hf_2Fe_{0.66(1)}Ir_{5.34(1)}B_2$	$Hf_2Mn_{0.81(1)}Ir_{5.19(1)}B_2$
Space group; *Z*	*P*4/*mbm* (no. 127), 2	
Profile function	pseudo-Voigt	
***a* (Å)**	9.0975(7)	9.1827(6)
***b* (Å)**	9.0975(7)	9.1827(6)
***c* (Å)**	3.2040(3)	3.2139(3)
***V* (Å^3)**	265.18(4)	265.0 (1)
R_P, R_{Bragg}	6.50, 9.41	5.14, 8.30
Mass fraction (wt %)	66	84
Side Phase	$HfIr_3B_{0.5}$ (*P m-3m, no. 221*) a = 3.9798(3) Å	$HfIr_3B_{0.5}$ (*P m-3m, no. 221*) a = 3.9846(2) Å

5.2.3 Results and discussion of the magnetic data

The magnetic susceptibility (χ) was measured in zero-field-cooled mode at 10 kOe field (1T) as a function of temperature (T) on polycrystalline $Hf_2FeIr_5B_2$ (temperature range 3-950 K) and $Hf_2MnIr_5B_2$ (temperature range 3-650 K) samples. The low temperature χ-T plot (Figure 5.7 top left) for $Hf_2FeIr_5B_2$ shows a typical behavior of a ferromagnet: increasing susceptibility with lowering of the temperature. Interestingly, significant susceptibility at highest measured temperature (300 K) under the instrumental setup indicated that the ordering temperature is much higher than room temperature (RT) and further measurements were necessary to get a complete picture. Indeed, at higher temperatures (Figure 5.7 top right) a rapid increase of the susceptibility around 900 K is

observed. Using the method described in [26] to determine T_C, an ordering temperature of ~901 K was estimated for this new compound.

The χ-T plot of $Hf_2MnIr_5B_2$ (Figure 5.7 bottom left) shows a maximum indicating a *Neel* temperature (T_N) at 30 K. The presence of T_N at this high field (1T) indicates a robust magnetic transition and hints at significantly strong AFM interactions. Recently, we discovered $Hf_2MnRu_5B_2$ which also orders antiferromagnetically with T_N = 20 K. However, in $Hf_2MnRu_5B_2$ the AFM interactions are very weak and a small field as low as 0.1 T was enough to destroy this AFM ordering in favor of FM ordering. These results confirm the VASP calculations which have predicted strong AFM ground state for $Hf_2MnIr_5B_2$ (this work) but a competition between FM and AFM1 ground states for $Hf_2MnRu_5B_2$ [21]. However, just like $Hf_2MnRu_5B_2$ and most AFM-based compounds in the compound family, the interchain AFM interactions may be affected by the magnetic field or the temperature, leading to metamagnetic behaviors. $Hf_2MnIr_5B_2$ is not different and shows a second FM-like ordering at elevated temperatures (ca. 590 K). Therefore, coupling its high T_C with the VASP-predicted large MAE, $Hf_2MnIr_5B_2$ is expected to be an excellent candidate for achieving large coercivity at or above RT.

Field-dependent magnetization ($\mu - H$) was measured at different temperatures and up to 80 kOe (8T) field. The $\mu - H$ plots are given in Figure 5.8. The magnetization of $Hf_2FeIr_5B_2$ measured at 3 K rose rapidly as we increased the applied field up to 10 kOe and then slowly reached near-saturation at about 30 kOe where an atomic moment μ_a = 3.1 μ_B/f.u. was observed. Further increasing the field up to 8T only resulted in a slight increase in the atomic moment where it reached a maximum value of μ_a = 3.2 μ_B/f.u.

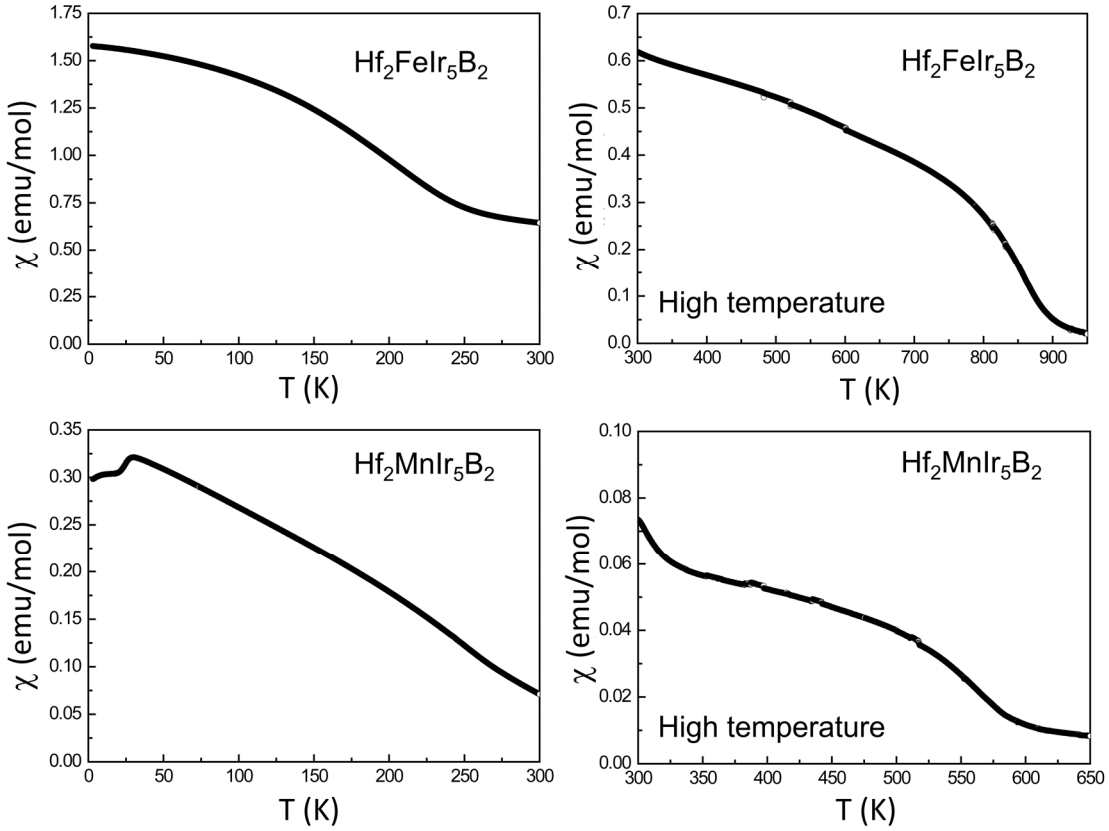

Figure 5.7. Magnetic susceptibility as a function of temperature for $Hf_2FeIr_5B_2$ (left) and $Hf_2MnIr_5B_2$ (right) plotted as low (top) and high (bottom) temperature data measured at 10 kOe.

The magnetization of $HfMnIr_5B_2$, at 3 K, on the other hand, did not saturate up to 8 T. It rapidly increased up to 10 kOe, and then a linear increase of the moment was observed with an increasing magnetic field, where it reached about $\mu_a = 0.8\ \mu_B$/f.u. at 8 T. Lower value and the unsaturating nature of the magnetic moment indicated more of a metamagnetic behavior of the Mn-based compound, resulting from the presence of both strong ferro- and antiferromagnetic interactions as indicated by the theoretical calculations.

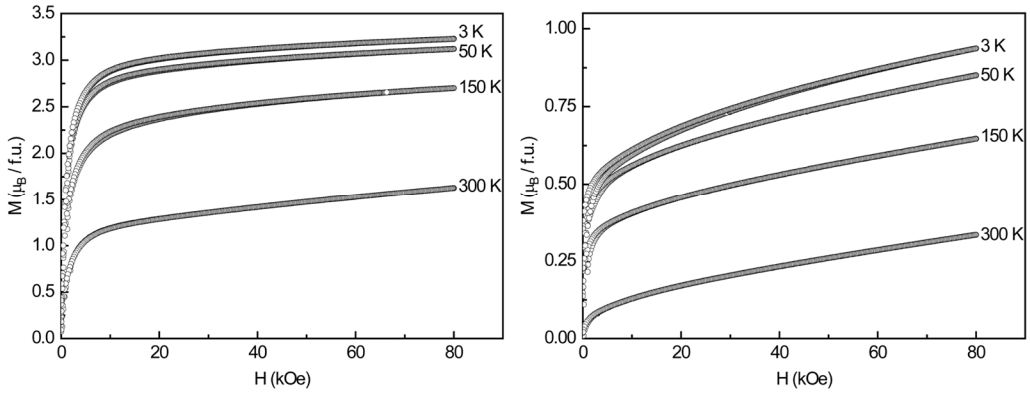

Figure 5.8. Field-dependent magnetization ($\mu - H$) measurements for $Hf_2FeIr_5B_2$ (left) and $Hf_2MnIr_5B_2$ (right).

5.2.4 Hysteresis loops and coercivity

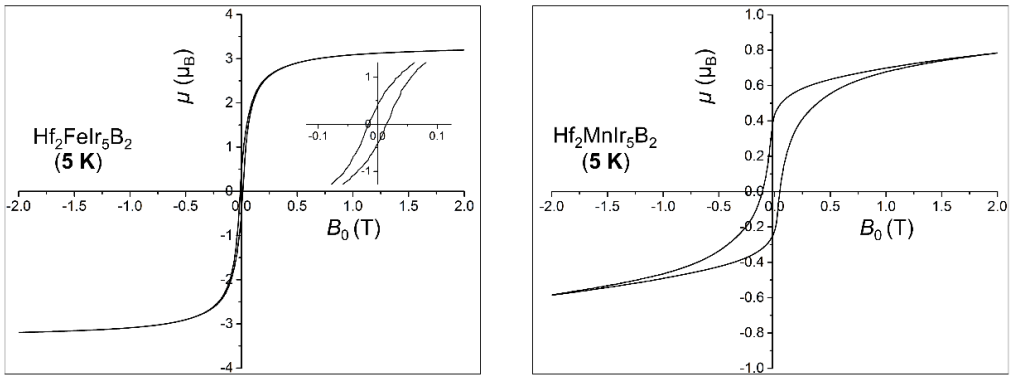

Figure 5.9. Magnetization vs field plots (hysteresis loop) measured at 5K for $Hf_2FeIr_5B_2$ (left) and $Hf_2MnIr_5B_2$ (right).

Figure 5.10 shows the *B-H* plots or Hysteresis loops measured for the compounds measured at 5K, up to a field of 2.0 T. Both the compounds show features of a ferromagnet. The following scale is used to determine soft, semihard, and hard magnetic materials:

H_C < 1 kA/m	soft
1 kA/m < H_C < 30 kA/m	semihard
H_C > 30 kA/m	hard

$Hf_2FeIr_5B_2$ shows a coercivity (H_C) value of 12.05 kA/m (at 5 K) and is thus, is classified as a "semihard" magnetic material. The other compound, $Hf_2MnIr_5B_2$, however, shows large coercivity, H_C = 62.0 kA/m and therefore, is a hard-magnetic material. Interestingly, this is the highest reported value of coercivity for this structure type and beats the previously reported value of 52.4 kA/m measured for $Sc_2FeRu_2Ir_3B_2$. Moreover, this compound shows very high ordering temperature and large coercivity at high temperature. Even at room temperature, the H_C value stays around 26 kA/m, whereas $Sc_2FeRu_2Ir_3B_2$ (H_C = 52.4 kA/m at 5K, 5T) had a low ordering temperature (T_C = 85 K) and practically paramagnetic at room temperature.[12]

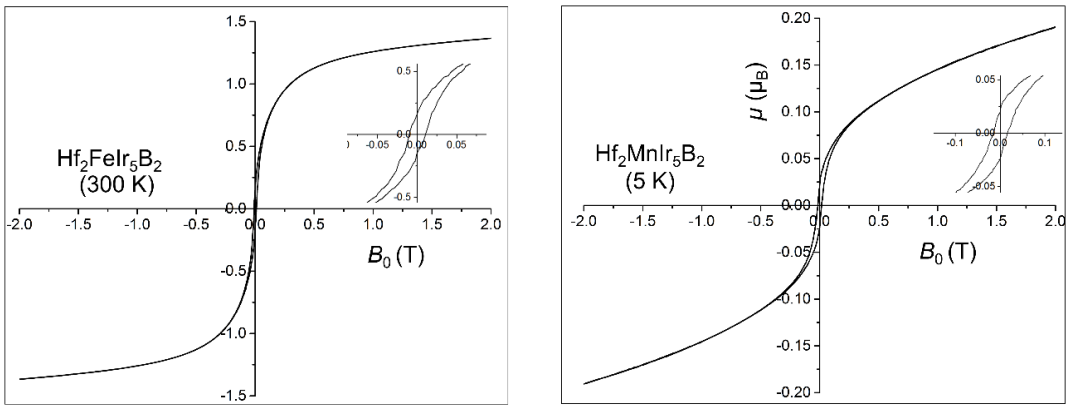

Figure 5.10. Magnetization vs field plots (hysteresis loop) measured at 300K for $Hf_2FeIr_5B_2$ (left) and $Hf_2MnIr_5B_2$ (right).

5.3 Conclusion

As far as the magnetic property is concerned, the newly synthesized compounds fall in the lower range of the H_C spectrum, but they show very high ordering temperatures and chemical and thermal stability. Both the compounds are thermally stable as they were synthesized at ca. 3000 ºC and can withstand concentrated HCl at room temperature for several hours. It is worth mentioning that the magnetic measurements of the new

compounds were performed on as-synthesized powder sample (micrometer-sized) obtained from crushing a bulk ingot without any further processing, hence, the magnetic properties observed are purely intrinsic in nature. Most of the materials discussed above, on the other hand, show their superior magnetic properties only in a highly-processed state like ball-milled, particle size reduced, thin-filmed, sintered, or densified state.[5] These extrinsic properties hugely amplify magnetic hardness. For example, the high-temperature hard ferromagnetic Hf-Co and Zr-Co alloys are prepared using the same arc-melting technique that we use. Following the arc melting, the alloys are re-melted to a molten state and then melt-spun to form nanocrystalline ribbons before measuring their magnetic properties.[] McGuire et al. measured the melt-spun ribbon of "$Hf_2Co_{11}B$" alloy at 24 m/s which showed very soft ferromagnetism with $H_C \leq 10$ Oe (0.80 kA/m) compared to 780 Oe of $Hf_2MnIr_5B_2$. The same alloy, melt-spun at a rate of 16 m/s showed coercivity values as high as 4500 Oe (358.1 kA/m).[7] Thus, upon further processing, the potential of getting a very high-energy product out of the two newly synthesized materials is enormous. Even though we had to use expensive 5d elements to achieve high coercivity and ordering temperature, these compounds can be utilized in the less quantity-demanding application such as, microelectromechanical systems (MEMS) and spintronics devices that demand stability and performance.

5.4 Experimental section

The starting materials used for the synthesis of the title phase were elemental powders of Hf (99.6%), Mn (99.99%), Ir (99.9%) and B (99% amorphous and crystalline), purchased from Alfa Aesar. The elements were weighed in the desired atomic ratio, mixed well (total

mass around 0.3 g) and was pressed into a pellet inside a glove box. The pellet was arc-melted under argon atmosphere using a Schlenk line. The argon gas was purified prior to use over silica gel, molecular sieves and titanium sponge (at 950 K). The melting was performed on a water-cooled copper crucible using a tungsten tip as the second electrode, where the pellet was re-melted for few seconds with a direct current of 20 Amperes until a homogeneous melting was achieved (prolonged melting will evaporate manganese). During the handling, sample preparation, manipulation, and synthesis tungsten carbide die sets, agate mortar-pestle were used in order to avoid any magnetic contaminations. The synthesized phase was stable in the air as a compact bulk as well as finely ground powders. Powder X-ray data of synthesized compound was collected at room temperature, using Rigaku MiniFlex 600 diffractometer [Cu-$K\alpha_1$ radiation (λ = 1.54059 Å), Ge monochromator, image plate detector, and silicon standard].

Energy-dispersive X-ray spectroscopy (EDX) was carried out on an ultra-high-resolution low-energy system of the type Nova NanoSEM450 equipped with a 50mm^2 X-Max 50 SD EDX detector.

The magnetic measurements of both compounds were carried out using a vibrating sample magnetometer in an EverCool-II cryogen-free upgraded version of a Physical Property Measurement System (Quantum Design International, USA).

5.5 References

[1] K. P. Skokov, O. Gutfleisch, *Scripta Mater.,* 2018, *154*, 289-294.

[2] O. Gutfleisch, M. A. Willard, E. Brück, C. H. Chen, S. G. Sankar, J. P. Liu. *Adv. Mater.,* 2011, 23, 821-842.

[3] https://www.energy.gov/sites/prod/files/DOE_CMS2011_FINAL_Full.pdf

[4] M. D. Kuz'Min, K.P. Skokov, H. Jian, I. Radulov, O. Gutfleisch, *J.Phys.: Condens. Matter*, 2014, *26*, 064205.

[5] J. Cui, M. Kramer, L. Zhou, F. Liu, A. Gabay, G. Hadjipanayis, B. Balasubramanian, D. Sellmyer, *Acta Mater.,* 2018, *158*, 118-137.

[6] W. Xie, E. Polikarpov, J-P Choi, M. E. Bowden, K. Sun, J. Cui, *J. Alloy. Comp.* 2016, *680*, 1-5.

[7] M. A. McGuire, O. Rios, N. J. Ghimire, M. Koehler, *App. Phys. Lett.*, 2012, *101*(20), 202401.

[8] B. Balasubramanian, B. Das, R. Skomski, W. Y. Zhang, D. J. Sellmyer, *Adv. Mater.,* 2013, *25*(42), 6090-6093.

[9] T. Kojima, M. Ogiwara, M. Mizuguchi, M. Kotsugi, T. Koganezawa, T. Ohtsuki, T.-Y. Tashiro, K. Takanashi, *J. Phys. Condens. Matter,* 2014, *26*, 064207.

[10] J. J. Croat, J. F. Herbst, R.W. Lee, F. E. Pinkerton, *J. Appl. Phys.,* 1984, *55*(6), 2078-2082.

[11] Y. Zhang, G. J. Miller, B. P. T. Fokwa, *Chem. Mater.* 2017, 29, 2535-2541.

[12] M. Hermus, M. Yang, D. Grüner, F. J. DiSalvo, B. P. T. Fokwa, *Chem. Mater.* 2014, *26*, 1967-1974.

[13] P. Shankhari, J. P. Scheifers, M. Hermus, K. Yubuta, B. P. T. Fokwa, *Z. Anorg. Allg. Chem.*, 2017, *643*, 1551-1556.

[14] P. E. Blöchl, *Phys. Rev. B* 1994, *50*, 17953-17979.

[15] G. Kresse, D. Joubert, *Phys. Rev. B* 1999, *59*, 1758-1775.

[16] G. Kresse, J. Furthmüller, *Phys. Rev. B* 1996, *54*, 11169-11186.

[17] J. P. Perdew, K Burke, M. Ernzerhof, *Phys. Rev. Lett.* 1996, *77*, 3865−3868.

[18] Y. B. Kuz'ma, Y. P. Yarmolyuk, *J. Struct. Chem.* 1971, *12*, 422-424.

[19] J. Brgoch, S. Yeninas, R. Prozorov, G. J. Miller, *J. Solid State Chem.* 2010, *183*, 2917-2924.

[20] P. Shankhari, *PhD Dissertation*, University of California, Riverside, 2019

[21] P. Shankhari, Y. Zhang, D. Stekovic, M. E. Itkis, B. P. T. Fokwa, 2017, *Inorg. Chem*., 2017, *56*, 12674-12677.

[22] R. Tank, O. Jepsen, A. Burkhardt, O. K. Andersen, TB-LMTO-ASA Program, version 4.7. Max-Plank Institute for Solid-State Research, 1994 Stuttgart, Germany

[23] R. Dronskowski, K. Korczak, H. Lueken, W Jung, *Angew. Chem. Int. Ed.* 2002, *41*, 2528-2532.

[24] D. S. Young, B. S. Sachais, L. C. Jefferies, The *Rietveld* method, 1993.

[25] J. Rodriguez-Carvajal, *In satellite meeting on powder diffraction of the XV congress of the IUCr*, 1990, *127,* Toulouse, France.

[26] B. P. T. Fokwa, G. D. Samolyuk, G. J. Miller, R. Dronskowski, Inorganic chemistry, 2008, 47, 2113-2120.

6. Dissertation Conclusion

$Ti_3Co_5B_2$ is a versatile structure type among metal-rich borides including ternary ($A_3T_5B_2$), quaternary ($A_2MT_5B_2$) and quinary ($A_2M(TT')_5B_2$) phases in its large family. Although more than sixty compounds with $Ti_3Co_5B_2$-type structure are known, only nine ternaries have been found since the first report of $Ti_3Co_5B_2$ in 1971 by Kuzma *et. al*. We have synthesized bulk $Ti_3Co_5B_2$ for the first time and found a significant mixed occupancy of Ti and Co on the 2*a* site, leading to its reformulation as $Ti_{3-x}Co_{5+x}B_2$ (x = 0 – 0.5). Moreover, we report the first single-crystal data on the isoelectronic $Hf_3Ir_5B_2$ with $Ti_3Co_5B_2$-type structure. The corresponding mixture of Zr, Rh, and B, however, did not form a compound in the $Ti_3Co_5B_2$-type structure under the same reaction conditions. We have found out that the radii ratio r_A/r_T and the electronegativity difference play a great role in understanding this unexpected trend. DFT calculations also provide further support for this trend, as the Gibbs free energy of formation greatly favors the $Ti_3Co_5B_2$-type structure over the perovskite-like structure for $Ti_3Co_5B_2$ and $Hf_3Ir_5B_2$.

Interestingly, many quaternary variants $A_2MT_5B_2$ (*M* = magnetically active element) of this structure type are known to show magnetic ordering that comes from *M*-*M* interaction within and between the one-dimensional magnetic chains build by *M*-atoms. We predicted theoretically and then realized experimentally a competition between antiferro- and ferromagnetic states for the first time in the ruthenium-rich compound $Hf_2MnRu_5B_2$. VASP total energy calculations showed a slightly stable ferromagnetic ground state (FM type). Earlier investigations in such Fe-based ruthenium-rich compounds had shown a clear preference for antiferromagnetic (AFM1) type ground states. Thus, it was believed that

Mn-was behaving differently from iron in this type of compounds and this needed to be further investigated. Therefore, we performed a complete theoretical and experimental study on the four the ruthenium-rich quaternary borides $A_2MRu_5B_2$ (A = Hf, Zr; M = Fe, Mn, etc.) which established the fundamental difference between the Mn and Fe-based Ru-rich compounds in this structure type. Electronic structure calculations through VASP indicated strong antiferromagnetic interactions between M-chains (M = Fe, Mn) in the Fe-based compound whereas competing ferro- and antiferromagnetic interactions are found in the Mn-based compound. VASP energies and results of the magnetic measurements of the new compounds and the previously reported ones established that the interplay between the magnetic element (Mn/Fe) 5*d* element can dramatically lower the AFM interactions in these compounds and increases ferromagnetic interactions. This effect was the maximum when both Hf and Mn were present together in $Hf_2MnRu_5B_2$. This study opened possibilities to synthesize new ferromagnetic materials based on Hf and Mn.

Further increasing the number of 5d elements by replacing Ru by Ir yielded 5d-rich $Hf_2FeIr_5B_2$ and $Hf_2MnIr_5B_2$ which were predicted to have strong magnetic anisotropy (i.e. permanent magnet candidates). Experiments confirmed and extended these predictions: $Hf_2FeIr_5B_2$ orders at T_C ~ 901 K with 12 kA/m coercivity whereas $Hf_2MnIr_5B_2$ orders at ca. 590 K with 62 kA/m coercivity (the highest value reported for this structure type). $Hf_2MnIr_5B_2$ is the first hard magnetic material in this structure type showing high ordering temperature. Mn-based alloys such as MnAl, MnBi, Mn-Ga; binary alloys of Zr-Co and Hf-Co; $L1_0$-ordered compounds, such as, FeCo, CoPt, FeNi; and iron nitrides (α''-$Fe_{16}N_2$) are some of the most widely studied, REF permanent magnets of the past decade which

show large coercivity (H_C values 40 to several hundred kA/m) and high ordering temperature (as high as ~1000 K). Most of these compounds, however, suffer from issues arriving during their synthesis, processing or stability. As far as the magnetic property is concerned, newly synthesized $Hf_2FeIr_5B_2$ and $Hf_2MnIr_5B_2$ fall in the lower range of the H_C spectrum, but they show very high ordering temperatures and chemical and thermal stability. Both the compounds are thermally stable as they were synthesized at ca. 3000 ºC and can withstand concentrated HCl at room temperature for several hours. It is worth mentioning that the magnetic measurements of the new compounds were performed on as-synthesized powder sample (micrometer-sized) obtained from crushing a bulk ingot without any further processing, hence, the magnetic properties observed are purely intrinsic in nature. Most of the materials discussed above, on the other hand, show their superior magnetic properties only in a highly-processed state like ball-milled, particle size reduced, thin-filmed, sintered, or densified state. These extrinsic properties hugely amplify magnetic hardness. Thus, upon further processing, the potential of getting a very high-energy product out of the two newly synthesized materials is enormous. Even though we had to use expensive 5d elements to achieve high coercivity and ordering temperature, these compounds can be utilized in the less quantity-demanding application such as, microelectromechanical systems (MEMS) and spintronics devices that demand stability and performance.